NASA TM X-53326

SUMMARY OF BASE THERMAL ENVIRONMENT
MEASUREMENTS ON THE SATURN I BLOCK I FLIGHT VEHICLES

By Ira P. Jones, Jr.
   Aero-Astrodynamics Laboratory

NASA

*George C. Marshall
Space Flight Center,
Huntsville, Alabama*

TECHNICAL MEMORANDUM X-53326

SUMMARY OF BASE THERMAL ENVIRONMENT MEASUREMENTS ON THE SATURN I BLOCK I FLIGHT VEHICLES

By

Ira P. Jones, Jr.

George C. Marshall Space Flight Center
Huntsville, Alabama

ABSTRACT

Base thermal environment measurements were made on all of the Saturn I Block I vehicles (SA-1 through SA-4). Total and radiation calorimeter measurements were made in the base region along with base gas temperatures and pressures. Details of the instrumentation and problems encountered in the data evaluation are discussed, and the data are compared from flight to flight on the basis of altitude. Some representative correlations of total and radiation heating, gas temperatures, and base pressures with small scale model tests are included. Flight heat transfer coefficients are calculated and compared with the model results.

NASA - GEORGE C. MARSHALL SPACE FLIGHT CENTER

NASA - GEORGE C. MARSHALL SPACE FLIGHT CENTER

TECHNICAL MEMORANDUM X- 53326

September 3, 1965

SUMMARY OF BASE THERMAL ENVIRONMENT MEASUREMENTS
ON THE SATURN I BLOCK I FLIGHT VEHICLES

By

Ira P. Jones, Jr.

AERO-ASTRODYNAMICS LABORATORY

TABLE OF CONTENTS

LIST OF ILLUSTRATIONS

LIST OF ILLUSTRATIONS (Cont'd)

LIST OF ILLUSTRATIONS (Cont'd)

LIST OF ILLUSTRATIONS (Cont'd)

LIST OF ILLUSTRATIONS (Cont'd)

LIST OF ILLUSTRATIONS (Concluded)

LIST OF TABLES

DEFINITION OF SYMBOLS

SYMBOL	DEFINITION
A	Active area of the sensor
C_p	Heat capacity of the sensor material
D	Base diameter
$\dfrac{dT}{d\theta}$	Slope of the calorimeter slug temperature
h	Heat transfer coefficient
I	Transmission
IECO	Inboard engine cut-off
K	Conduction loss coefficient, calibration factor
k	Thermal conductivity of air
m	Thermal mass of the sensor material
OECO	Outboard engine cut-off
O/F	Oxygen to fuel ratio
P	Pressure
$\dot{q}_c$	Convective heating rate
Q_{coL}	Conduction losses from the slug
Q_L	Heat lost by the slug
$\dot{q}_R$	Radiation heating rate
Q_{rrL}	Reradiation loss from slug surface

DEFINITION OF SYMBOLS (Cont'd)

SYMBOL	DEFINITION
Q_s	Heat stored in the slug
Q_T	Total heat absorbed by the slug
$\dot{q}_T$	Total heating rate
r	Refractive index
T	Sensor thermocouple temperature
t	Thickness of the thermal mass
T_i	Calorimeter slug temperature at ignition
T_w	Calorimeter slug temperature during flight
V	Velocity
α	Absorption coefficient
β	Total calorimeter view angle
γ	Specific heat ratio
ϵ	Emissivity
θ	Time
ν	Kinematic viscosity
ρ	Density of the thermal mass
σ	Stefan-Boltzman radiation constant
φ	Angle of incidence

DEFINITION OF SYMBOLS (Concluded)

SYMBOL   DEFINITION

SUBSCRIPTS

B   Heat shield

$\overline{B}$ Average over heat shield

c-o   Engine cut-off condition

crit   Critical condition

F   Flame shield

flt   Flight condition

∞ Free stream condition

g   Condition of gas

i   Initial condition

ℓ Downstream condition

mod   Model condition

O   Reservoir condition

R   Recovery condition

Ref   Reference condition

SUMMARY OF BASE THERMAL ENVIRONMENT MEASUREMENTS ON THE SATURN I BLOCK I FLIGHT VEHICLES

SUMMARY

Base thermal environment measurements were made on all of the Saturn I Block I vehicles (SA-1 through SA-4). Total and radiation calorimeter measurements were made in the base region along with base gas temperatures and pressures. Details of the instrumentation and problems encountered in the data evaluation are discussed, and the data are compared from flight to flight on the basis of altitude. Some representative correlations of total and radiation heating, gas temperatures, and base pressures with small scale model tests are included. Flight heat transfer coefficients are calculated and compared with the model results.

Maximum heating rates on the heat and flame shields occurred at lift-off for both the total and radiation calorimeters. Maximum flame shield total heating rates were three times (60-90 watts/cm^2) that of the heat shield maximum. A secondary peak occurred on the base where the reverse flow from the inboard engines becomes choked. Base gas temperatures varied widely with location on the base with a maximum probable value of 1100°C on the heat shield and 1800°C on the flame shield.

Base heat shield pressures were near ambient up to the altitude where reverse flow from the inboard engines became dominant. Above this altitude the base pressures were greater than the ambient. The flame shield pressure showed a similar trend to the heat shield; however, the variation from the ambient was much greater and, above the choking altitude, became relatively constant.

The effects of one inboard engine out were found to increase the flame shield heating rate and decrease the gas temperature and pressure level.

The successful acquisition of the base thermal environment data has made possible the establishment of measured base heating rates for multi-jet LOX-RP-1 propelled vehicles, and has served as a basis for developing improved methods of data measuring, reduction, and evaluation.

INTRODUCTION

The successful launching of the Saturn SA-4 flight vehicle concludes the Block I research and development tests of the Saturn I program, which consisted of four flights (SA-1 through SA-4) of the configuration shown in Figure 1. Since the primary mission of these flights was to check out the booster, the eight-engine cluster S-I stage shown in Figure 2 was the only live stage for these tests. The upper S-IV and S-V stages were dummy and carried water ballast to simulate the actual loading. The payload was a dummy Jupiter type nose cone and an S-V adapter section.

Block II vehicles, which begin with SA-5, have the configuration shown in Figure 1. The H-1 engines on these flights (SA-5 through SA-10) will be uprated from 165,000 pounds thrust to 188,000 pounds each on the booster stage. The second S-IV stage, which will also be live, will be powered by six RL-10 engines of 15,000 pounds thrust each.

The Block I vehicles were all launched from Complex 34 at Cape Kennedy, Florida. The SA-1 was launched on October 27, 1961, the SA-2 on April 25, 1962, the SA-3 on November 16, 1962, and the SA-4 on March 28, 1963. Early engineering evaluations of each of the Block I test vehicles are contained in References 1 through 4. The performance of each of the vehicle systems, giving special attention to deviations from expected operation and the occurrence of malfunctions, is emphasized. This report gives a more definitive presentation of the data obtained from the Block I flight tests for determining the base thermal environment. Data interpretation and the problems which are due to calorimeter design, mounting techniques, and calibration procedures are emphasized. The scope will be limited to measurements of the heating rates, gas temperatures, and pressures on the base heat and flame shields of the vehicles and will include all possible comparisons with model test data.

VEHICLE BASE CONFIGURATION

When the design of the Saturn engine cluster was conceived in 1958, the high base heating rates experienced in the Jupiter (Ref. 5) and other missile programs were fresh in mind, and attention was immediately focused on this aspect of the development.

The structural and propulsion designers of the initial engine configuration foresaw a circular engine arrangement. It was expected, however, that this circular arrangement would cause a pronounced recirculation of hot combustion products on the inside of the engine circle, as well as high radiative heat inputs in the same area. This reasoning was later confirmed by experience on the Polaris (Ref. 6). A cross-type configuration as shown in Figures 1 and 2 was therefore chosen. The four fixed engines were placed as closely together as possible at the center of the arrangement. The area remaining in the exit plane between the four nozzles was sealed with a flame shield to prevent the hot gases from circulating into the base area proper at higher altitudes. The hot recirculated gases and intense radiation expected between the inner engines was thus trapped in a small, easily protected area. The four movable outer engines were grouped about the four central engines at a distance which minimized, within design limitation, the potential jet interference.

To protect the engine compartment against the recirculating high temperature gases in a region forward of the flame shield, a base heat shield was placed on a plane perpendicular to the vehicle axis and approximately at the throat plane of the eight rocket engines. Since aerodynamic loads were not permitted on these engines, the outer engines were each protected by a shroud that extended beyond the heat shield. Scoops were placed on these shrouds and in the area between them to flush these regions of the heat shield with cool ambient air.

The gas turbine of the H-1 engine discharges a fuel-rich exhaust $(O/F \approx .33)$. Afterburning of the turbine exhaust gases caused high heating rates on the Jupiter missile when it was discharged into the base region. The inner engine turbine exhaust of the S-1 is dumped overboard through ducts which are located as shown in Figure 1. Since the gas generator and turbine are attached to the engine, discharge of turbine exhaust of the outboard (movable) engines into the ambient flow was mechanically difficult. Hence, the turbine exhaust gases are discharged with an exhausterator located around the exit of each outboard engine nozzle.

The heat shield consisted of an outer layer of aluminum reflective tape, a thin layer of low temperature subliner (T-500 Thermolag) and a filled phenolic epoxy (X-258) insulation which is bonded to the metallic portion or structural plate of the heat shield. A sketch of the heat shield cross section is shown in Figure 3a. The reflective tape was added to retard the sublining of the surface material due to the initial high radiation level associated with launch, and was not expected to survive the full flight time. Small patches of tape were observed to be loose on both SA-1 and SA-2 at lift-off.

Some difficulty was encountered before the SA-1 flight in obtaining a good bond between the reflective tape and the sublimer. Because the moisture absorbed by the base shield material caused the tape to pull away from the base structure, it was necessary to remove this tape and to apply new tape. Steps were taken to remedy this situation for the remaining Block I flights.

The flame shield consisted of a structural steel plate and an asbestos phenolic laminate (CT-301) insulating material. The cross section of the flame shield is sketched in Figure 3b. The gap between the flame shield and inboard engine nozzle wall is sealed so that the reversed gases do not pass directly to the base shield.

The area between the outboard engine walls and the heat shield is enclosed with flexible curtains having an outer layer of "Refrasil" cloth covered with reflective tape.

For the SA-3 and SA-4 flights, sample test panels of the material proposed for the Block II heat shield were used. Figure 3c shows the cross section of this heat shield design which incorporates an unfired ceramic (M-31) insulation which is nonpyrolizing.

FLIGHT TRAJECTORIES

Figures 4a, 4b, and 4c give the altitude, Mach number, and velocity as a function of flight time for the Block I vehicles. The trajectories of SA-1 and SA-2 flights were very similar in all respects. The SA-3 flight had a heavier lift-off mass due to a full propellant loading, resulting in lower values of the altitude, Mach number, and velocity for a given time than the other three flights. To minimize the effects of the trajectory differences, the data are plotted as a function of altitude for comparison. The SA-4 flight had a loading similar to SA-1 and SA-2; however, a slight deviation in the trajectory was caused by the programmed cut-off of engine number five at 100.6 seconds.

FLIGHT TEST INSTRUMENTATION AND REDUCTION OF THE DATA

The instrumentation used to measure the thermal environment of the base on the Block I vehicles is not considered representative of the "state of the art" at this time. The condition is due to a rather inflexible system of long

4

leadtime requirements for the pruchase and installation design of the instruments. Simple evolutionary changes have been made from flight to flight to improve the situation, but certain inherent losses in the instrumentation and calibration techniques preclude in the present data any attainment of a great degree of accuracy in the measurement of the thermal environment. More sophisticated instruments are being developed which are expected to eliminate some of the existing sources of error. Details of the problems involved and the present solution will be explained in later sections.

A. ACQUISITION OF DATA

The data used in this report were telemetered from the vehicle to various ground tracking stations and recorded on magnetic tape. It was then transferred to the MSFC Computation Laboratory for reduction and dissemination to the various engineering groups for evaluation. The thermal data were received as digital printout of the instrument temperature for every 0.1 second of flight time. Automatic plotters also supplied these same data in graphical form. Typical samples are given for the SA-2 flight in the results. The accuracy of the telemeter system of this type is given as ±5 percent of the full scale reading; however, for the Block I flights it appears that the accuracy is more probably ±2 to 3 percent of full scale.

B. BASE MEASUREMENT LOCATIONS

The locations of the instruments on the base of each of the Block I vehicles are shown in Figure 5. Measurements were obtained from three total and two radiation calorimeters, four gas temperature probes, and three flush mounted pressure orifices on the heat shield. A total calorimeter, a gas temperature probe, and a pressure orifice were located on the flame shield between the four inboard engines.

Radiation calorimeters C79-2 and C64-4 were located symmetrically with respect to the engine pattern near engines 2 and 6, and 4 and 5, respectively, but unsymmetrically with respect to the turbine exhaust ducts off fins II and IV. Assuming similar engine operation, each calorimeter should yield similar data except for the influence of control movements of the outboard engines and the possibility of unsymmetrical heating from the turbine exhaust ducts.

The same geometric situation exists for the total calorimeters C76-3 and C63-1 with the probable result of afterburning and engine movement affecting both the radiation and convective component measurements unsymmetrically. The location of gas temperature probes C10-2 and C10-4 behind engines 2 and

5

4 and the engine shrouds is approximately similar and should be influenced only slightly by engine movement and vehicle angle of attack. The remaining instruments are located individually, and cannot be compared except on a flight-to-flight basis and to show variations with location on the base.

Table I summarizes the instrument locations as to the symmetric placement of similar units and conditions which cause the gas flow over them to be unsymmetrical. A basis for making comparisons is also presented, and the instruments involved in determining certain evaluation quantities (convective heating rate, heat transfer coefficient, etc.) are listed.

C. TOTAL CALORIMETER MEASUREMENTS

The total calorimeter is an instrument designed to measure the heating rate caused by a convective fluid flow over its surface in addition to the absorption of radiant energy. The output of the calorimeter will then give the "total" or sum of the two types of heating. Typically, the total calorimeter is a slug of metal with a high value of thermal conductivity. It has a thermocouple mounted from the rear of the slug which measures the change in temperature of the slug with time. The slug, isolated from the surrounding structure to minimize heat conduction losses, has a surface finish with an emissivity approaching 1.0. For the ideal case with perfect isolation and with a slug temperature below the level where reradiation becomes significant, the equation for the total heating rate is simply

$$\dot{q}_T = C_p \frac{m}{A} \frac{dT}{d\theta} = \rho \, C_p \, t \, \frac{dT}{d\theta} , \tag{1}$$

where C_p = heat capacity of the sensor

m = thermal mass

A = active area of the thermal mass

ρ = density of the thermal mass

t = thickness of the mass

T = sensor temperature

θ = time.

6

A discussion of methods for evaluating calorimeter data and the procedure used in this report will follow; additional information will be given in Appendix A.

      1. <u>Heat Shield</u>. Three total calorimeters were installed on the heat shield at measurement locations C63-1, C77-5, and C76-3 as shown in Figure 5. A drawing of the calorimeter used on all the flights is given in Figure 6. The nine-inch pedestal and flush mounting of the calorimeters are shown in Figures 7, 8, and 9. Table II indicates for each flight how the calorimeter was mounted, its location, sensing element thickness, and whether it had a copper or nickel element. The surface of all sensing elements was coated with platinum black to give a high absorptivity.

      The evaluation of the base heating rates from these data has proved to be a difficult task. The isolation of the sensing elements of the calorimeters was not satisfactory since the twelve bolts shown in Figure 6 contact the sensing element, the casing, and the heat shield structure. Some isolation was obtained by the use of a small groove around the sensing element to act as a heat flow barrier (Fig. 6). It was also found from photographs taken on the launch pad that the methods of mounting varied from flight to flight. This situation produced additional errors which could not be accounted for by normal calibration means. Figures 10 and 11 indicate some of the mounting conditions found. Figure 10 shows total calorimeter C76-3 as flown on flights SA-3 and SA-4. For the SA-4 flight, an aluminum tape covered the pedestal and calorimeter bolts, whereas for SA-3 no tape was used. It is impossible to determine from the photograph if the tape covered the opening in the pedestal of SA-4. Laboratory tests (Ref. 7) have indicated that backside heating caused by hot gases circulating within the pedestal can have a marked effect on the calorimeter losses.

      Figure 11 indicates the situation for the flush-mounted calorimeters. For the SA-3 flight, calorimeter C77-5 was very neatly mounted in the M-31 panel and appears to have good edge contact with the M-31. The SA-4 flight calorimeter C63-1 appears to be very crudely installed with little edge contact, and part of the heat shield chipped away exposing the lower part of the calorimeter. These cases are typical of the mounting conditions which made an exact evaluation of the heating rates, regardless of the method used, virtually impossible.

      The calorimeters used on the SA-1, SA-2, and SA-3 flights were calibrated before the flight using an infrared quartz tube lamp-bank as a radiation source. The heat source was used for both radiation and total calorimeters. The source did not simulate combined radiation and convective heat flow which would be needed for the proper calibration of the total calorimeters. The heat shield structure was not simulated for the calibrations of these flights, but a

partial simulation was made for the SA-4 flight, which indicated sizeable differences for similar calorimeters when compared with the earlier flight calibrations. The results of experimental work in evaluating and comparing the total calorimeter losses are found in References 8 and 9. Additional analytical and experimental information on total calorimeters used in flight tests is found in References 10, 11, and 12, which verify the problems encountered in evaluating the heating rates on the Saturn I heat shield.

Another problem to be considered in evaluating the total slug calorimeter is that of the thermal boundary discontinuity on the heat shield surface caused by the presence of the calorimeter. Analytical investigations, such as References 13 and 14, have indicated that the calorimeter-measured heating rate may have large deviations from the actual heating rate to the heat shield. The referenced works consider ideal cases of incompressible laminar and turbulent boundary layer flow along a flat plate. The attempted application of these methods to correct the flight data would likely yield erroneous results, since the turbulent character of the base flow field is likely to reduce or eliminate these temperature mismatch effects (Ref. 15 and 16).

The total heat rate data presented in this report represent only the heating rate to the calorimeter surface which has been corrected for radiation and conduction losses, and should not necessarily be interpreted as the absolute value of the heating rate to the heat shield surface. It has generally been concluded that a slug type calorimeter can only be calibrated satisfactorily for its ability to measure the flow of heat into the slug for the specific heat source and mounting condition of the calibration. It cannot be calibrated in a manner that will accurately indicate the heating rate to the structure in which it is installed.

The method used for reducing the calorimeter time-temperature curves to heating rates employed an inflight calibration procedure. This accounted for the conduction losses at engine cut-off and applied this loss over the total flight time. A development of the method follows.

A heat balance equation can be written for the calorimeter slug to account for its losses:

$$Q_T = Q_s + Q_L \tag{2}$$

where Q_T = total heat absorbed by the slug

Q_s = heat stored in the slug

Q_L = heat lost by the slug.

Then

$$Q_T = Q_s + (Q_{rrL} + Q_{coL}) \qquad (3)$$

where Q_{rrL} = reradiation loss from slug surface

and Q_{coL} = conduction losses from the slug.

Expressing the equation in terms of a heating rate, and substituting equation (1) for the Q_s term, we obtain

$$\dot{q}_T = \rho \ C_p \ t \ \frac{dT}{d\theta} + \epsilon \ \sigma \ T_w^4 + K(T - T_i), \qquad (4)$$

which is the form suggested by Hottle and others. The temperature-time slope $\frac{dT}{d\theta}$ was obtained from telemetered flight data as shown in Figures 25, 28, and 31, etc. The obviously "wild" points were omitted, and a computer program determined a polynomial curve fit by a method of "least squares." These curves were then differentiated to obtain the slope. For the radiation term $\epsilon \ \sigma \ T_w^4$, the emissivity ϵ was taken at 0.9 since all the slug surfaces were blackened. The Stefan-Boltzman radiation constant is symbolized by σ, and T_w is the temperature of the slug.

The heat conduction losses are found by the evaluation of the loss coefficient K. The evaluation is made at the point of the inboard engine cut-off (IECO) where a sharp drop in the calorimeter temperature-time curve is observed. The outboard engine cut-off (OECO) had little or no effect on the curve, indicating a very low heating rate contribution due to these engines after inner engine cut-off. The value of $\dot{q}_T$ could then be assumed equal to zero in equation (4). Then $\frac{dT}{d\theta}$ will be equal to the slope of the temperature curve and T_w the slug temperature at inboard cut-off. The value of $(T - T_i)$ is taken as the temperature difference between lift-off and inboard engine cut-off. Here the assumption is made that the calorimeter casing temperature remained at the initial launch

temperature. This assumption is a conservative one since the case temperature will rise during the flight and the value of $(T - T_i)$ will decrease, thus yielding a lower conduction loss than that obtained under the constant casing temperature assumption. With all the quantities of equation (4) known for the engine cut-off condition, K can be evaluated:

$$K = \frac{\rho \, Cp \, t \, (\frac{dT}{d\theta})_{c-o} - \epsilon \, \sigma \, T^4_{w_{c-o}}}{(T_{c-o} - T_i)} . \tag{5}$$

The value of K is then inserted as a constant in equation (4), and the heating rates as shown under "Results" are calculated by a computer program. Reference 17 gives a more detailed discussion of the loss coefficient, along with an analytical derivation of the quantity.

Some confidence in this method over the preflight calibration procedure (see Appendix A) is indicated in Reference 18. A mathematical model of the total calorimeter was formulated, and the SA-3 flight heating rates obtained by the inflight calibration method were used as input to the model computer program which calculated the slug temperature of the calorimeter. This temperature compared well with the measured flight temperature data.

2. Flame Shield. A single total calorimeter measurement, C78-8, was made on the flame shield for each flight. A drawing of this calorimeter is shown in Figure 12, and an installation drawing showing its location relative to the fin reference lines is found in Figure 13. Figure 14 is a photograph of typical instrumentation on the flame shield. The data reduction procedure was identical to that described for the heat shield calorimeters.

D. RADIATION CALORIMETER MEASUREMENTS

Two slug-type radiation calorimeter measurements, C79-2 and C64-4, were flown on each of the Block I flights. The use of these measurements in the data evaluation can be found in Table I. Figure 5 shows their location on the heat shield. The calorimeters had minor design changes from flight to flight to improve their accuracy, such as increased view angle, better slug isolation, and an improved nitrogen purge system. Figures 15, 16, and 17 show the construction of the calorimeter used for each flight; Figure 18 shows the pedestal mounting installation used for all Block I flights. The flight conditions of each measurement are given in Table II; Figure 19 is a photograph of a typical radiation calorimeter mounted on a pedestal.

As seen in Figures 15 through 17, the radiation calorimeter consisted of a copper slug with a blackened surface enclosed behind a sapphire window to isolate the convective flow from the slug surface. A conical purge of high pressure nitrogen gas is used around the sapphire window to prevent the possible clouding over by the carbon particles circulating in the base region.

The radiation calorimeter, since it was of the slug type, was subject to the same losses as the total calorimeters, and the method used to evaluate the heating rate was identical to that used for evaluating the heating rates on the total calorimeters. Additional conditions existing in the radiation calorimeter make an accurate evaluation of the radiative heating rates even more difficult than that experienced with the total calorimeters.

The radiation calorimeters should have a wide directional sensitivity or view angle so as to respond to the total amount of radiation present in the base region. For the SA-1 flight, the calorimeter of Figure 15 had a total conical geometric view angle of approximately 114 degrees. This angle was increased to 130 degrees (Fig. 16) for the SA-2 flight as a result of a redesign of the nitrogen purge ducts to prevent cooling of the calorimeter slug by the purge gas. Further improvements (Fig. 17) of the purge system and view angle (150 deg), as well as better slug isolation, were incorporated in the calorimeter of location C79-2 for SA-3 flight, and both C64-4 and C79-2 used this instrument for the SA-4 flight. An experimental evaluation of the effects of the increased view angle for these calorimeters is found in Reference 19, which indicates that the factor required to correct the 150 degrees view angle calorimeter to 180 degrees was close to unity and uniform with respect to the distance from the radiating source. The other two designs showed larger correction factors and a sharper influence of the source location.

As mentioned above, the early purge design produced a cooling effect on the calorimeter slug which made evaluation more difficult. Calibration of the later designs indicated that this condition had been eliminated. Simple ground tests were performed with a blow torch which showed that the purge design was effective for the test conditions; but since no simulation of the actual flight conditions could be made, it is not known just how effective the purge is during the flight. It is possible that an increasing filtering effect is present in the data caused by a gradual build-up of carbon contamination on the sapphire windows.

The transmissive properties of the sapphire window also influence the output of the calorimeters in a manner which cannot be accurately evaluated with the test data available. Reference 17 shows that for normal radiation approximately 85 percent transmission was indicated out to a wavelength of 6 microns.

It was found that the nontransmitted energy at the shorter wave lengths is lost by reflection and the energy at the longer wave lengths is mostly absorbed by the sapphire. The laboratory calibration accounts for this loss based on a normal radiation from an infrared lamp; however, under flight conditions the radiation is from a nonuniform source, and the jet plume changes shape (Fig. 20), temperature, and spectral distribution as the altitude increases. For a valid correction to be made to the radiation calorimeters, these quantities would be required so that the losses from reflection and absorption could be evaluated. It is estimated that if the correction could be made it may be 15 percent or more for some conditions. Because of the complexity of obtaining the required data for this correction, it was not considered practical to include it in the measuring program, and the radiation data presented have not included any correction for the window transmissivity. Additional information in this area is found in Appendix B.

E. GAS PROBE MEASUREMENTS

In an effort to determine the temperature of the gases circulating in the base area, six gas probe measurements were made on the heat shield and one on the flame shield on each flight. Figure 5 indicates the locations of measurements C10-2, C10-4, C10-7, C65-3, C67-7, and C93-7. The mounting conditions of the probes are summarized in Table II; a drawing of the types of probes used is found in Figure 21. The SA-1 probe shown in Figure 21a had its thermocouple junction enclosed in a double-walled radiation shield which protected it from high temperature gases, and made it very sluggish in its response to rapid changes in temperature. For the SA-2 and subsequent flights, the design was altered as shown in Figure 21b, and a satisfactory response was obtained. The bracket was placed above the probe for the same measurements (Table II) not only to protect the instrument from damage during installation on the launch pad, but also to serve as a normal radiation shield for the thermocouple junction.

The probes were either flush-mounted on the heat shield or flame shield, as shown in the photographs in Figures 14 and 22, or located on a pedestal whose mounting surface was nine inches above the heat shield surface as shown in Figure 19.

The sensing elements of the heat shield probes were chromel-alumel junctions; the flame shield probe used a platinum-platinum 10 percent rhodium junction since the temperatures in this region exceeded the level at which the heat shield junctions could function.

12

F. PRESSURE MEASUREMENTS

The base pressure was measured on the aft surface at three locations on the heat shield (D25-4, D25-7, and D38-4) and one location on the flame shield (D38-7) as indicated in Figure 5. A typical pressure orifice is shown on the photograph of the flame shield in Figure 14. The pressure, which was measured using an absolute transducer with a 0 to 13.8 N/cm^2 range, had a possible error of ± 2 percent full scale (± 0.276 N/cm^2). This range was required since pressures must be measured at ground level, as well as at high altitudes. Since the transducer error at attitudes above 25 km (approximately) was the same order as the measured pressures, the data above this altitude are questionable. It is desirable that future base pressure installations have dual range instruments and Δ P-type transducers to increase the accuracy of measurements.

RESULTS

The following sections compare the results of each environment-type base flight measurement on a flight-to-flight basis with the altitude as a variable. For the heating rate data, a flight comparison of the calorimeter slug temperature is shown. For each measurement, typical telemetered flight data are shown for SA-2 as plotted with an automatic x-y plotter at 0.1 second increments. These plots, which show quite well the magnitudes of data scatter, are typical of all the flights.

A. TOTAL HEATING RATES ON THE BASE

1. <u>Heat Shield Heating Rates</u>. The three total heating rate measurements on the heat shield are found in Figures 23 through 31. Measurements C76-3 (Fig. 23 through 25) and C63-1 (Fig. 26 through 28) were made in the inner region of the base, symmetrical with respect to engines 3 and 1. Measurement C77-5 (Fig. 29 through 31) was made in the outer region of the base between engines 1 and 4.

The total heating rate data shown for the base calorimeters have the same general trend with increasing altitude. The initial high value at lift-off is caused by the launch procedure of holding the vehicle in position on the launch pad for some three seconds until all the engines have approached full thrust. This procedure creates a high radiation level on the base which is due to the engine exhaust impingement on the launch deflector. After lift-off the total

heating rate drops sharply as the normal radiation at low altitudes from the engine plume is recorded. Starting at approximately 10 km (Fig. 20, picture 4), the total heating rate begins to increase as the reverse hot gas flow from the inboard engines produces a convective flow in the base region. At about 20 km (Fig. 20, picture 5), the reversed flow from the inboard engines has reached a choked condition, and the peak heating of the inflight condition is obtained. Above this point the rapid expansion of the rocket plume causes a cooling of the exhaust gases and a reduction in the radiation level as shown by the decreasing value of the total heating rates.

The wide variations in the data cannot be analyzed in detail because of the many factors that influence the final results. If we with the aide of Table II, undertake to establish the effects on the data of the mounting condition (flush versus pedestal), no conclusive trends can be established possibly because of a randomly turbulent flow as explained in References 15 and 16. In Figure 29 for measurement C77-5, it is observed that for a flush mount in an M-31 panel the heating rate for SA-4 is lower than SA-3 at cut-off by a factor of 4. When the "as flown" measurement photographs were checked, the mounting conditions were the same as those shown in Figure 11. This variation in the mounting is suspected, at least in part, for the large difference in the heating rates. However, looking at the data for the measurements shown in Figure 11 (C77-5 for SA-3, and C63-1 for SA-4), which were located near each other, we see in Figures 23 and 26 that, at SA-4 cut-off, measurement C77-5 is higher by a factor of only 1.15 over measurement C63-1. This illustrates the advantage of making measurements on a number of flights so that a mean value of the base thermal environment can be established.

The heat rate data are presented in Figures 23b, 26b, and 29b as a function of flight time for better detail in the low altitude region. These curves should not be used for a comparison between flights since the trajectory conditions between them differ.

Figures 24, 27, and 30 give the calorimeter slug temperatures for each flight. The part of the curve past the inboard engine cut-off point was the portion used to evaluate the loss coefficient term used in determining the flight heating rates.

A sample of the telemetered SA-2 flight data for the three measurements is shown in Figures 25, 28, and 31. These temperature-versus-time curves are typical of the measurements in shape and magnitude of the data scatter of all the Block I flights.

14

2. <u>Flame Shield Heating Rate</u>. The area between the four inboard engines was expected to have unusually high heating loads, and unless special protection was applied in this area, structural failures may have resulted. A flame shield, shown in Table I and Figures 1 and 2, was placed between the inboard engines. A cross section of the material used is found in Figure 3b.

Details of the flame shield measurement C78-8 are given in Figures 12, 13, and 14. The total heating rate on the flame shield is presented in Figure 32. The slug temperatures are found in Figure 33 and a sample of the SA-2 telemetered data in Figure 34.

In Figure 32 the maximum total heating rate observed at lift-off is three times the value found for the heat shield area. After clearing the launch pad, the level decreases rapidly and the flow assumes a condition as shown for the low altitude condition in Figure 35. As the altitude increases, there is the gradual change into the flow condition that is shown for high altitudes in Figure 35. The plume expansion of the four inboard engines results in the interaction of their wakes and the formation of a standing shock. A reversal of the flow which takes place impinges on the flame shield area and causes the heating rate in this area to again increase. The reversed flow is forced out between the engines and parallel to the flame shield surface as shown in the third sketch of Figure 35. As the altitude continues to increase, the critical pressure ratio is reached, and the flow becomes choked in the minimum area between the engines. Additional discussion of this condition is found in section IV-D. It is believed that the peak heating rate found at approximately 8 km occurs before the arrival of the fully choked flow condition, since it would be expected that the heat rate would become relatively constant above the choking altitude. This seems to occur between 15 and 20 km in Figure 32 and is indicated in much of the other data discussed in section IV-D. The rapid decrease in the heating rate prior to this choked condition is not fully understood; however, based on the simulation tests of Reference 18, part of the decrease can be accounted for. It was found that above 650°C, the platinum blackened surface of the calorimeter was burned off, greatly altering the absorptive and emissive properties of the calorimeter slug used for calculating the heating rate. This temperature agrees well with the point at which the flight slug temperatures shown in Figure 33 begin to flatten. The extent of the change would be difficult to determine since the actual condition of the slug is unknown. The heating rate rise at 35 km for SA-4 was due to the shutdown of the number 5 inboard engine.

B. RADIATION HEATING RATES

The two radiation measurements made on the Block I vehicles C79-2 and C64-4, which were located in symmetric locations with respect to engines 2 and 4 as shown in Figure 5. The data are summarized in Figures 36 through 41. The measured heating rates for C79-2 and C64-4 are given in Figures 36 and 39, respectively. The data shown have been evaluated using the inflight calibration method as explained in section III-D; no corrections have been included for the window transmissivity loss or the effects of the variable view angle of the calorimeters. The apparent effect of the view angle is seen in Figures 37 and 40. The heating rates for the 150 degree view angle calorimeter were generally higher than the data from the flights with the smaller 130 and 114 degree view angles. However, measurement C79-2 of the SA-1 flight with the 114-degree view angle was actually higher over most of the flight than the SA-2 data for a 130-degree view angle. At the smaller view angles other factors may offset the effects of the change in angle. The slug temperature data in Figures 37 and 40 present a consistent picture for the effects of change in view angle regardless of the various slug thicknesses which alter the temperature levels shown. Rather consistent temperature data are observed with the exception of measurement C64-4 on the SA-4 flight. It appears that some undetermined obstruction or temporary purge failure caused the calorimeter slug to experience a heat loss from approximately 3.5 to 35 km altitude. It then returned to a value quite close to that of C79-2 and at cut-off had nearly the same cooling rate. The resulting heating rate curve shown in Figure 39 is not to be considered valid, but is only shown to illustrate that seemingly satisfactory data from the electrical and acquisition standpoint can yield results which deviate widely from established levels.

The trend of the radiation data is seen to be similar to that of the total heating rates since the radiation is a component of the total heating. After lift-off the high radiation, created by proximity to the launch pad, decreases rapidly. As altitude increases, radiation continues to decrease until luminous regions appear in the jet impingement boundaries. These regions are created by the plume expansion and reversed flow process of the inboard engines (Fig. 35). The radiation heating rate again increases until the reverse flow of the inboard engines has reached a choked condition. Beyond this point the radiation decreases to a relatively constant level.

C. GAS PROBE TEMPERATURES

Gas probe temperatures were measured at five locations on the heat shield and one location on the flame shield (Fig. 5). The data for each flight

at a particular measurement location along with a sample of the SA-2 telemetered data are found in Figures 42 through 53.

Similar gas temperature measurements, C10-4 and C10-2, located between the outboard engines 4 and 2 and the engine shrouds, are shown in Figures 42 and 44. The temperature level at the two locations compares quite well, with the exception of C10-2 for the SA-2 flight where wide oscillations in the temperature are noted up to an altitude of 10 km. The data shown for the SA-1 flight should not be considered as a true measurement since a double shielded probe ·was used which made its response very poor. The temperatures increase at a rapid rate up to the point where the reversed flow from the inboard engines becomes choked. Beyond this point a decrease in temperature is observed. In Figure 42 the calculated free stream total temperature is compared with the gas temperatures and found to be lower up to an altitude of 30-35 km.

Temperature measurements C10-7 and C65-3 in the open base area are shown in Figures 46 and 48. These temperatures reach peak levels as high as 1150°C, some 300°C higher than the measurements made behind the shrouds. This difference indicates that either the hot gases do not circulate well behind the shroud or the air scoops mounted on the shrouds cool the gas effectively. Since at the high altitudes the temperature difference is approximately the same and the scoops are not expected to be effective under these conditions, it is suspected that only a small amount of the exhaust gases is found in the shroud region.

The mounting conditions of measurements C10-7 and C65-3 were dissimilar in that C10-7 was a flush-mounted instrument (thermocouple 1.5 inches off the heat shield surface) and C65-3 was on a 9-inch pedestal. The mounting positions do not reflect any appreciable change in the temperature level.

One additional gas temperature measurement C93-7 was made on the heat shield from a pedestal mount located beneath the flame shield in the space between adjacent inboard engines. The peak temperature compares well with the measurements C10-4 and C10-2. After the choked condition occurred in the flame shield region the temperature decreased more slowly than in the shroud area and reached a temperature level somewhat higher.

A single gas temperature measurement C67-7 was flush-mounted to the flame shield, the results of which are given in Figures 52 and 53. Some difficulty was encountered in obtaining data from this measurement. However, only data from the SA-1 flight were considered totally unreliable. The peak temperatures were not measured for any of the flights since the recording range

was set for 0 to 1500°C. As shown in Figure 53 when the upper limit is reached, a constant temperature is recorded until the actual temperature drops below the limit line. The extrapolations shown in Figures 52 and 53 were based on the shape of the curves and recent Block II data which had an upper range limit of 1750°C. The actual peak temperature is estimated to be approximately 1800°C which is 100°C above the maximum level that platinum-platinum 10 percent rhodium thermocouple junctions are designed to operate. The erratic behavior of the data after the peak temperature has been reached for the SA-3 and SA-4 flights indicates a failure of the junction because of melting. In the SA-3 flight, there appears to have been a re-fusing of the junction, and the temperature after recovery compared very well with the SA-2 data which showed no indication of a junction failure. The SA-4 data showed a more pronounced junction failure after the peak temperature was reached. The re-fusing or partial re-fusing of the junction must have taken place at the surface of the thermocouple stem or within the stem, since indicated temperatures are much lower and do not follow the other measurement trends in this region.

The constant level of the gas temperature after the reverse flow has choked in the flame shield would seem to be reasonable since the total heating rate also levels off above the choked altitude. At this altitude and above, the unburned carbon particles in the exhaust plume do not have sufficient oxygen from the atmosphere to afterburn and so are introduced into the inner restricted flame shield area as hot unburned carbon. Figure 35 shows that, after choking has occurred in the flame shield region, it becomes relatively isolated from the external influences of changes in altitude and velocity. The plume in this region will retain a fixed shape since the pressure in the flame area reached a constant value (Fig. 59). The conditions in this region can be considered in a state of thermal and flow equilibrium with the carbon particles radiating at a constant level and with a constant rate of hot gases flowing out over the flame shield producing a uniform convective heat rate at a given location on the flame shield. For the SA-4 flight this condition was disrupted by the shutdown of the number 5 engine at 100.65 seconds which resulted in an increased heating rate (Fig. 32). The flame shield temperature for SA-4 was not reliable, and current Block II data indicate a sharp drop in the temperature and then a leveling off at a lower level with one inboard engine out.

D. BASE PRESSURES

Three pressure measurements were made on the heat shield (D25-4, D25-7, and D38-4) and one on the flame shield (D38-7) as shown in Figure 5. The three heat shield absolute pressures are compared in Figure 54 for the SA-4 flight. The figure indicates the accuracy of the measurements, and it is

seen that above 25 km the range of the measurement accuracy is the same order as the pressures measured. Also, the variations in one measurement exceeded the differences caused by the location on the base and the best value of the base pressure would be the arithmetic average of the three measurements. Figure 55 shows a sample of the uncorrected telemetered data for D38-4 for the SA-2 flight. The maximum scatter for these data is approximately ±0.24 N/cm^2, which is within the ±0.276 N/cm^2 accuracy given for the gage. The average base pressure for the Block I vehicles is shown in Figure 56. To see how these pressures vary with respect to the ambient pressure (Fig. 57) the base pressure was ratioed to the ambient pressure (Fig. 58). For the region up to the choking altitude the data differ; SA-1 and SA-3 flights indicate a base pressure higher than the ambient, and for SA-2 and SA-4 flights the pressure is slightly lower than ambient indicating an injector effect over the base. Above the choking altitude, the ratio increases. This indicates that the reversed flow from the inboard engines is feeding into the heat shield area.

The flame shield pressure measurement D38-7 is given in Figures 59 through 62. A very good comparison of the absolute pressure for all flights except SA-3 was obtained (Fig. 59). The SA-3 data between 2.5 and 25 km are questionable. The flame shield pressure decreases in a manner similar to the heat shield pressure up to the point where the reverse flow from the flame shield becomes choked. At this point the flame shield pressure remains relatively constant as the altitude increases. For all the flights there was an equivalent altitude variation of only 13.0 to 14.5 km on the flame shield. The data shown for SA-4 indicate the effects of one inboard engine out of operation on the flame shield pressure. The sharp drop in pressure at 35 km is the result of the shutdown of the number 5 engine. This drop is equivalent to a rise in altitude on the flame shield from 13.2 to 21 km. The flame shield pressure is ratioed to the ambient pressure in Figure 60. The figure indicates an injector-type pumping action of the ambient air (Fig. 35) for low altitudes. This action continues from lift-off to an altitude of 11 to 12 km at which time the flow in the flame shield area is reversed and the pressure begins to drop more slowly than do the ambient and base pressures.

One additional curve has been found useful in evaluating the flow behavior in the base region. Figure 61 shows the ratio of the flame shield pressure to the average base heat shield pressure. This curve is equivalent to the pressure ratio across a supersonic nozzle with the space between the inboard engines taken as the nozzle throat, the flame shield pressure as the reservoir, and the base pressure as the downstream conditions. The critical pressure ratio, or the condition where Mach one is reached in the areas between adjacent inboard engines, is found at some point along the curve. This will define the altitude

at which the inboard engine reverse flow becomes fully choked and at which the maximum possible mass of hot gas is introduced into the heat shield area. The critical pressure ratio is defined as

$$\left(\frac{P_0}{P_1}\right)_{crit} = \left(\frac{\gamma + 1}{2}\right)^{\frac{\gamma}{\gamma - 1}} = \left(\frac{P_F}{P_{\overline{B}}}\right)_{crit} , \qquad (6)$$

where P_0 = reservoir pressure

P_1 = downstream pressure

γ = specific heat ratio for the hot exhaust gases (assumed to be 1.23)

P_F = flame shield pressure

$P_{\overline{B}}$ = average base pressure.

Then the critical pressure ratio for the above assumption is equal to

$$\frac{P_F}{P_{\overline{B}}} = 1.79.$$

The data shown for SA-1, SA-2, and SA-4 in Figure 61 for this ratio would indicate that the flow chokes between 16.9 and 19.2 km. Confirmation of this range is derived from the observation of the absolute flame shield pressure of Figure 59, the temperature of Figure 52, and the total heating rate of Figure 32. All these data indicate that choking occurred between 15 and 20 km altitude. In a later discussion experimental model results also confirmed this range.

E. CORRELATION OF FLIGHT MEASUREMENTS WITH MODEL TESTS

In the course of the design of the Saturn I flight vehicle, a considerable effort was expended in model tests to determine the base heating characteristics of the design and to supply data which would be useful in determining the required heat protection for the base area. A number of test programs in facilities at the Lewis Research Center, Arnold Engineering Development Center, and the Cornell Aeronautical Laboratory were conducted over a three-year period. It is beyond the scope of this paper to make a detailed evaluation and correlation of all the flight and model data available; however, representative

20

comparisons of total heating rates, radiation heating rates, base gas temperatures, and base pressures are presented. To obtain a background for the procedures and methods used in the model tests, a review of the published results found in References 21, 22, 23, 24, 25, 26, 27, 28, and 29 would be helpful.

1. Base Heating Correlation. The problems involved in devising a base heating "hot jet" model which will closely simulate actual flight conditions and yield data directly comparable are legion. For example, Figure 63 compares radiation heating rates taken from AEDC and Cornell tests on an S-1 booster 5.47-percent scale model with Block I flight data at approximately the same location on the base. Both the flight and AEDC measurements, and a procedure using equation (4) was employed for obtaining the heating rates. The Cornell data were obtained by a totally different procedure using thin-film resistance gages on a short duration test technique model. The model heating rates shown are all for a sensor temperature of 38°C; whereas, the flight data varied up to a value of 325°C. From a radiation standpoint, the model turbine exhaust flow simulation was poor since hydrogen gas was used for all the model tests. During flight the engine turbine exhausts a kerosene fuel-rich mixture (O/F $\approx$ .33) which has significantly different radiation characteristics from the model simulation. Basic gas laws indicate that similarity between the model and full scale exists only when the exhaust plumes are optically thin and when the products of a linear dimension and density are identical for both. The Saturn plume is far from optically thin, and at altitudes up to about 10 kilometers the radiation is predominantly due to secondary combustion of the fuel-rich engine exhaust with air. This process is influenced by scale, and the plume geometry of the model deviates significantly from the flight plume. It is indeed remarkable, considering all the negative factors involved, that the model and flight data shown in Figure 63 compare so well.

The total heating rate on the base with model data are compared in Figure 64. The model data have been corrected for the calorimeter losses by the same procedure as the radiation data. The convective component of the data is subject to additional correction for scale effects before a valid comparison is possible. The proper scaling procedure for this type of base flow has been very difficult to determine, and additional effort in this area is needed. The present data have been corrected on the basis of References 30, 31, and 32. A correlation equation was developed for heat transfer on the rear of bodies in separated flow, which indicated that the Nusselt Number is proportional to the Reynolds Number to the two-thirds power. The scaling method used is discussed in the Appendix C. The equation used for correlating the convective heating rates is

$$\dot{q}_{c_{flt}} = \left[\left(\frac{D_{mod}}{D_{flt}} \right)^{\frac{1}{3}} \frac{(T_R - T_w)_{flt}}{(T_R - T_w)_{mod}} \right] \dot{q}_{c_{mod}} \quad , \qquad \qquad (7)$$

where $\dot{q}_{c_{flt}}$ = convective component of the flight measured heating rate data

D_{mod} = diameter of the model base

D_{flt} = diameter of the flight vehicle base

$(T_R - T_w)_{mod}$ = Recovery temperature minus calorimeter temperature for the model

$(T_R - T_w)_{flt}$ = recovery temperature minus calorimeter temperature for the flight vehicle, $T_R = T_{gas}$ for the flight data

$\dot{q}_{c_{mod}}$ = model convective heating rate data.

After the scaling, equation (7) was applied to the convective component of the model data, the radiation was then added, and the total value plotted (Fig. 64). Although comparison with the range of the Block I data is good, the spread of the data in both cases is rather large.

Flight and model base gas temperatures are compared at approximately the same location in Figure 65. The model data required no correction and follows well the Block I measurement of C65-3 up to the altitude where reverse flow becomes a factor. Beyond this altitude the model gas temperature decreases; this indicates that there is less burning of the simulated turbine exhaust flow in the base or that less of the hydrogen turbine exhaust gas reaches the base of the model. It is believed that, from this critical altitude on up, scale effects prohibit burning of the turbine exhaust in the base area of the models, while it still continues on the flight vehicle.

2. Base Pressures. Pressures were measured at various locations on the base of all model tests; average base pressure ratios were obtained and compared with the flight results in Figures 58, 60 and 61. The model data for the base-to-ambient-pressure ratio of Figure 58 indicate generally lower

22

pressure for all the model tests up to the point of the inboard flow reversal. Above this altitude the model data indicate a higher pressure than the flight data. The differences can be attributed to the mismatch of the flow boundary conditions upstream of the model base and the improper scaling of the flow deflectors and air scoops to the model boundary layer conditions (they were scaled geometrically from the flight dimensions).

The flame-shield-to-ambient-pressure ratio model data are compared to flight in Figure 60. The comparison of the data in this region is very good over the whole model test range. This is due in part to the small influence of the external flow conditions on this region and to the similarity of the model engine and flight plume shapes. The flame shield to the base pressure ratio data shown in Figure 61 also compared well with the model data. By using this and additional experimental data found in Reference 33, the critical or choking altitude was found to be 18.75 km for a critical pressure ratio of 1.72. If the critical pressure ratio were taken as 1.79, as shown in Figure 61, the choked condition would first occur at an altitude of 17.5 km. Both these values fall within the range indicated by the flight data in the previous section.

F. HEAT TRANSFER COEFFICIENTS

The result of the base heating rate and gas temperature measurements is the determination of a base heat transfer coefficient which can be used in the design of the heat shield protective material. The reliability of each measurement will influence the resultant value of the coefficient and ultimately the degree of conservatism of the heat shield design and the payload capability of the flight vehicle.

The heat transfer coefficient is defined for flight data by the following equation:

$$h = \frac{(\dot{q}_T - \dot{q}_R)}{(T_g - T_w)} = \frac{\dot{q}_c}{(T_g - T_w)} , \qquad (8)$$

where h = vehicle heat transfer coefficient, watts/cm^2-°C

$\dot{q}_T$ = total calorimeter heating rate, watts/cm^2

$\dot{q}_R$ = radiation calorimeter heating rate watts/cm^2

$\dot{q}_c$ = convective difference between the total and radiation heating rates, watts/cm^2

T_g = gas temperature in the same relative location as the total calorimeter, °C

T_w = temperature of the total calorimeter slug, °C.

The heat transfer coefficient was calculated for each flight on the basis of the sample data given in Figure 66. By using the measurements shown in this figure, which are located in the same relative position on the base, the heat transfer coefficient was calculated at various positions along the trajectory. Then, from Figure 66,

$$h = \frac{\dot{q}_c}{(T_g - T_w)} = \frac{[\text{Meas. (C76-3) - Meas. (C79-2)}]}{[\text{Meas. (C65-3) - Meas.(C76-3)}]} . \qquad (9)$$

Normally, the value of h should be in a positive sense relative to the heat shield. At low altitudes the inflow of ambient air to the base results in a convective cooling ($\dot{q}_T < \dot{q}_R$ yields $-\dot{q}_c$). The high lift-off radiation level initially raises the wall temperature above the gas temperature ($T_g - T_w$ is $-$), and a positive value of h is obtained. The data have not been completely consistent with the above, since at the low altitude the wall and gas temperatures are close to the same value and the data scatter is sufficient to cause ($T_g - T_w$) to become positive while $\dot{q}_c$ remains negative and a minus h results. The negative values of h were not considered in Figure 67 but only a smoothed composite curve of all the flight heat transfer coefficients is compared to the corrected model heat transfer data. As explained in Appendix C, the model data are correlated to the flight data by the equation

$$h_{flt} = .378 \left(\frac{\dot{q}_c}{T_r - T_w}\right)_{mod} = .378\, h_{mod}, \qquad (10)$$

where T_r = the model recovery temperature at $\dot{q}_c = 0$,

$\dot{q}_c$ = convective heating rate measured on the model at $T_w = 38°C$,

T_w = calorimeter slug temperature = 38°C.

The model data are plotted for the particular test altitudes that simulated the flight trajectory as shown in Figure 67. Considering the complexity of evaluation and the averaging procedures employed, the excellent comparison of the data is encouraging and adds some additional degree of confidence in the model test results.

CONCLUSIONS

The following remarks are made concerning the measurements which defined the thermal environment on the base of the Saturn I, Block I vehicles:

1. The data acquisition for the measurements was on the whole considered satisfactory. There were very few cases where measurements were lost or erroneous data obtained because of malfunction of the telemeter system or thermal instrumentation.

2. Although the evaluation of the heating data has indicated large variations for similar measurement locations and flight trajectories, it has been possible to establish broad total base heating rate and gas temperature levels that can be expected to exist in the base of multi-engine, LOX/RP-1 propelled vehicles.

3. Similarly, the radiation data experienced large changes in level from flight to flight (due in part to improvements in the calorimeter design); however, the data indicated a consistent trend and valuable information was obtained on plume radiation attenuation with altitude.

4. The experimental model results had many instrumentation problems similar to the flight vehicle, in addition to those of scaling and simulation, which were responsible for the large data scatter band. Comparison of the model results with the flight results showed that similar trends existed and the level and scatter of the data were of the same order of magnitude.

5. The methods and procedures used for evaluating the thermal environment have resulted in a minimum scatter of data--the least that could be expected, possibly, considering the types, installation and limitations of the thermal instrumentation used. The experience gained during these flights has influenced the selection of instrumentation for future Saturn vehicles which are expected to reduce the data scatter and eliminate many of the evaluation problems previously discussed.

TABLE I INSTRUMENTED LOCATIONS REFERENCED FOR DATA COMPARISON AND EVALUATION

BASIS ON WHICH DATA CAN BE COMPARED OR EVALUATED	SYMMETRICAL WITH RESPECT TO	UNSYMMETRICAL WITH RESPECT TO	RADIATION MEASUREMENT	TOTAL MEASUREMENT	GAS MEASUREMENT	PRESSURE MEASUREMENT
FOR EACH FLIGHT AND FROM FLIGHT TO FLIGHT	ENGINE NO. 2 & 4	TURBINE EXH. NO. 2 & 4 *	C79-2 C64-4	—	—	—
FOR EACH FLIGHT AND FROM FLIGHT TO FLIGHT	ENGINE NO. 1 & 3	TURBINE EXH. NO. 1 & 3 *	—	C76-3 C63-1	—	—
FOR EACH FLIGHT AND FROM FLIGHT TO FLIGHT	ENGINE NO. 2 & 4 T.E. NO. 2 & 4	*	—	—	C10-2 C10-4	—
BASE GAS TEMP. VARIATION OVER BASE COMPARED FOR EACH FLT. & FROM FLT. TO FLT.			—	—	C10-7 C93-7 C65-3	—
FLAME SHIELD TEMP COMPARED FROM FLT. TO FLT.			—	—	C67-7	—
HEAT RATE, TEMP & PRESS. AT A POINT, DETERMINE CONVECTIVE HEATING & HEAT TRANSFER COEF. FROM FLT. TO FLT.	ENGINE NO. 2,1,3 & 4 T.E. NO. 2,1,3, 4	*	C79-2	C63-1	C65-3	D25-4
COMPARE CONVECTIVE HEATING RATE FROM FLT. TO FLT.	ENGINE NO. 4 & 3 T.E. NO. 4 & 3	*	C64-4	C76-3	—	—
COMPARE CONVECTIVE HEATING RATE FROM FLT. TO FLT.	ENGINE NO. 2 & 3	T.E. NO. 2 & 3 *	C79-2	C76-3	—	—
COMPARE CONVECTIVE HEATING RATE FROM FLT. TO FLT.	ENGINE NO. 1 & 4	T.E. NO. 1 & 4 *	C64-4	C63-1	—	—
FLAME SHIELD TOTAL HEAT RATE COMPARED FROM FLT. TO FLT.				C78-8	—	—
DETERMINE AVERAGE BASE PRESSURE, COMPARE FROM FLT. TO FLT. AND VARIATION FOR EACH FLIGHT						D38-4 D25-4 D25-7
COMPARE FLAME SHIELD PRESSURE FROM FLT. TO FLT. AND WITH BASE PRESSURE						D38-7

* THE INSTRUMENTS IN QUESTION COULD HAVE DISSIMILAR READINGS DUE TO DIFFERENT GIMBAL PATTERNS OF ADJACENT OUTBOARD ENGINES
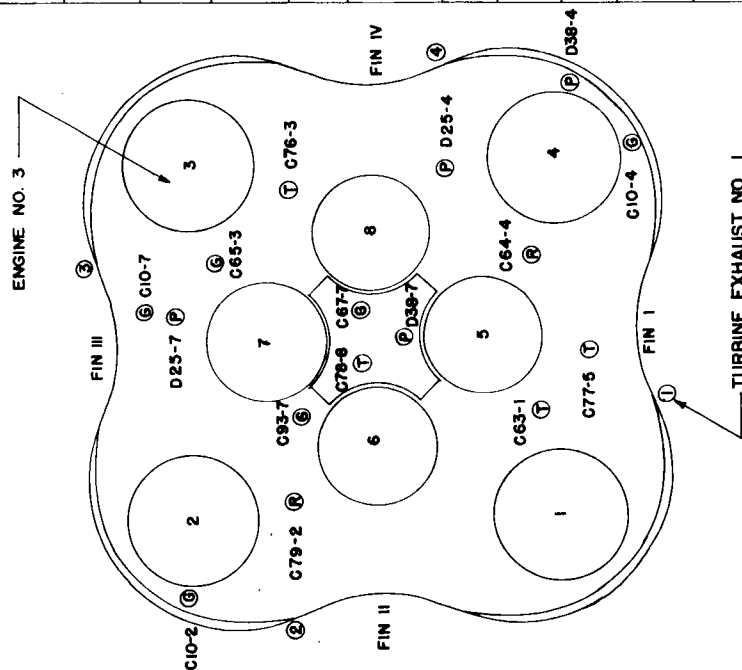
TABLE II TABULATION OF BASE HEATING INSTRUMENTATION FOR S-I STAGE OF SATURN I BLOCK I VEHICLES

CALORIMETER NUMBER	TYPE	SENSING ELEMENT	SLUG THICKNESS	METHOD MOUNTED	LOCATION
SA-1					
C63-1	TOTAL CALORIMETER	COPPER SLUG	.12 IN.	FLUSH	HEAT SHIELD
C77-5	↓	↓	.12 IN.	PEDESTAL	↓
C76-3	↓	↓	.12 IN.	PEDESTAL	↓
C78-8	↓	↓	.60 IN.	FLUSH	FLAME SHIELD
C79-2	RADIATION CALORIMETER	↓	.126 IN.	PEDESTAL	HEAT SHIELD
C64-4	RADIATION	↓	.126 IN.	PEDESTAL	↓
C10-2	GAS TEMPERATURE PROBE	CHROMEL-ALUMEL THERMOCOUPLE	——	FLUSH — PROTECTIVE BRACKET OVER DOUBLE SHIELD	↓
C10-4	↓	↓	==	↓	↓
C10-7	↓	↓	==	↓	↓
C65-3	↓	↓	——	PEDESTAL, NO BRACKET	↓
C93-7	↓	↓	——	PEDESTAL, NO BRACKET	↓
C67-7	↓	PLATINUM-PLATINUM 10% RHODIUM	——	FLUSH — DOUBLE SHIELDED	FLAME SHIELD
SA-2					
C63-1	TOTAL CALORIMETER	NICKEL SLUG	.12 IN.	FLUSH	HEAT SHIELD
C77-5	↓	COPPER SLUG	.12 IN.	PEDESTAL	↓
C76-3	↓	↓	.12 IN.	PEDESTAL	↓
C78-8	↓	↓	.60 IN.	FLUSH	FLAME SHIELD
C79-2	RADIATION CALORIMETER	↓	.14 IN.	PEDESTAL	HEAT SHIELD
C64-4	RADIATION CALORIMETER	↓	.14 IN.	PEDESTAL	↓
C10-2	GAS TEMPERATURE PROBE	CHROMEL-ALUMEL THERMOCOUPLE	——	FLUSH — PROTECTIVE BRACKET AND RING	↓
C10-4	↓	↓	==	↓	↓
C10-7	↓	↓	==	↓	↓
C65-3	↓	↓	——	PEDESTAL, NO BRACKET	↓
C93-7	↓	↓	——	PEDESTAL, NO BRACKET	↓
C67-7	↓	PLATINUM-PLATINUM 10% RHODIUM	——	FLUSH — PROTECTIVE RING	FLAME SHIELD
SA-3					
C63-1	TOTAL CALORIMETER	NICKEL SLUG	.12 IN.	PEDESTAL	HEAT SHIELD
C77-5	↓	COPPER SLUG	.12 IN.	FLUSH, M-31 PANEL	↓
C76-3	↓	↓	.12 IN.	PEDESTAL	↓
C78-8	↓	↓	.60 IN.	FLUSH	FLAME SHIELD
C79-2	RADIATION CALORIMETER	↓	.14 IN.	PEDESTAL	HEAT SHIELD — 150° VIEW ANGLE
C64-4	RADIATION CALORIMETER	↓	.27 IN.	PEDESTAL	HEAT SHIELD
C10-2	GAS TEMPERATURE PROBE	CHROMEL-ALUMEL THERMOCOUPLE	——	FLUSH — PROTECTIVE RING	↓
C10-4	↓	↓	==	↓	↓
C10-7	↓	↓	==	↓	↓
C65-3	↓	↓	——	PEDESTAL, PROTECTIVE RING	↓
C93-7	↓	↓	——	PEDESTAL, PROTECTIVE RING	↓
C67-7	↓	PLATINUM-PLATINUM 10% RHODIUM	——	FLUSH; PROTECTIVE RING	FLAME SHIELD
SA-4					
C63-1	TOTAL CALORIMETER	NICKEL SLUG	.12 IN.	FLUSH, M-31 PANEL	HEAT SHIELD
C77-5	↓	↓	.12 IN.	FLUSH, M-31 PANEL	↓
C76-3	↓	↓	.12 IN.	PEDESTAL, X-258 PANEL	HEAT SHIELD, CALORIMETER FLANGE UNDER PANEL
C78-8	↓	COPPER SLUG	.60 IN.	FLUSH	FLAME SHIELD
C79-2	RADIATION CALORIMETER	↓	.27 IN.	PEDESTAL	HEAT SHIELD — 150° VIEW ANGLE
C64-4	RADIATION CALORIMETER	↓	.27 IN.	PEDESTAL	HEAT SHIELD — 150° VIEW ANGLE
C10-2	GAS TEMPERATURE PROBE	CHROMEL-ALUMEL THERMOCOUPLE	——	FLUSH — PROTECTIVE BRACKET & PROTECTIVE RING	HEAT SHIELD
C10-4	↓	↓	==	↓	↓
C10-7	↓	↓	==	↓	↓
C65-3	↓	↓	——	PEDESTAL, NO BRACKET	↓
C93-7	↓	↓	——	PEDESTAL, NO BRACKET	↓
C67-7	↓	PLATINUM-PLATINUM 10% RHODIUM	——	FLUSH, NO BRACKET	FLAME SHIELD

FIGURE I. SATURN I VEHICLE CONFIGURATIONS
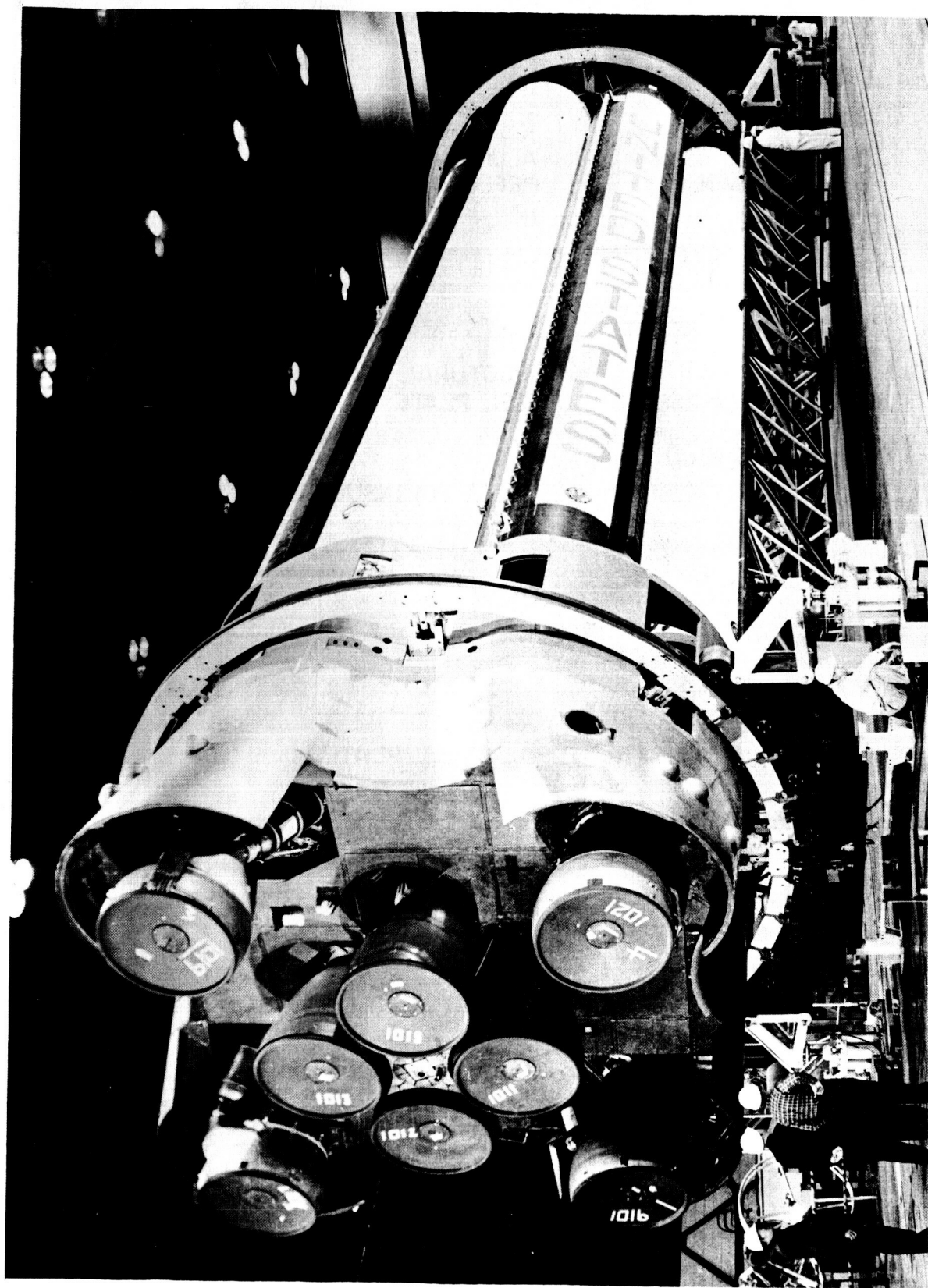
FIGURE 2. AFT VIEW OF S-I STAGE OF SATURN I BLOCK I VEHICLE

29

THERMOLAG

ALUMINUM
REFLECTIVE TAPE

.060"

.25"

.040"

ASBESTOS
(X-258)

STRUCTURAL
STEEL PLATE

a. HEAT SHIELD

CT-301 INSULATION

1.30"

.125"

STRUCTURAL STEEL PLATE

b. FLAME SHIELD

M-31 INSULATION

.06"

.25"

STEEL MESH

STRUCTURAL STEEL
PLATE

.04"

c. BLOCK II TEST PANEL
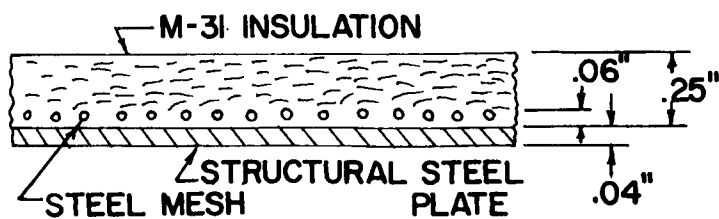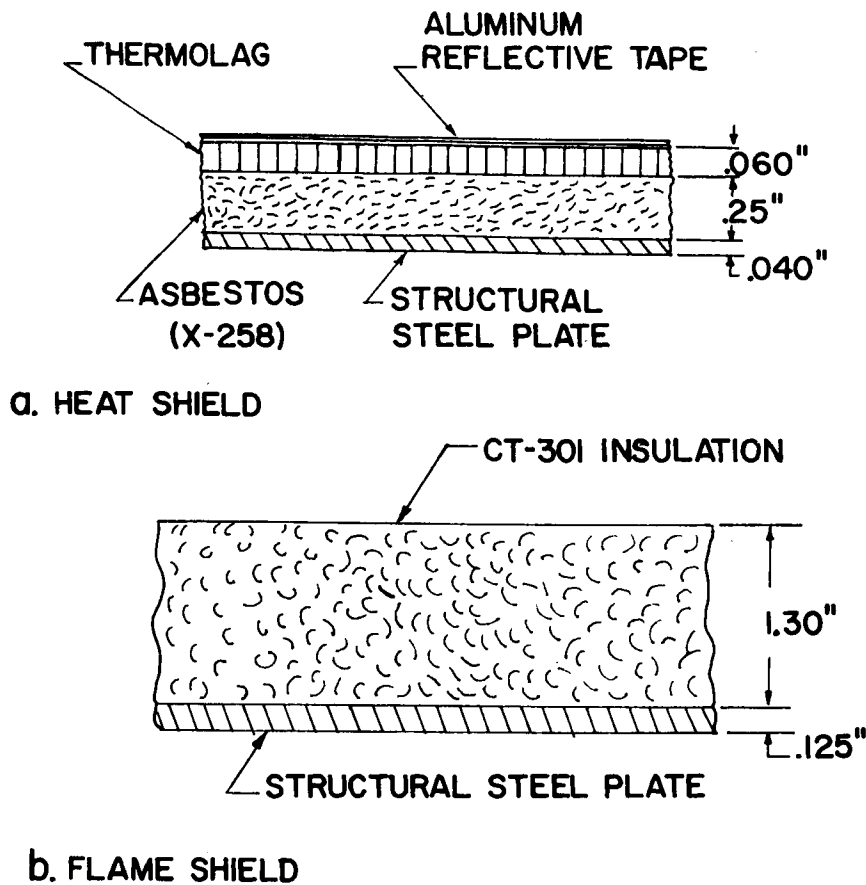
FIGURE 3. CROSS SECTION OF BASE HEAT PROTECTION
FOR S-I STAGE OF SATURN I BLOCK I VEHICLE

	IECO	OECO (SEC)
SA-1	110	116
SA-2	111	117
SA-3	142	149
SA-4	113.5	121
SA-4	100.6 (# 5 ENGINE)	

SA-1
SA-2
SA-3
SA-4

ALTITUDE, FT x 10³

ALTITUDE, KM

TIME, SECONDS
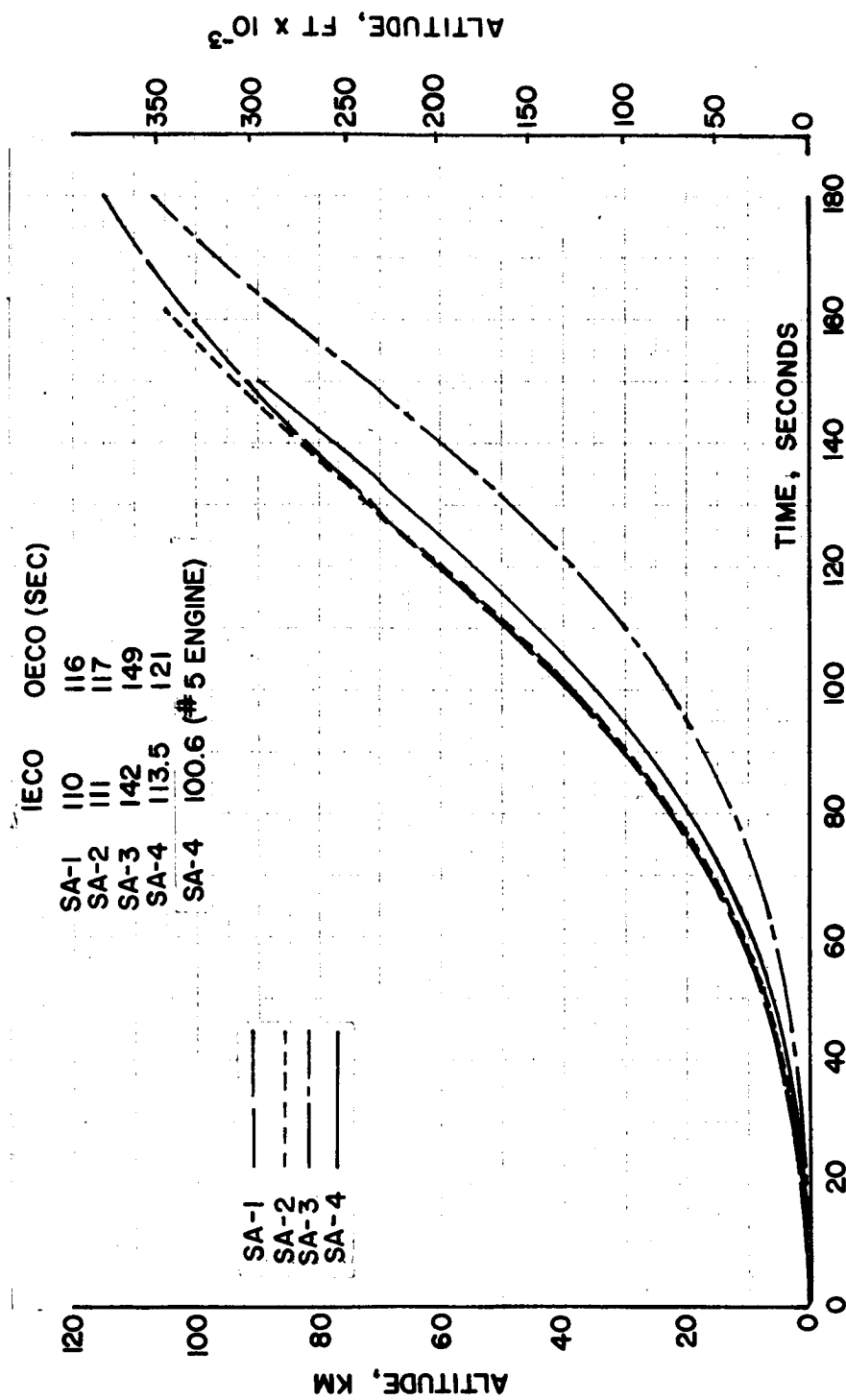
FIGURE 4a. COMPARISON OF FLIGHT TRAJECTORIES FOR THE SATURN I BLOCK I VEHICLES
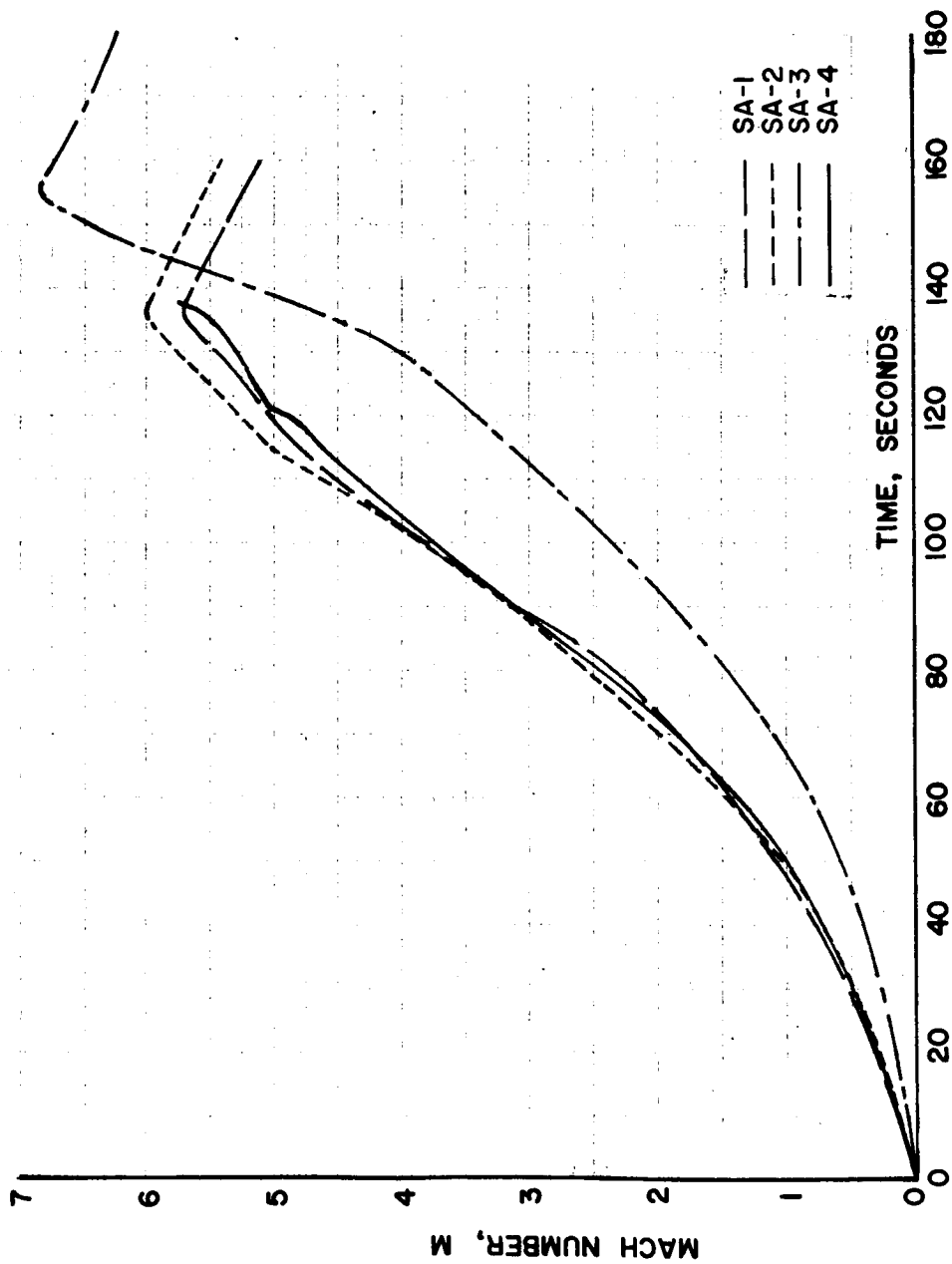
FIGURE 4b. COMPARISON OF FLIGHT TRAJECTORIES FOR THE
SATURN I BLOCK I VEHICLES

32

VELOCITY, FT/SEC x 10⁻³
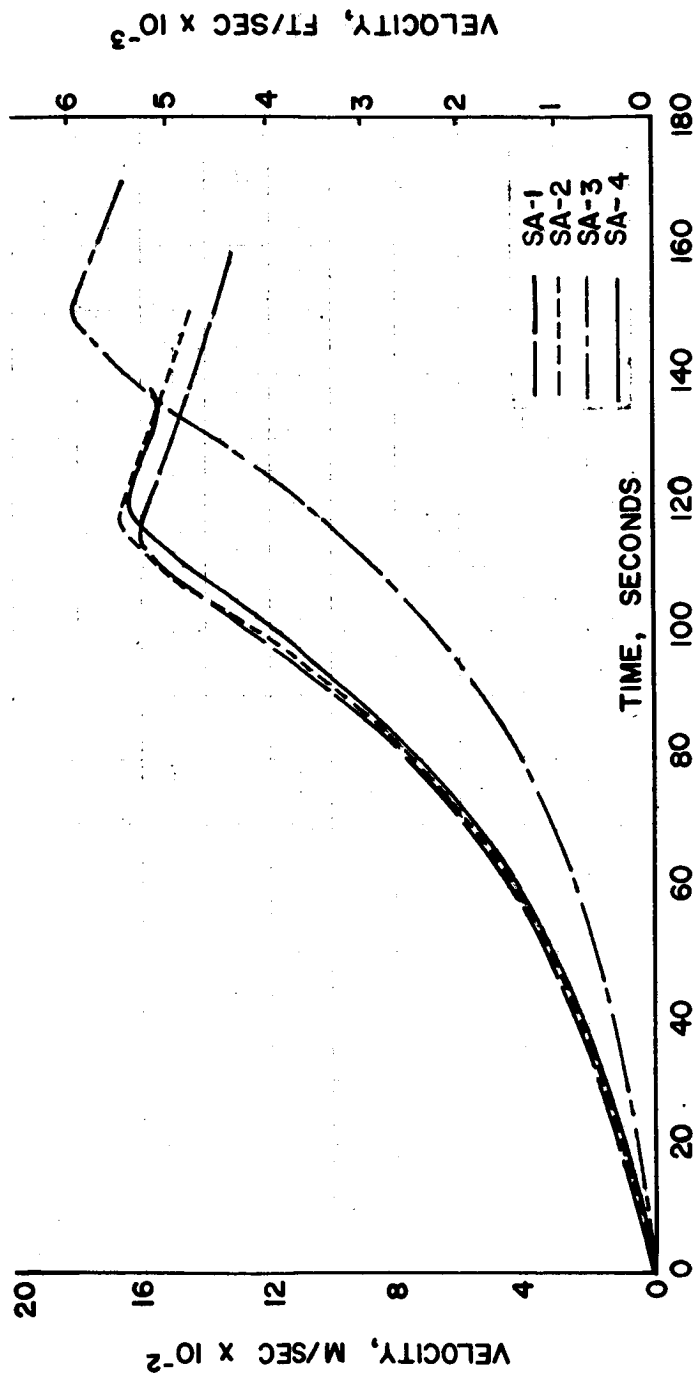
FIGURE 4c. COMPARISON OF FLIGHT TRAJECTORIES FOR THE
SATURN I BLOCK I VEHICLES

TIME, SECONDS

VELOCITY, M/SEC x 10⁻²

SA-1
SA-2
SA-3
SA-4

33
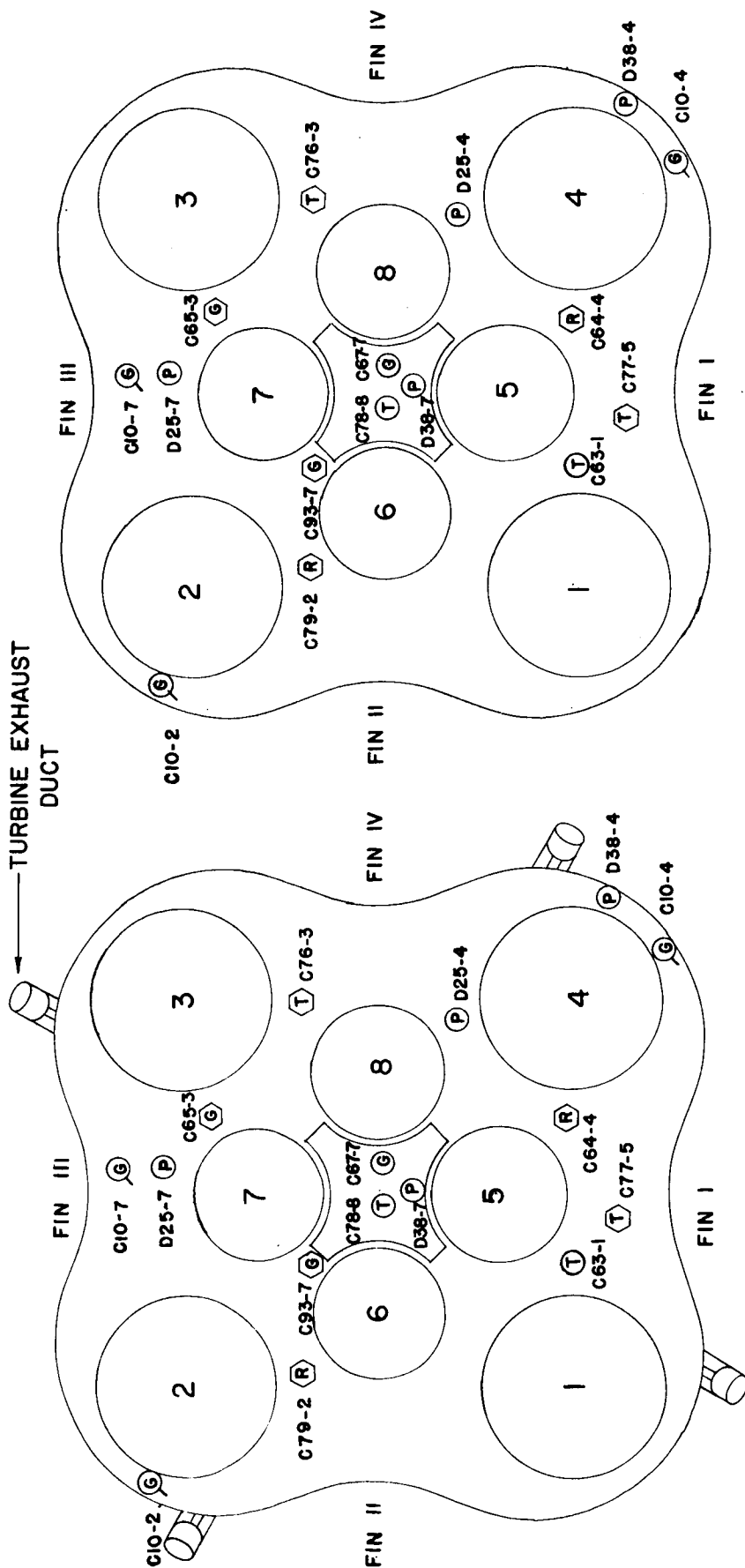
SA-2 FLIGHT

SA-1 FLIGHT

TURBINE EXHAUST DUCT

R - RADIATION CALORIMETER

T - TOTAL CALORIMETER

P - PRESSURE ORIFICE

G - GAS TEMPERATURE PROBE

◯ - FLUSH MOUNTED (SEE FIGURE II)

⬡ - MOUNTED ON 9-INCH PEDESTAL (SEE FIGURE IO)

FLAGGED SYMBOL INDICATES PRO-

TECTIVE BRACKET USED (SEE

FIGURE 21)
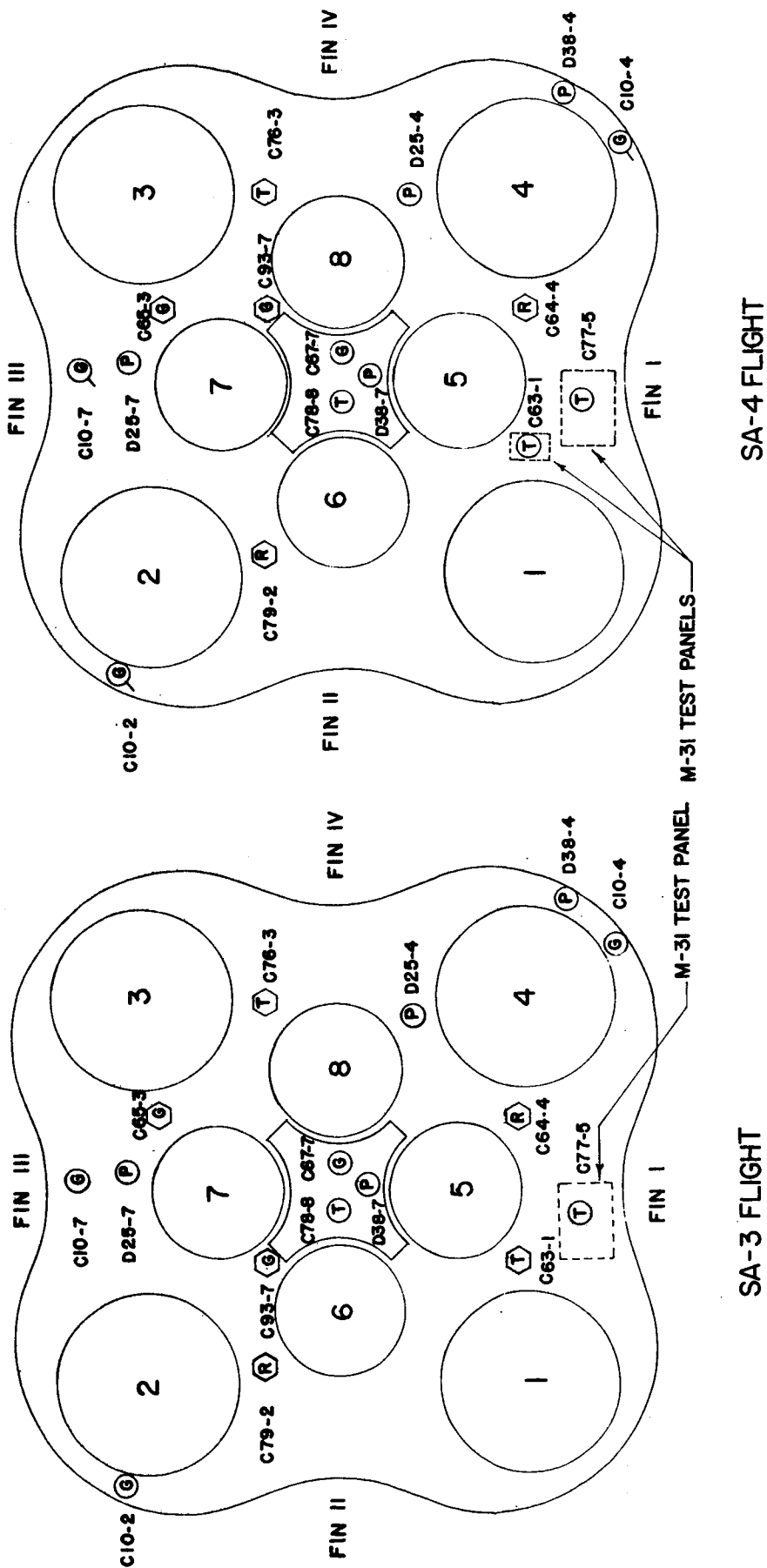
FIGURE 5. LOCATION OF INSTRUMENTATION ON THE BASE OF SATURN I
BLOCK I VEHICLES

CLAMP-WIRE

THERMOCOUPLE JUNCTION

ATTACHMENT POINTS TO HEAT SHIELD OR PEDESTAL

ASBESTOS GASKET

REFRASIL PACKING

HIGH-TEMP CEMENT

REFRASIL FIBERGLASS

3.500

2.500

.090 TYP.

.625

.060
.031
.120

.120

.050

3.500

2.500

SURFACE PLATINUM BLACKENED FOR ABSORPTIVITY

COPPER OR NICKEL (GRADE "A")

THERMOCOUPLE JUNCTION (ALUMEL-CHROMEL)

CERAMIC (ALUMINA)

COPPER OR NICKEL (GRADE "A")
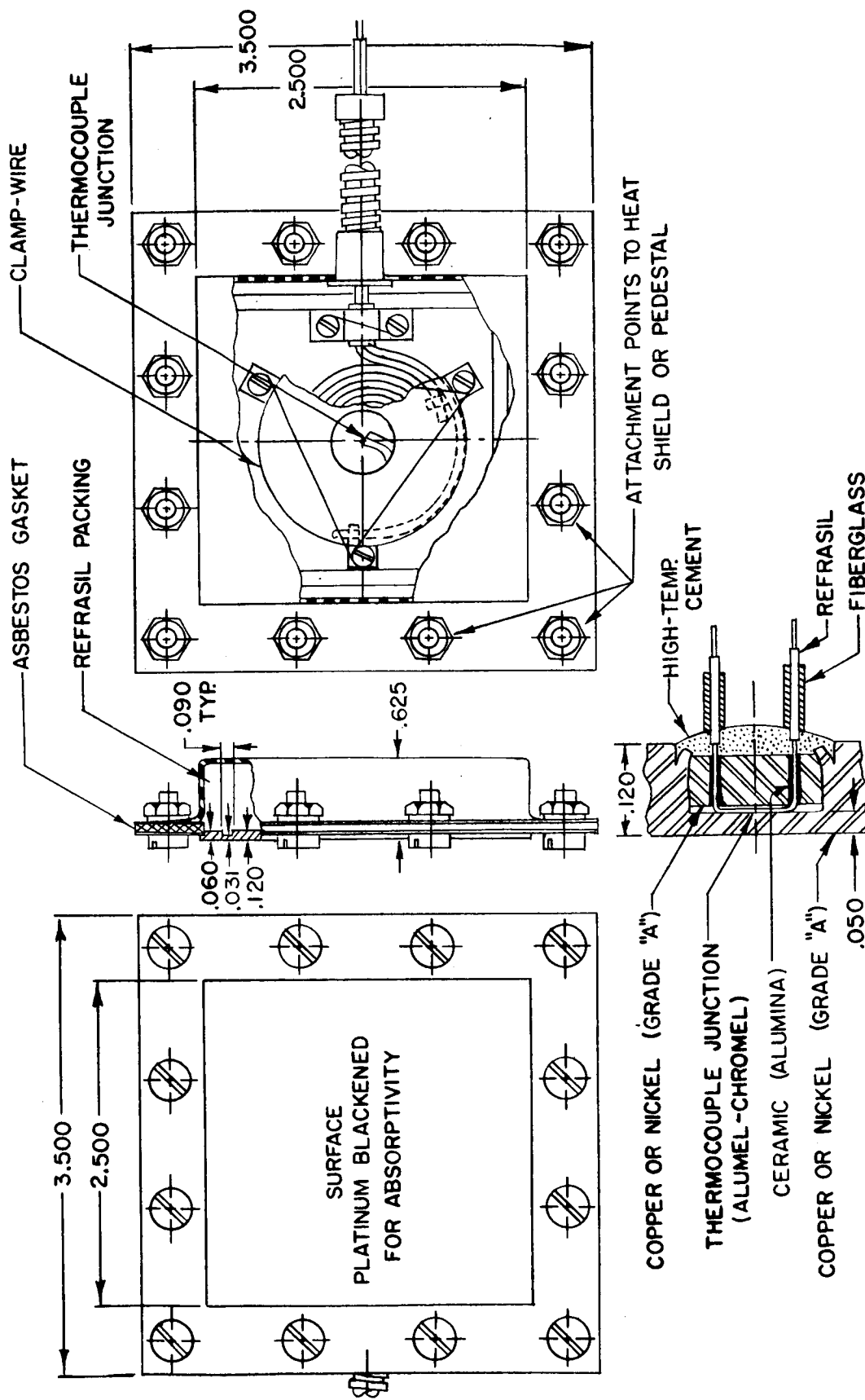
DIMENSIONS IN INCHES

FIGURE 6. TOTAL CALORIMETER USED ON HEAT SHIELD OF SATURN I BLOCK I VEHICLES
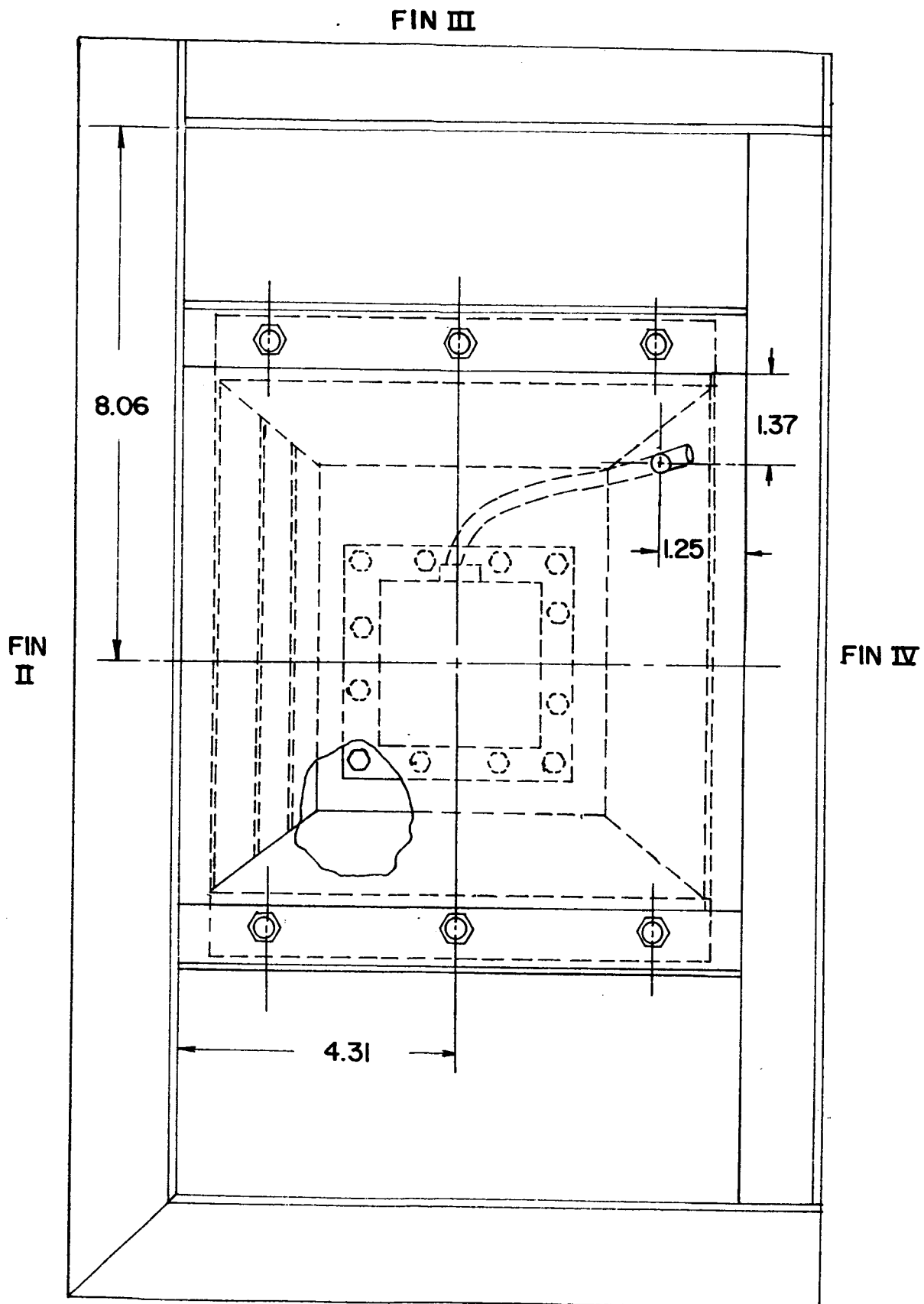
FIGURE 7. INSTALLATION DRAWING OF
SATURN I

.04
.25
.06
THERMOLAG
X258
.25
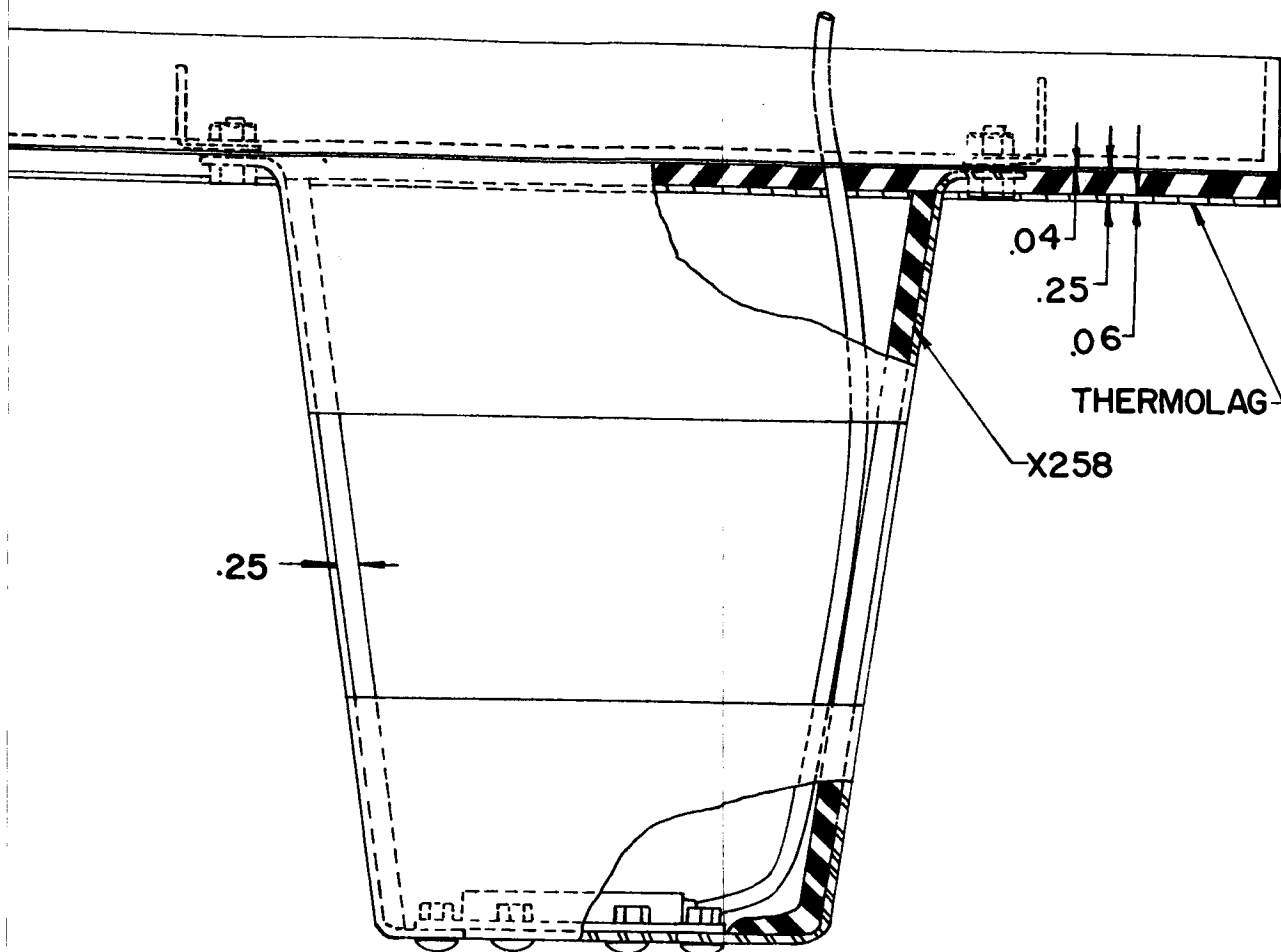
REFER TO DRAWING # 10410002-C (DETAIL GE-GE & VIEW CZ-CZ)

NOTE: CALORIMETER C63-I MOUNTED AS SHOWN FOR SA-3 FLIGHT

.390 CABLE HOLE THRU HEAT SHIELD.

SCALE 1/2 — ALL DIMENSIONS IN INCHES

TOTAL CALORIMETER C76-3 FOR BLOCK I VEHICLES

2#

FIN III

2.00

FIN II

3.50

1.375

0.50

FIN I
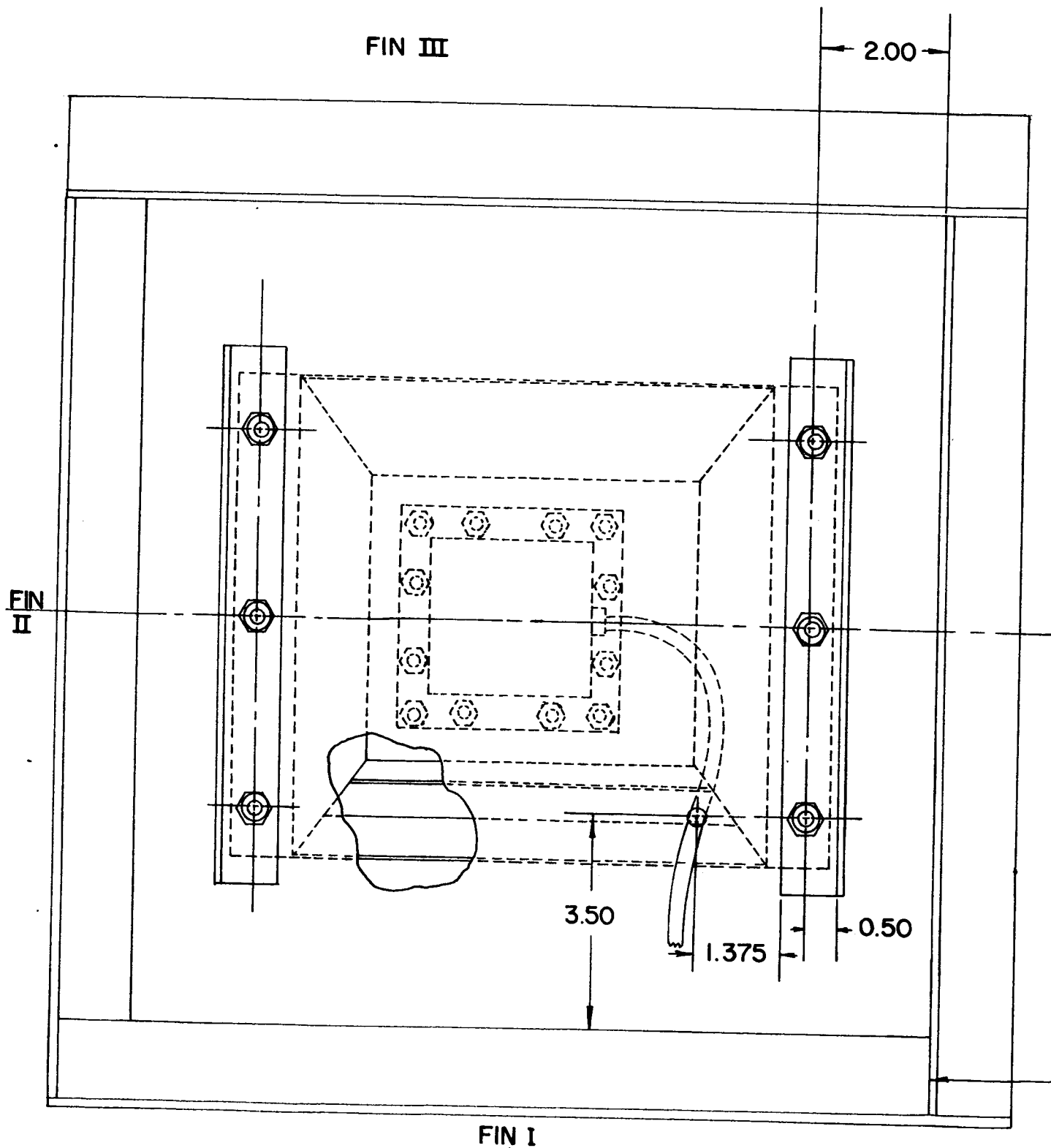
FIGURE 8. INSTALLATION DRAWING OF TOTA
SATURN SA-I AND

.04

.25

.06

THERMOLAG

X258

.25

FIN IV
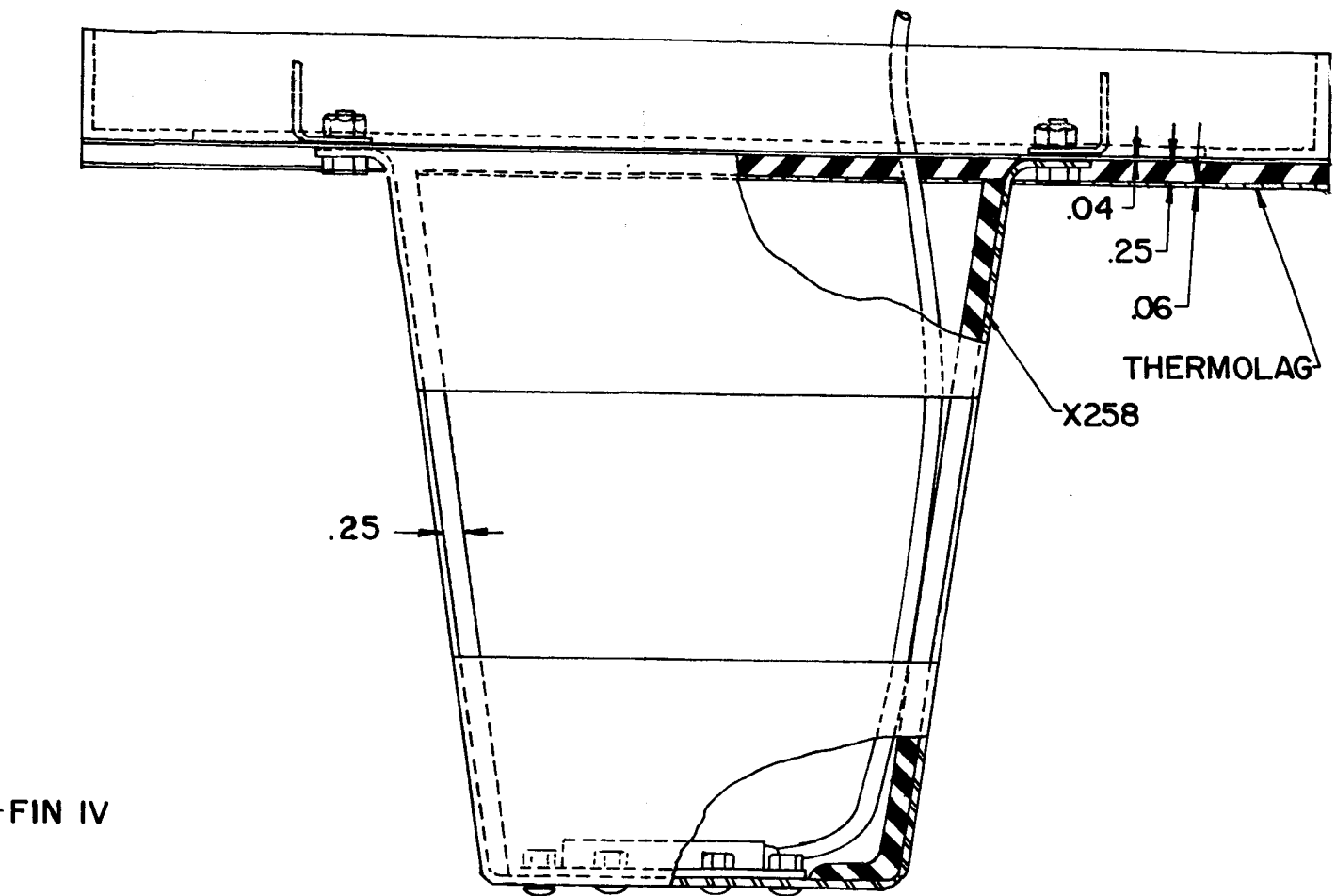
REFER TO DRAWING # 10410002-C (DETAIL GF & VIEW CZ-CZ)

SCALE 1/2 – ALL DIMENSIONS IN INCHES

CENTERLINE OF MISSILE

L CALORIMETER C77-5 FOR SA-2 FLIGHTS

2#

FIN III

FIN II

FIN I
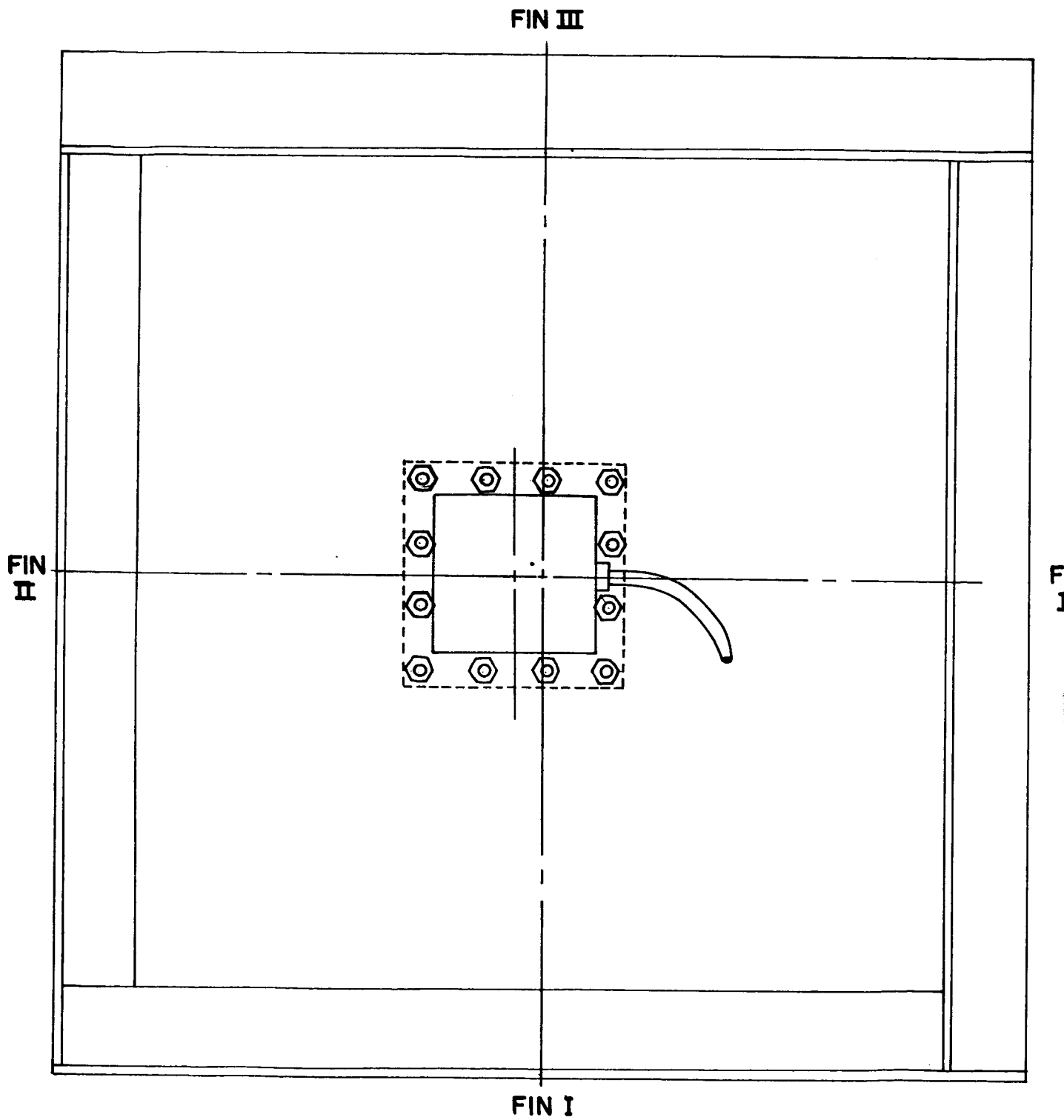
FIGURE 9. INSTALLATION DRAWING OF TOTA
SATURN SA-3

NOTE: CALORIMETER C63-1 INSTALLED AS SHOWN FOR SA-4 FLIGHT

SECTION A

SPACER PLATE .125 THICK

.25   .50

11/64
DIA

3.50

2.50

.25   3.50

M-31

.25   .103
.040

.65
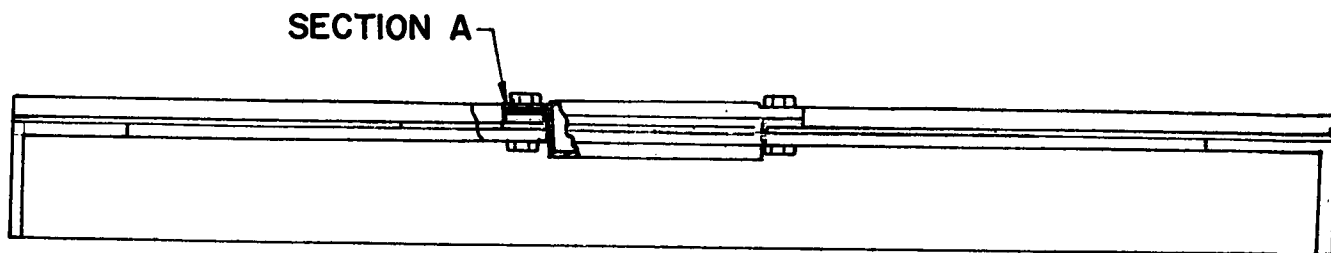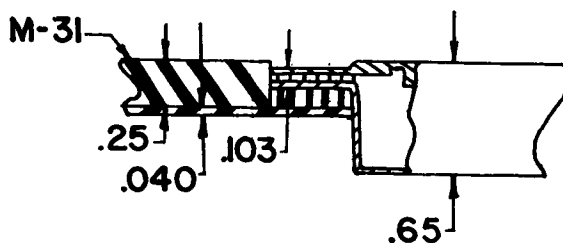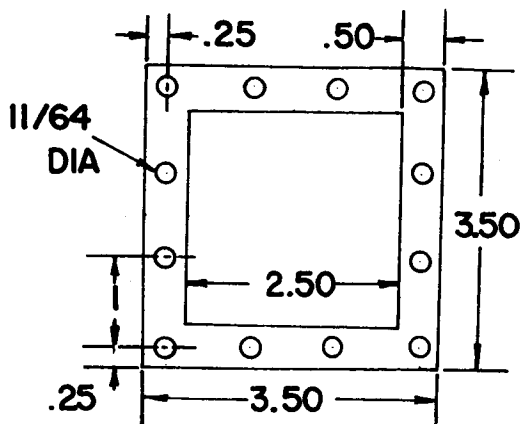
SECTION A

ALL DIMENSIONS IN INCHES
M-31 COATING ATTACHED TO BACKUP PLATE WITH WIRE LATHE

L CALORIMETER C77-5 FOR
5 AND SA-4 FLIGHTS

2#
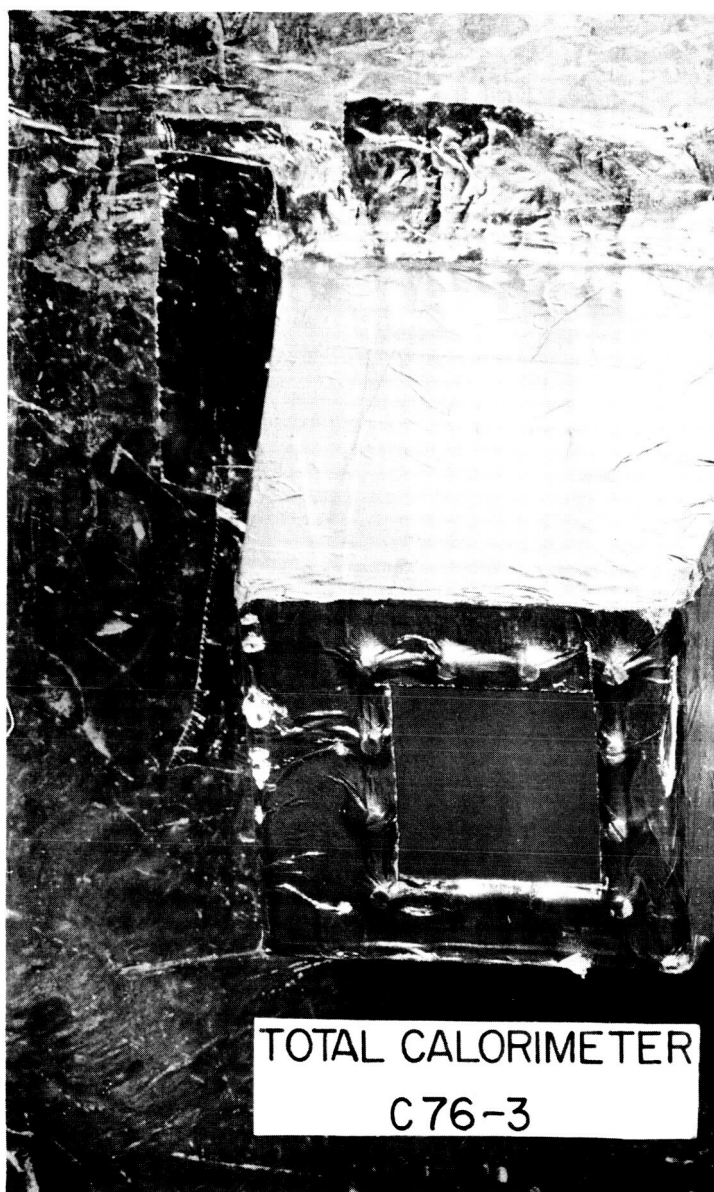
TOTAL CALORIMETER
C 76-3

SA-4 FLIGHT-ALUMINUM TAPE

FIGURE 10. VARIATION IN PED

ON PEDESTAL

SA-3 FLIG

ESTAL CONDITIONS FOR BLOCK

2#

PEDESTAL MOUNTED
TOTAL CALORIMETER
BLOCK I HEAT SHIELD

;HT—NO TAPE ON PEDESTAL

< I TOTAL CALORIMETERS

3#

TOTAL CALORIMETER C63-1

M-31 PANEL

SA-4 FLIGHT

TOTAL CALORIMETER C77-5

M-31 PANEL
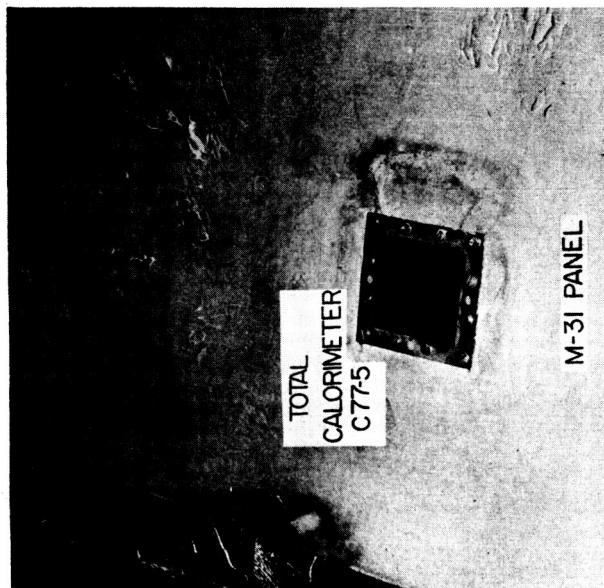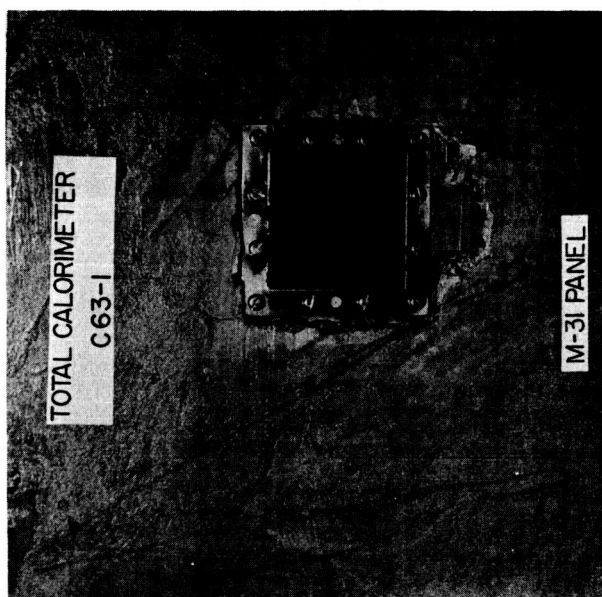
SA-3 FLIGHT

FIGURE 11. VARIATION IN FLUSH MOUNTING FOR BLOCK I TOTAL CALORIMETERS

45
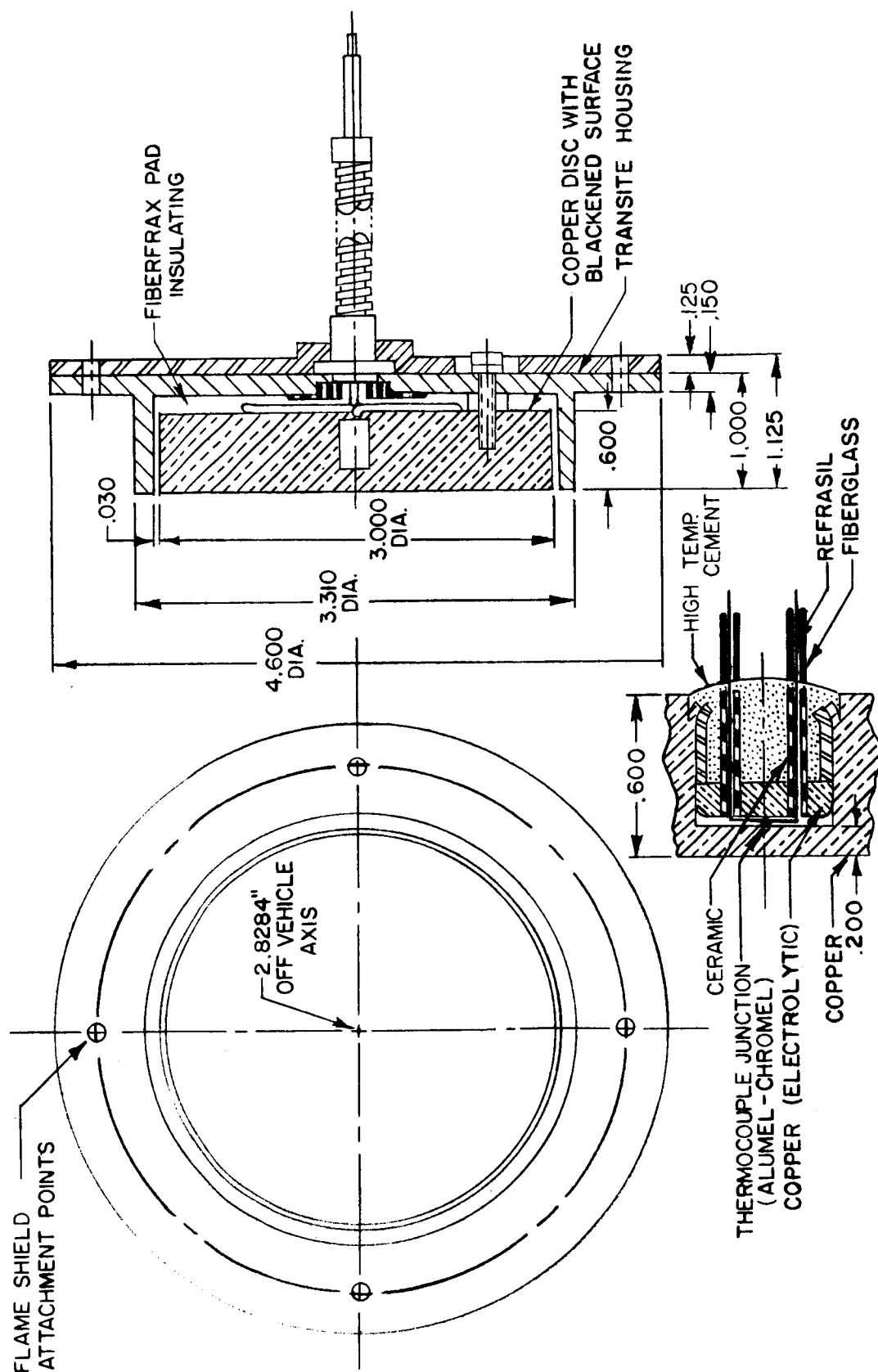
FIGURE 12. TOTAL CALORIMETER USED ON FLAME SHIELD OF SATURN I BLOCK I VEHICLES

FIBERFRAX PAD INSULATING

COPPER DISC WITH BLACKENED SURFACE

TRANSITE HOUSING

.125
.150
.030
1.000
1.125
.600
3.000 DIA.
3.310 DIA.
4.600 DIA.

HIGH TEMP. CEMENT

REFRASIL FIBERGLASS

.600

CERAMIC

THERMOCOUPLE JUNCTION (ALUMEL-CHROMEL)

COPPER (ELECTROLYTIC)

COPPER

.200

2.8284" OFF VEHICLE AXIS

FLAME SHIELD ATTACHMENT POINTS

DIMENSIONS. IN INCHES

46

FIN II

HALF SCALE

FIN
I

3.0   4.6

12

2

45°

2

12

FIN IV

FIN III

FIGURE 13.   INSTALLATION   DRAWING   OF   TOTA

SATURN I BLOCK

FULL SCALE

.125

1.3

RANSITE HOUSING

3

.6

CT-301
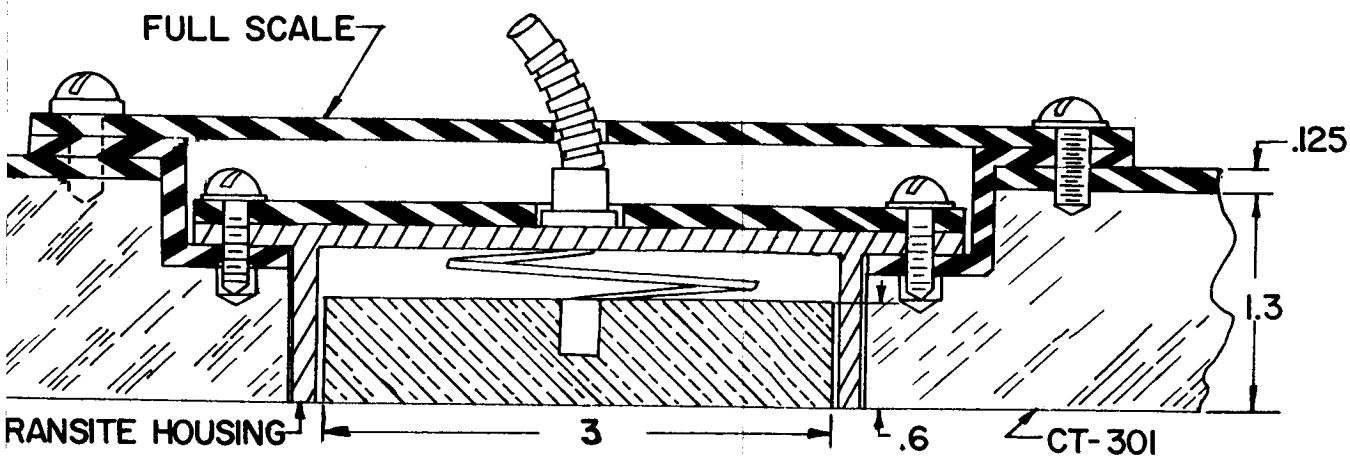
REFER TO DRAWING 10410002-C (VIEW HC-HC - SECTION HK-HK)

ALL DIMENSIONS IN INCHES

L CALORIMETER C78-8 FOR

I VEHICLES

2#

STATIC PRESSURE ORIFICE D38-7

GAS TEMPERATURE PROBE C67-7

TOTAL CALORIMETER C78-8
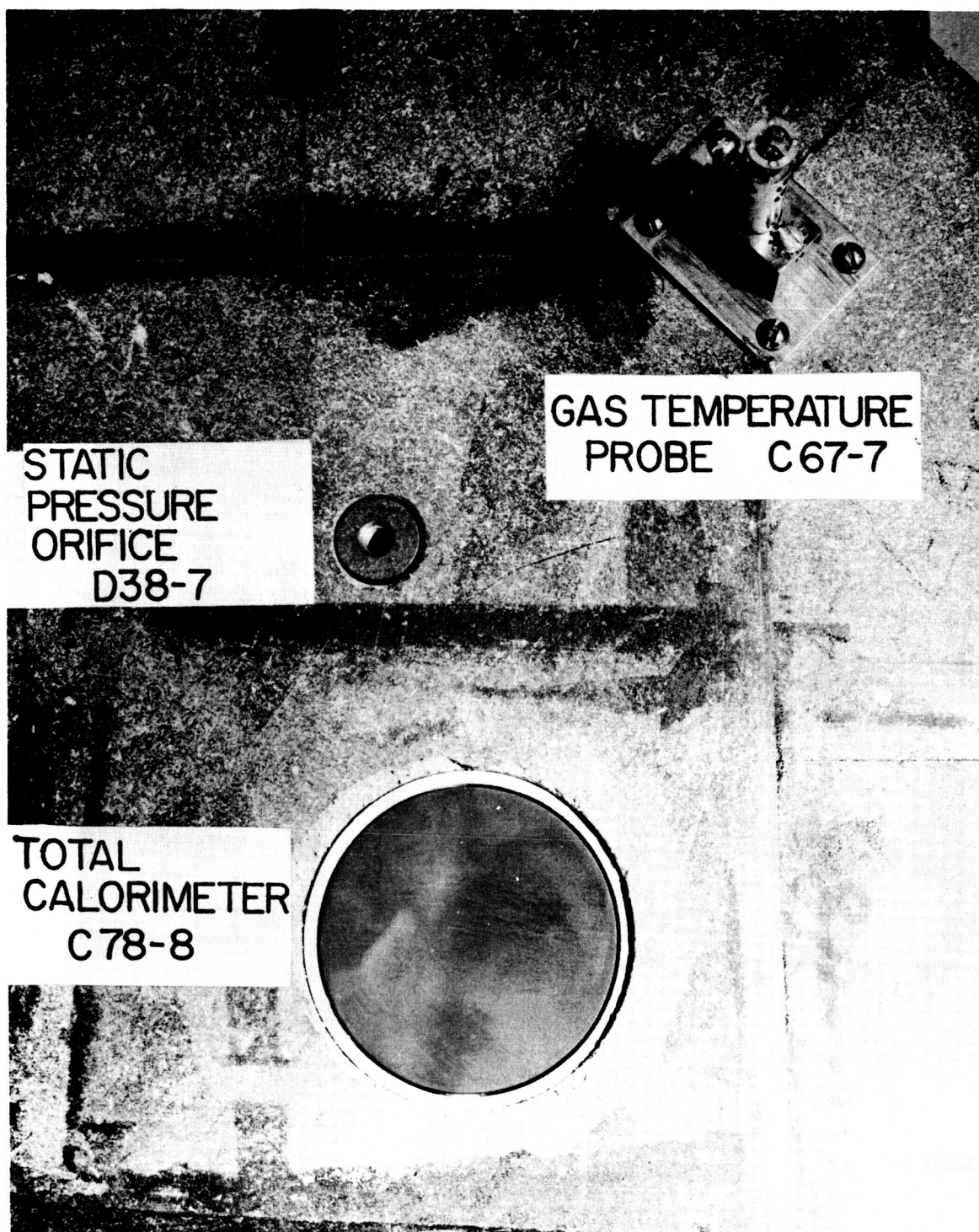
SA-3 FLIGHT

FIGURE 14.   FLAME SHIELD INSTRUMENTATION FOR THE BLOCK I VEHICLES

.312" DIA X .0394" THICK SAPPHIRE WINDOW

·.187"DIA X .126" THICK COPPER SLUG - BLACKEN SURFACE WITH EBONAL "C"

WIRE THERMOCOUPLE "ALUMEL" AWG 30 SOLID - FIBERGLASS OVER FIBERGLASS INSULATION

WIRE THERMOCOUPLE "CHROMEL" AWG 30 SOLID - FIBERGLASS OVER FIBERGLASS INSULATION

.165
.015
.003

60°

.250 DIA
.188 DIA

WIRE "CHROMEL" AWG 20 STRANDED - FIBERGLASS OVER FIBERGLASS INSULATION

WIRE "ALUMEL" AWG 20 STRANDED - FIBERGLASS OVER FIBERGLASS INSULATION

NITROGEN PURGE LINE (FLOW TO BE 6.2 TO 8.5 SCFM)

FIGURE 15.· SA-I FLIGHT RADIA

4.000 DIA

TION CALORIMETER

2#

.312" DIA X .0394" THICK
SAPPHIRE WINDOW

.230" DIA X .140" THICK
COPPER SLUG — BLACKEN
SURFACE WITH "EBONAL"

WIRE THERMOCOUPLE
"ALUMEL" AWG 30 SOLID

WIRE "ALUMEL" AWG 20
STRANDED - FIBERGLASS OVER
FIBERGLASS INSULATION

.015

.020

.050

A

.320
DIA

.280
DIA

WIRE "CHROMEL" AWG 20
STRANDED - FIBERGLASS OVER
FIBERGLASS INSULATION

A

WIRE THERMOCOUPLE
"CHROMEL" AWG 30 SOLID

NITROGEN PURGE LINE
(FLOW TO BE 6.2 TO 8.5
SCFM)

NO. 2 - 56 NC - 2A X .12 LG
SET SCREW — BRAZE
IN PLACE

.062 DIA. X .030 CERAMIC

SE

FIGURE 16. SA-2 FLIGHT RADIA

4.000 DIA

COPPER SLUG

cTION A-A

ATION CALORIMETER

2#

.120"

B ←

.625" DIA. X .0394" THICK
SAPPHIRE WINDOW

CHROMEL ALUMEL
30 AWG WIRE

ALUMEL 20 AWG
SOLID WIRE

CHROMEL 20 AWG
SOLID WIRE

CHRYCOTE ASSY.

EXCEPT BOTTOM

NITROGEN PURGE

FLOW CONNECTION
TO BE 3.0 ± 0.3 SCFM AT AN
UPSTREAM ORIFICE PRESS. OF
750 PSIG

B ←

SLUG NOTE:

HALF HARD COPPER SLUG .187"DIA. X.270"THICK
SPIRALLY GROOVED GENERATED FROM THE CENTER
WITH APPROX. 42 GROOVES PER INCH

35°   .017   .010

.028"DIA. X .04"

SET SCREW
NO. 2-56 NC-2A

FIGURE 17.   SA-3 AND SA-4 R

1#

4.00" DIA.

.349"
DIA.

.187"
DIA.

60°
REF.

COPPER RING
ID .232" OD .301"

STAINLESS STEEL
TUBE .028"OD X .005 WALL X .06"

COPPER SLUG

X. 18 LG

section B-B

DIATION FLIGHT CALORIMETER

2 #

FIN 4

FIN 3

1.250

FIN 1

8.06

FIN 2

RE

SC
3

FIGURE 18.   INSTALLATION DRAWING OF RADIAT

FOR SATURN I

18

.04

.25

.06

THERMOLAG

X258

.25
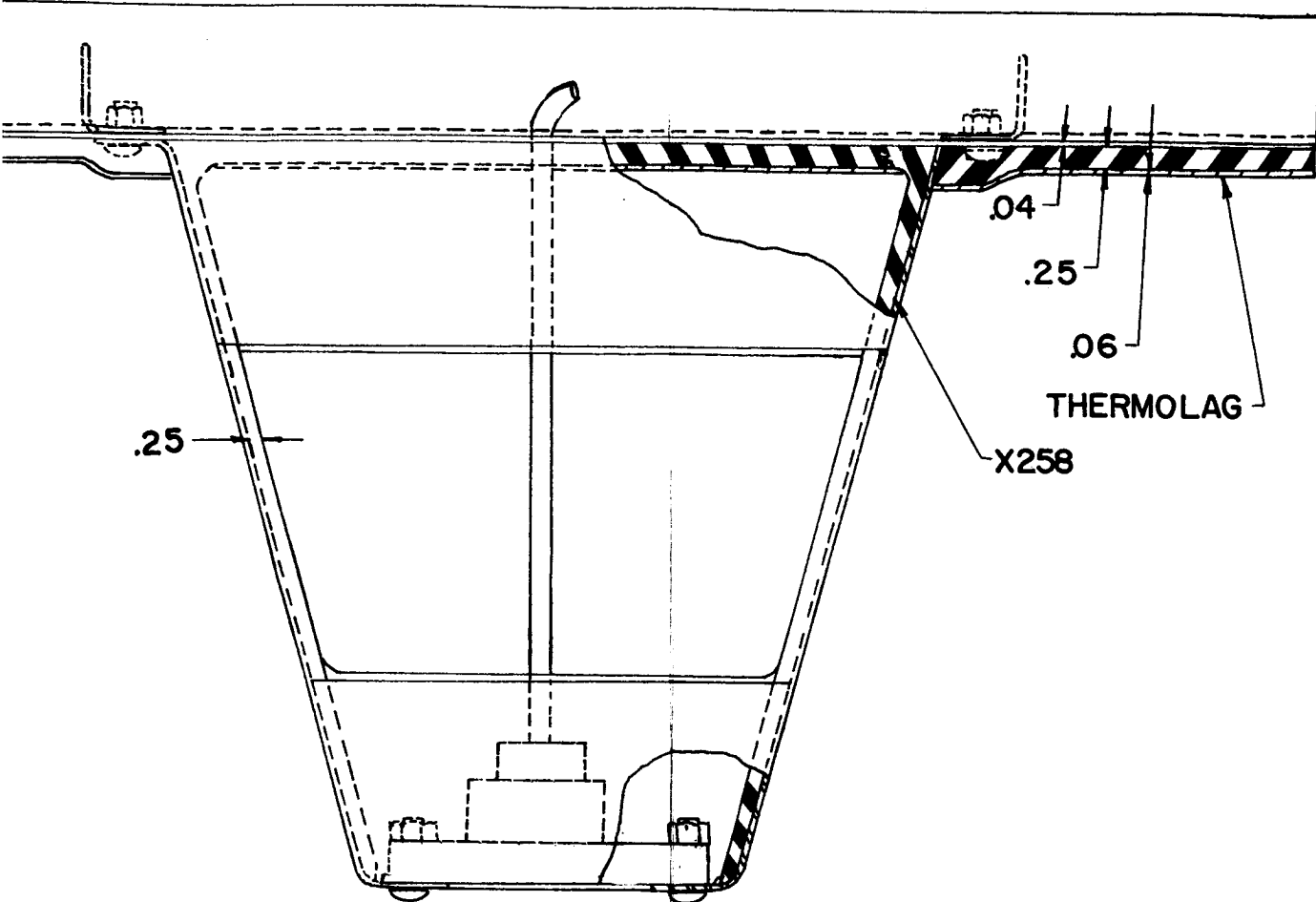
FER TO DRAWING #10410002-C (DETAIL GA – VIEW GU-GU)

CALE 1/2 — ALL DIMENSIONS IN INCHES
90 CABLE HOLE THRU HEAT SHIELD.

ION CALORIMETERS C64-4 & C79-2
BLOCK I VEHICLES

2#

GAS TEMPERATURE PROBE
C65-3

PEDESTAL MOUNTED
GAS TEMPERATURE PROBE
BLOCK I HEAT SHIELD

SA-3 FLIGHT

PEDESTAL MOUNTED
RADIATION CALORIMETER
BLOCK I HEAT SHIELD
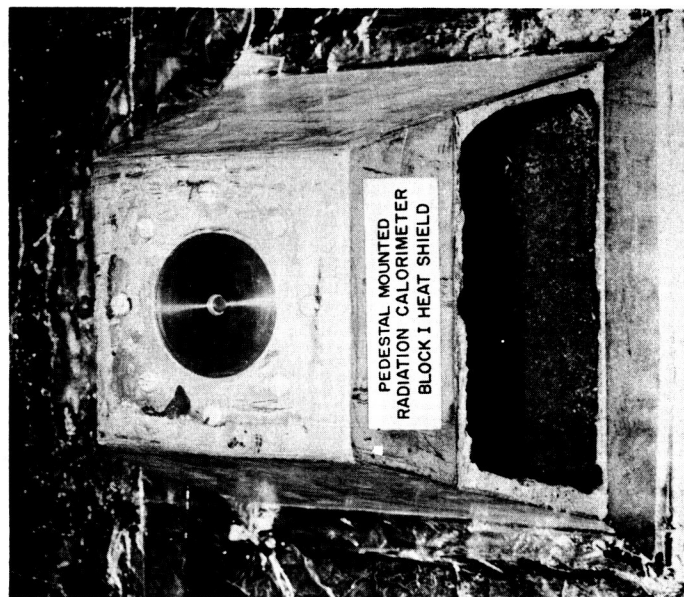
SA-3 FLIGHT

FIGURE 19. PEDESTAL MOUNTED BLOCK I RADIATION CALORIMETER AND GAS TEMPERATURE PROBE
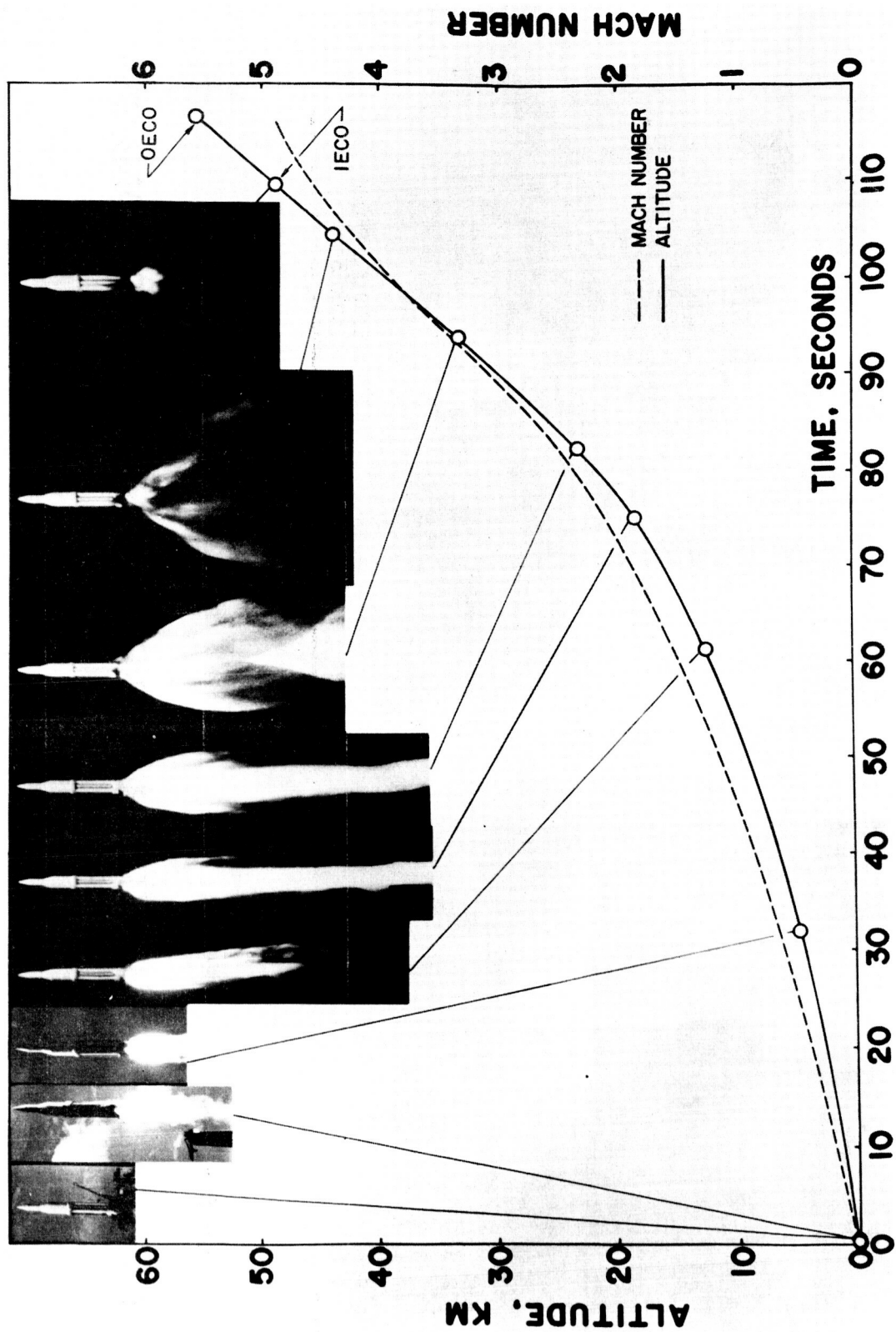
FIGURE 20. TYPICAL SATURN I PLUME EXPANSION WITH ALTITUDE

(SA-1 FLIGHT TRAJECTORY)

60

Dimensions and labels visible on figure:

1.250

1.250

.620

.250 RAD

.185 RAD

.250

PROTECTIVE BRACKET

INSTALLED ON ALL PROBES
EXCEPT FLAME SHIELD
PROBE

INNER
SHIELD

OUTER
SHIELD

2.13

1.32
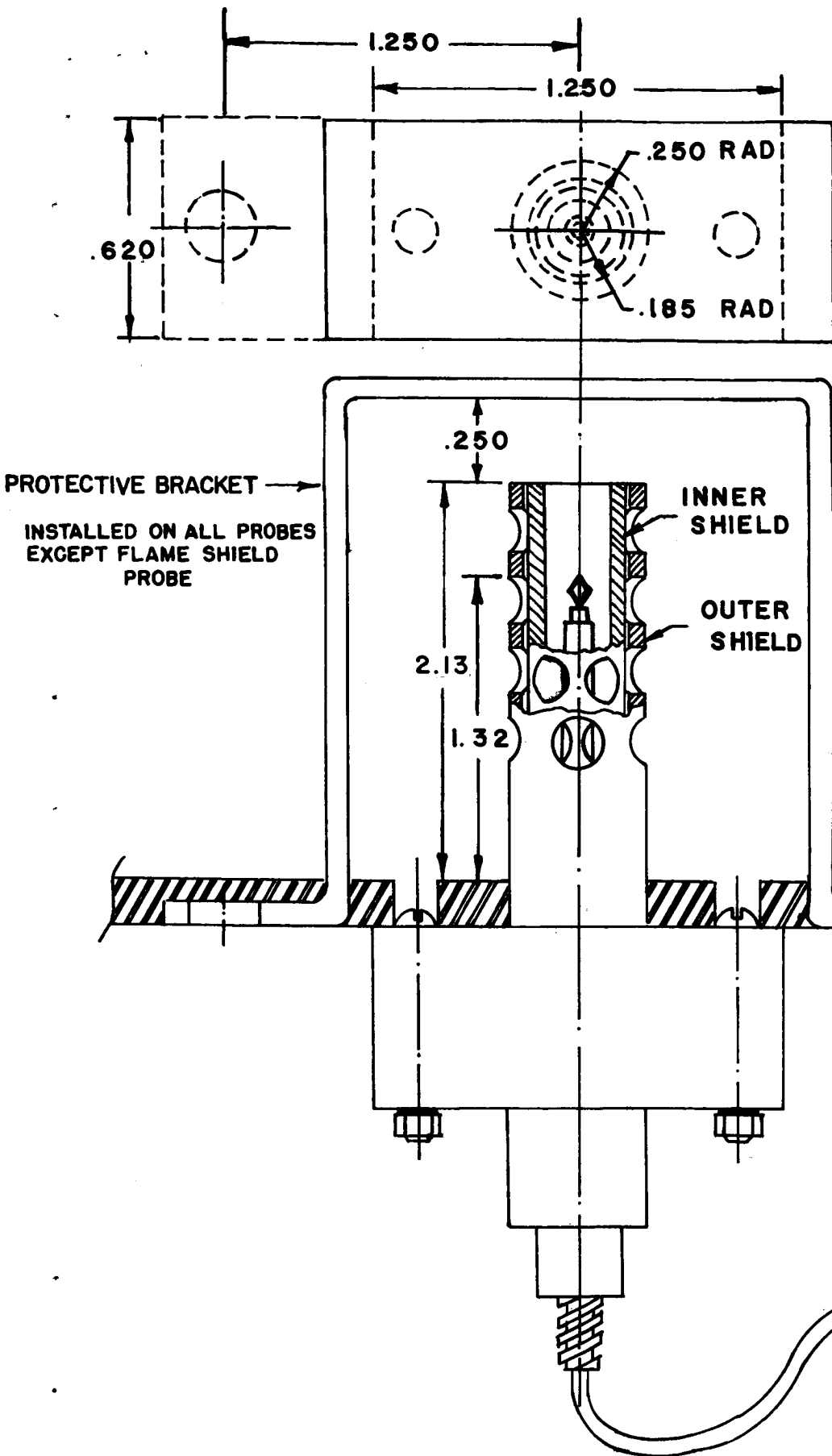
(A) DOUBLE SHIELD TYPE WITH F

SA-1   FLIGHT

FIGURE 21.   GAS TEMPERAT

1.250

.620

1.68

FLIGHT
DIRECTION
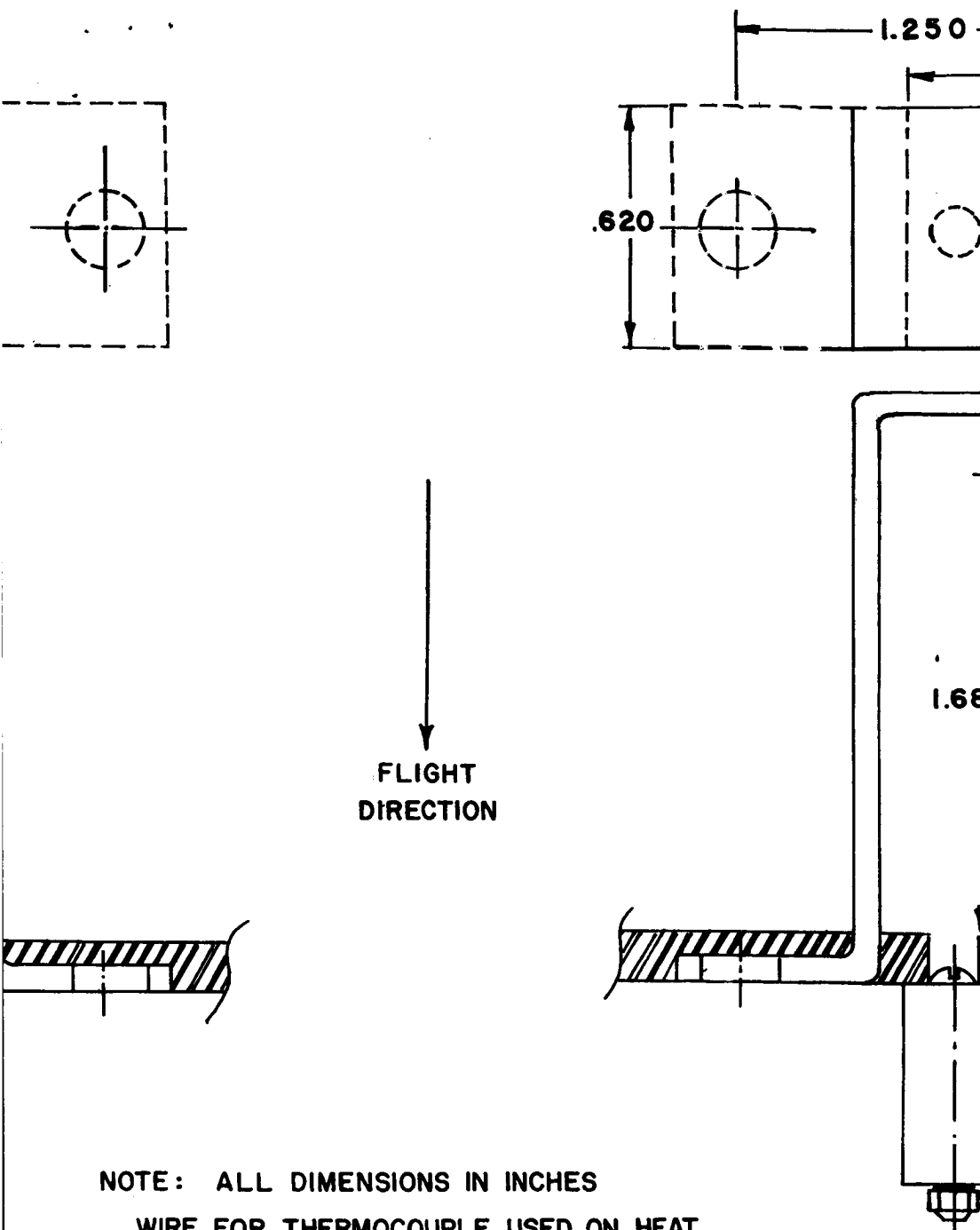
NOTE: ALL DIMENSIONS IN INCHES

WIRE FOR THERMOCOUPLE USED ON HEAT
SHIELD IS 28 GAUGE ALUMEL-CHROMEL

WIRE FOR THERMOCOUPLE USED ON FLAME
SHIELD IS 24 AWG PLATINUM-PLATINUM 10% RHODIUM

PROTECTIVE BRACKET   (B) UNSHIELDED PROTECT
                                             SA-2, SA-

TURE PROBES FOR SATURN I BLOCK I VEHICLES

1.250

.250 RAD

.185 RAD

GUARD RING .250

PROTECTIVE BRACKET

SUPPORT POST

INSTALLED ON FLUSH MOUNTED PROBES ONLY ON HEAT SHIELD

7

1.50
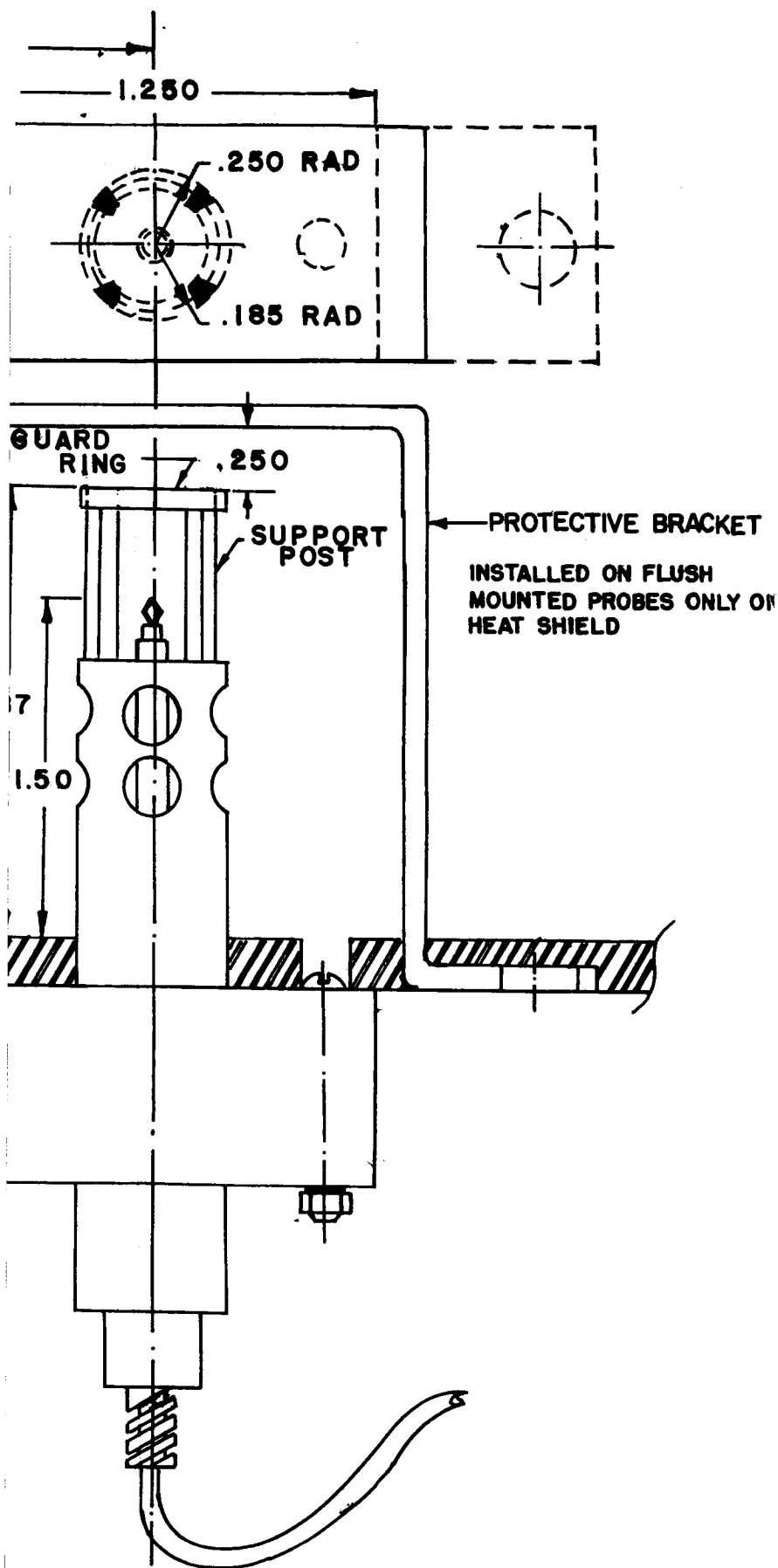
IVE RING TYPE WITH PROTECTIVE BRACKET
3 AND SA-4 FLIGHTS

S

3 FT

GAS TEMPERATURE
PROBE CIO-7

SA-4 FLIGHT –PROTECTIVE BRACKET INSTALLED

GAS TEMPERATURE
PROBE CIO-4

FLUSH MOUNTED
GAS TEMPERATURE PROBE
BLOCK I HEAT SHIELD

SA-3 FLIGHT – NO PROTECTIVE BRACKET

FIGURE 22. VARIATION IN FLUSH MOUNTING OF BLOCK I GAS TEMPERATURE PROBES

63

INFLIGHT CALIBRATION METHOD
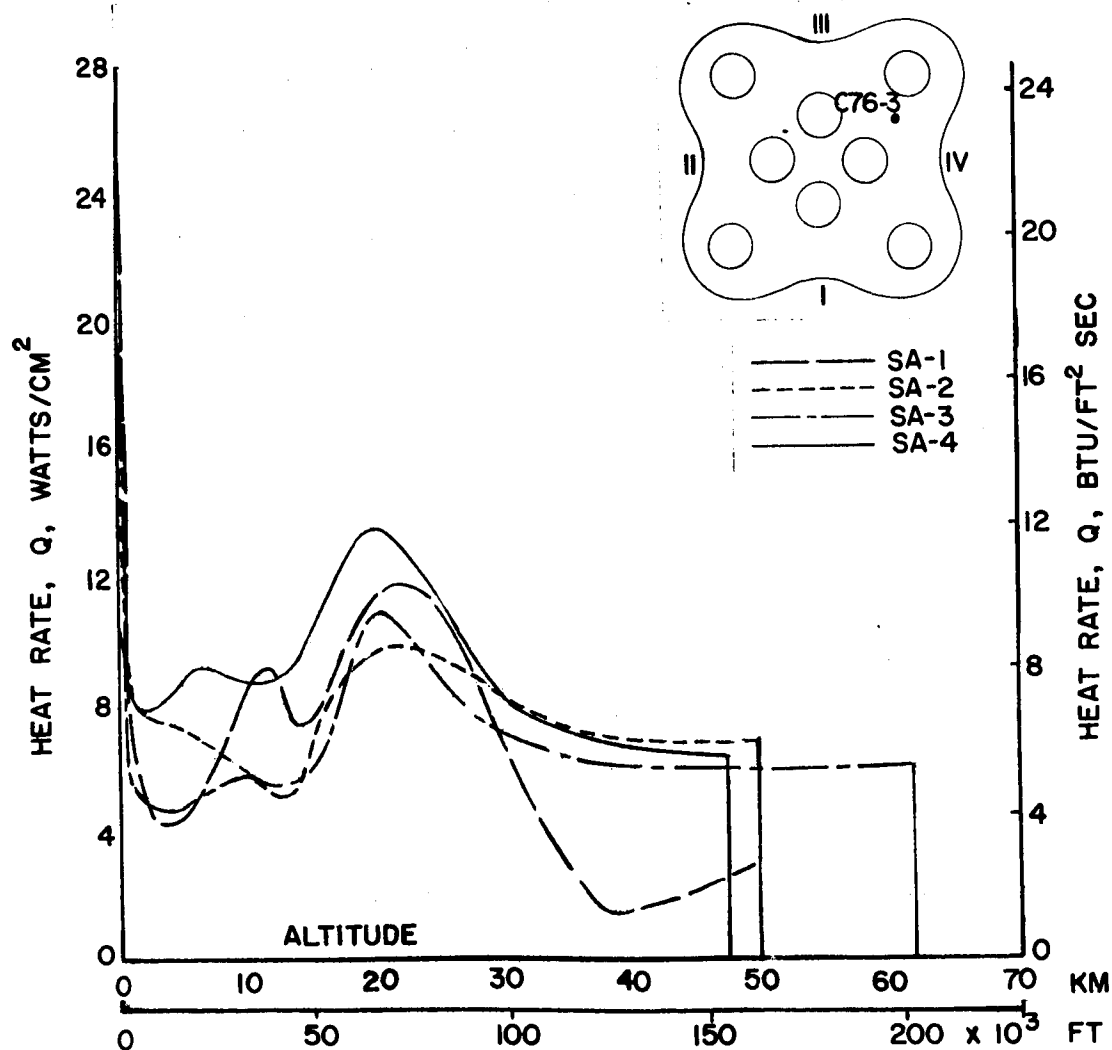
FIGURE 23a. COMPARISON OF TOTAL HEATING RATES ON
BASE OF SATURN I BLOCK I VEHICLES
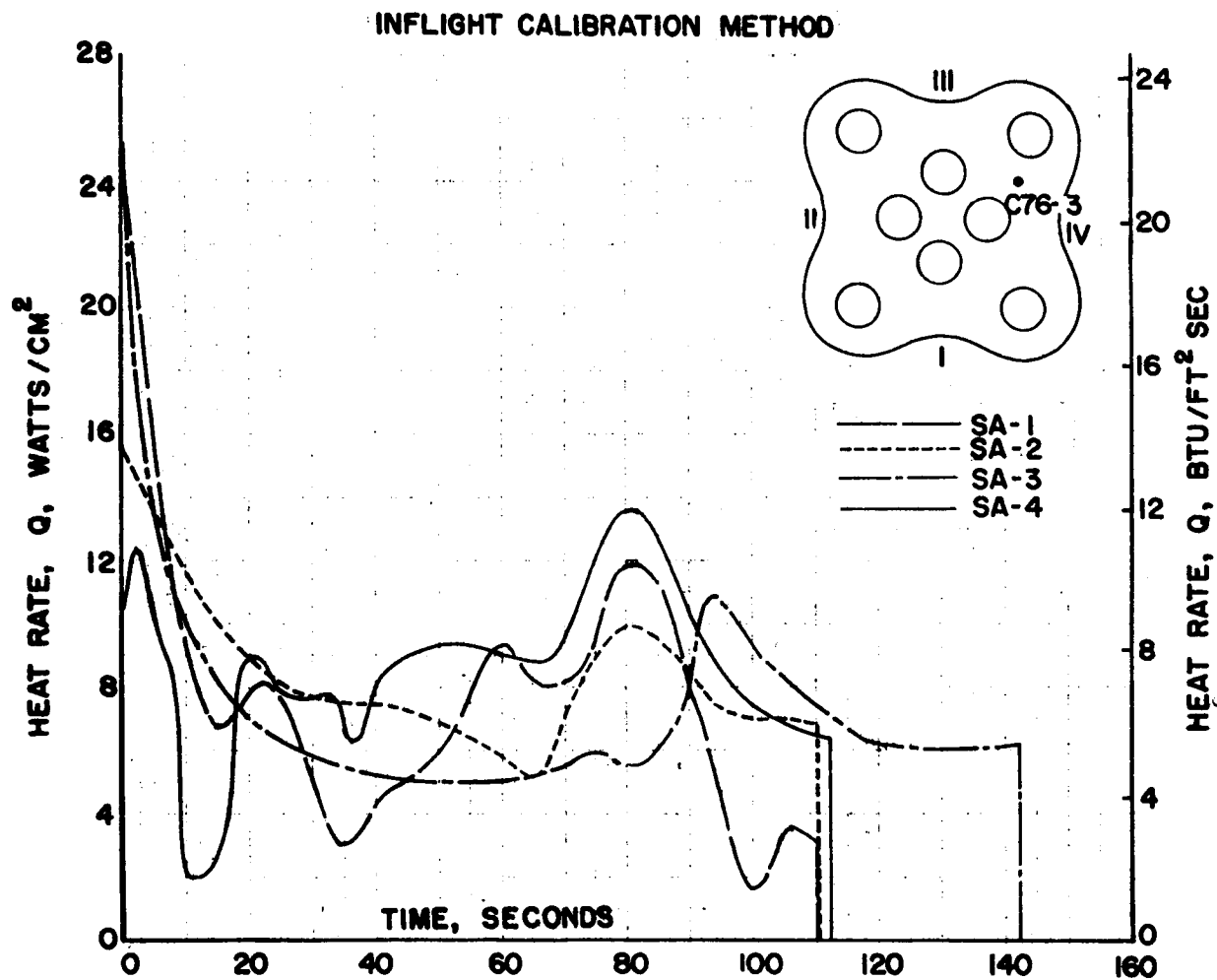
FIGURE 23b. COMPARISON OF TOTAL HEATING RATES ON
BASE OF SATURN I BLOCK I VEHICLES
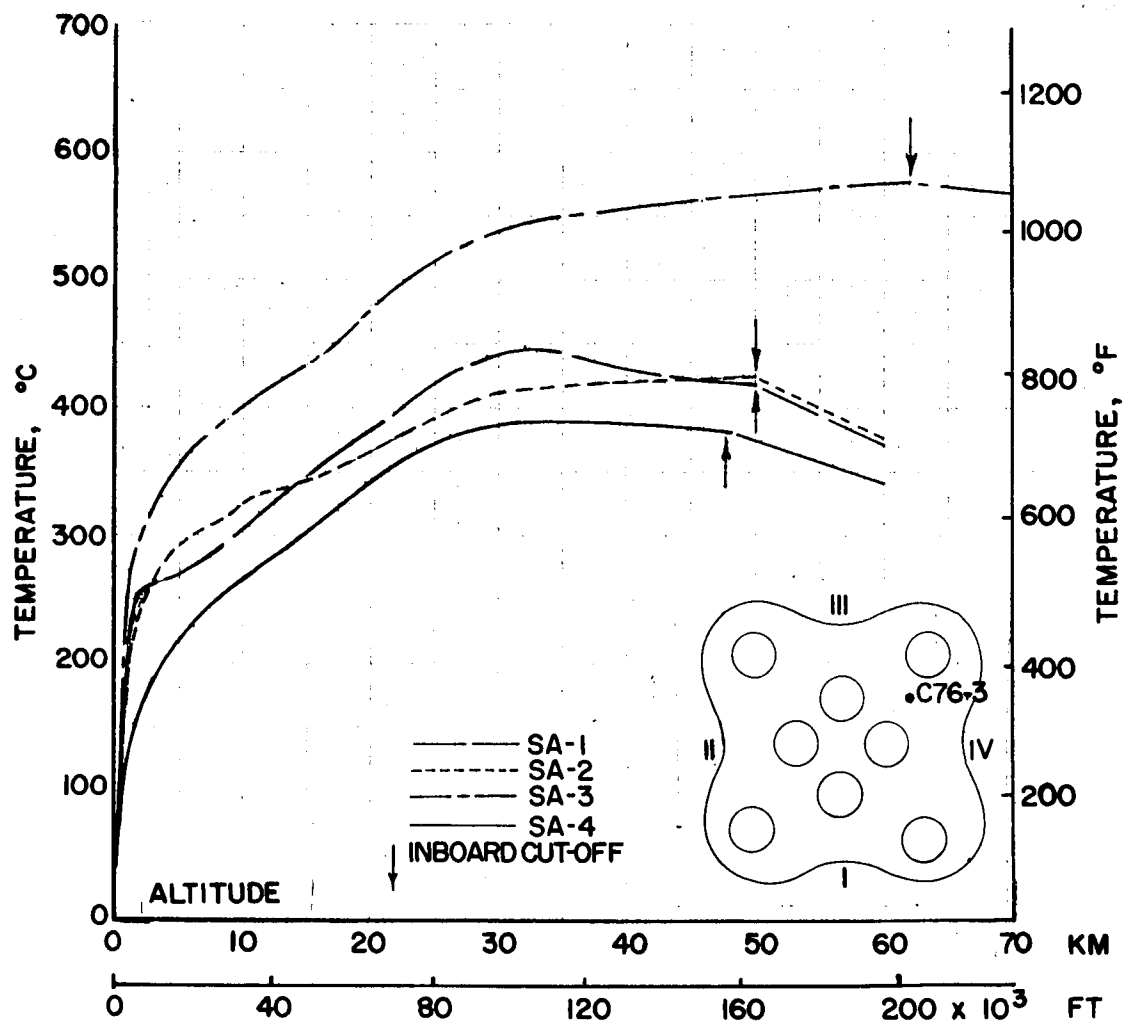
FIGURE 24. COMPARISON OF CALORIMETER SLUG TEMPERA-
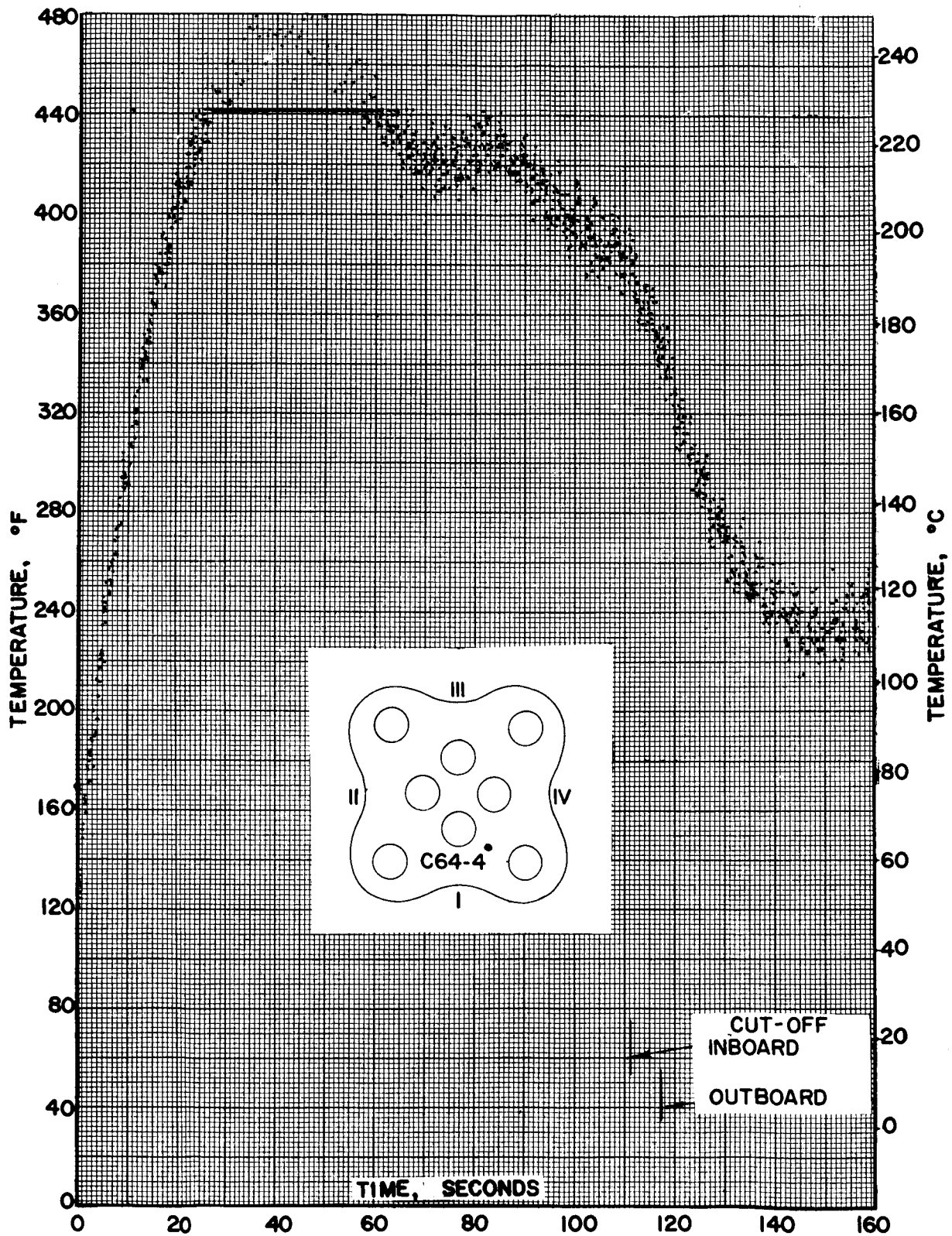TURE ON BASE OF SATURN I BLOCK I VEHICLES

66
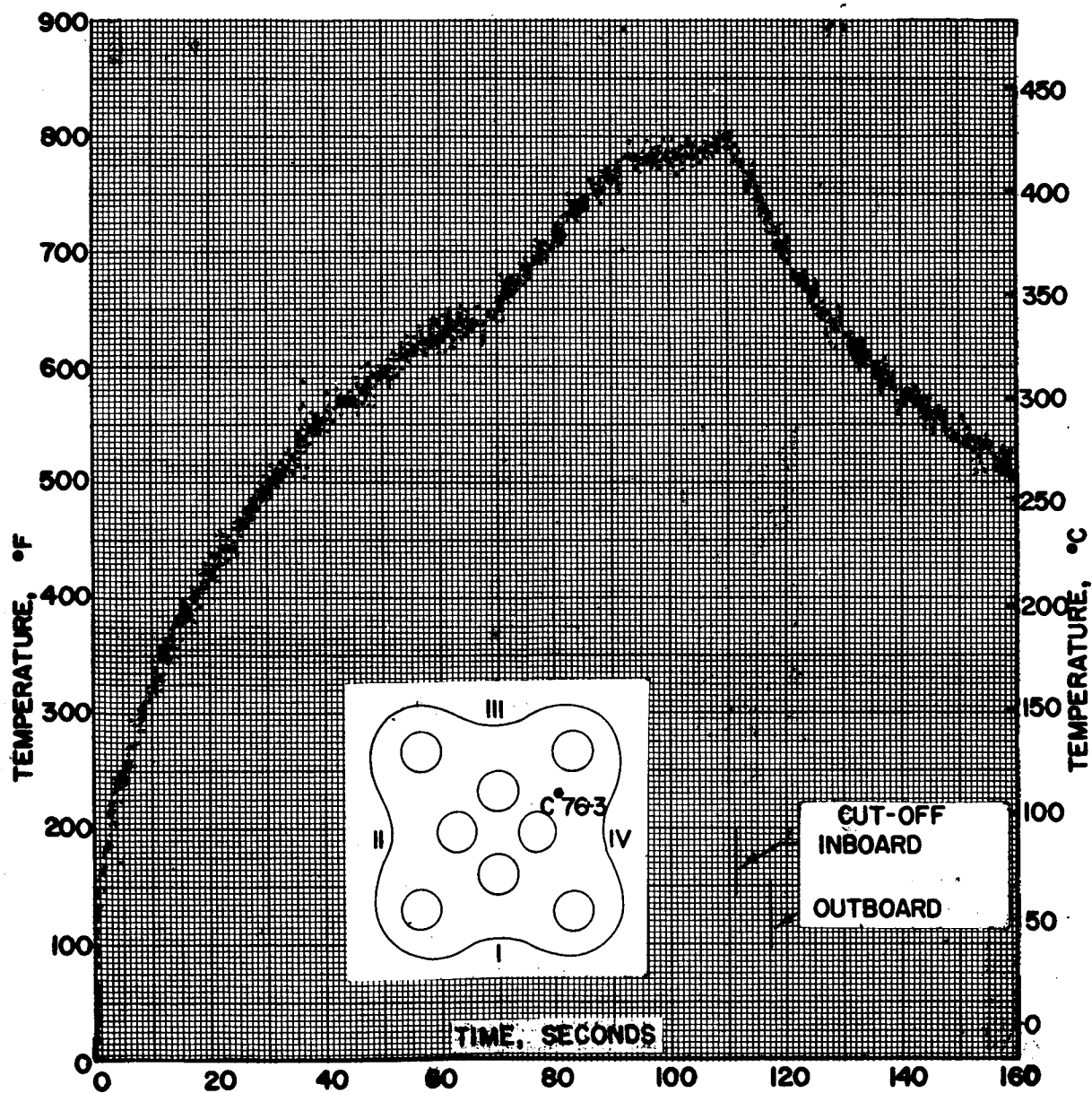
FIGURE 25. SATURN SA-2 FLIGHT TELEMETERED DATA

INFLIGHT CALIBRATION METHOD
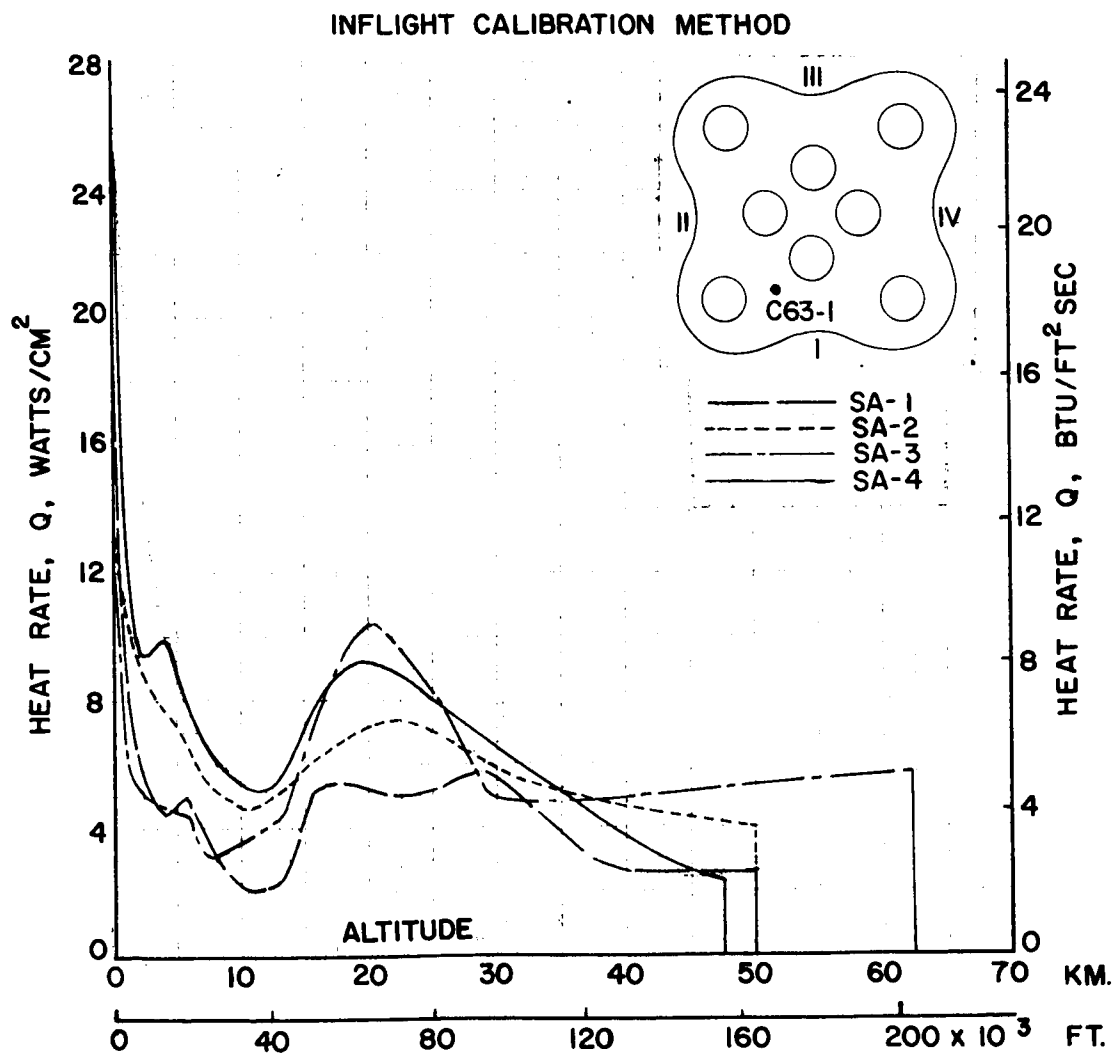
FIGURE 26a. COMPARISON OF TOTAL HEATING RATES ON
BASE OF SATURN I BLOCK I VEHICLES
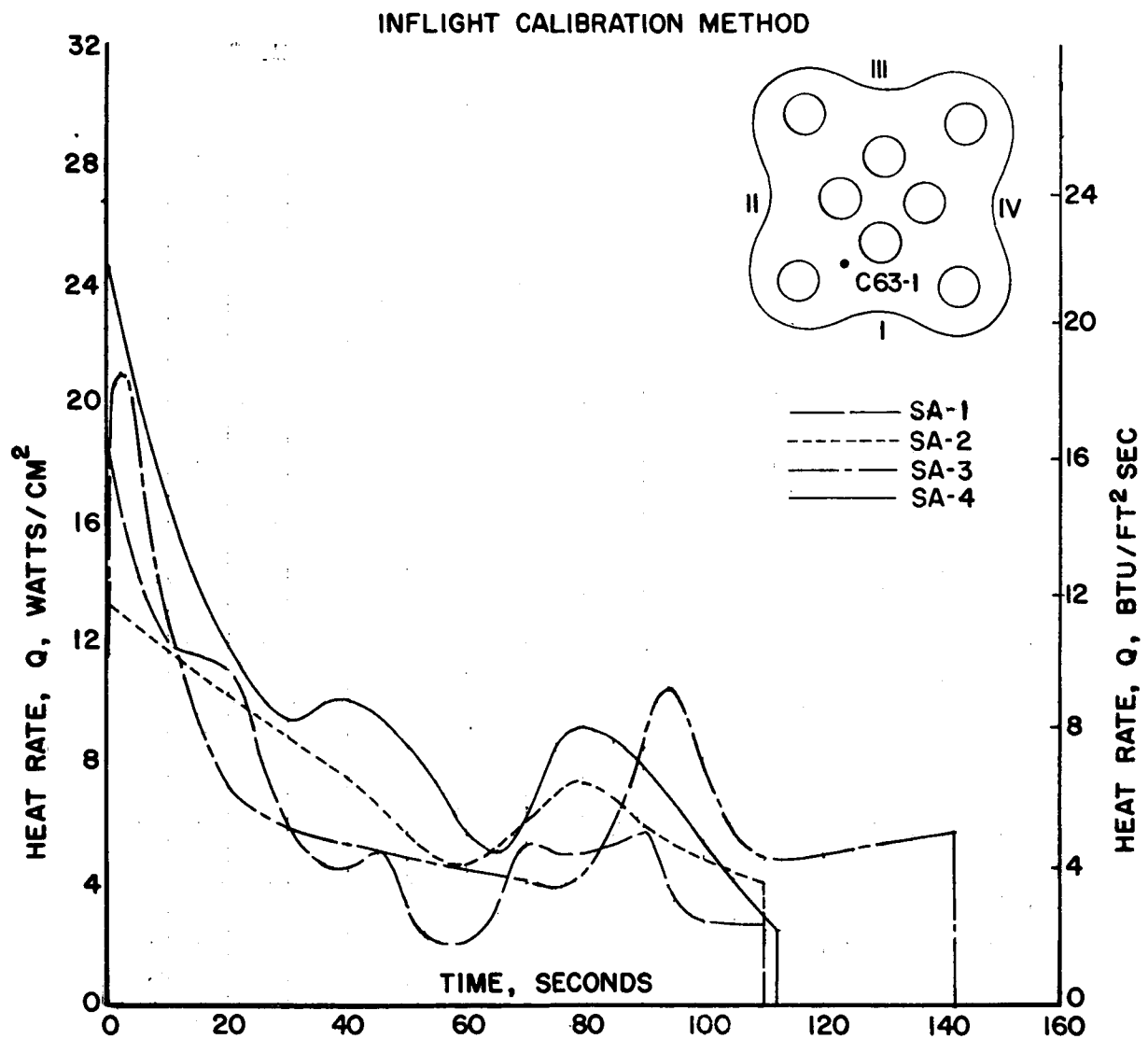
FIGURE 26b. COMPARISON OF TOTAL HEATING RATES ON
BASE OF SATURN I BLOCK I VEHICLES
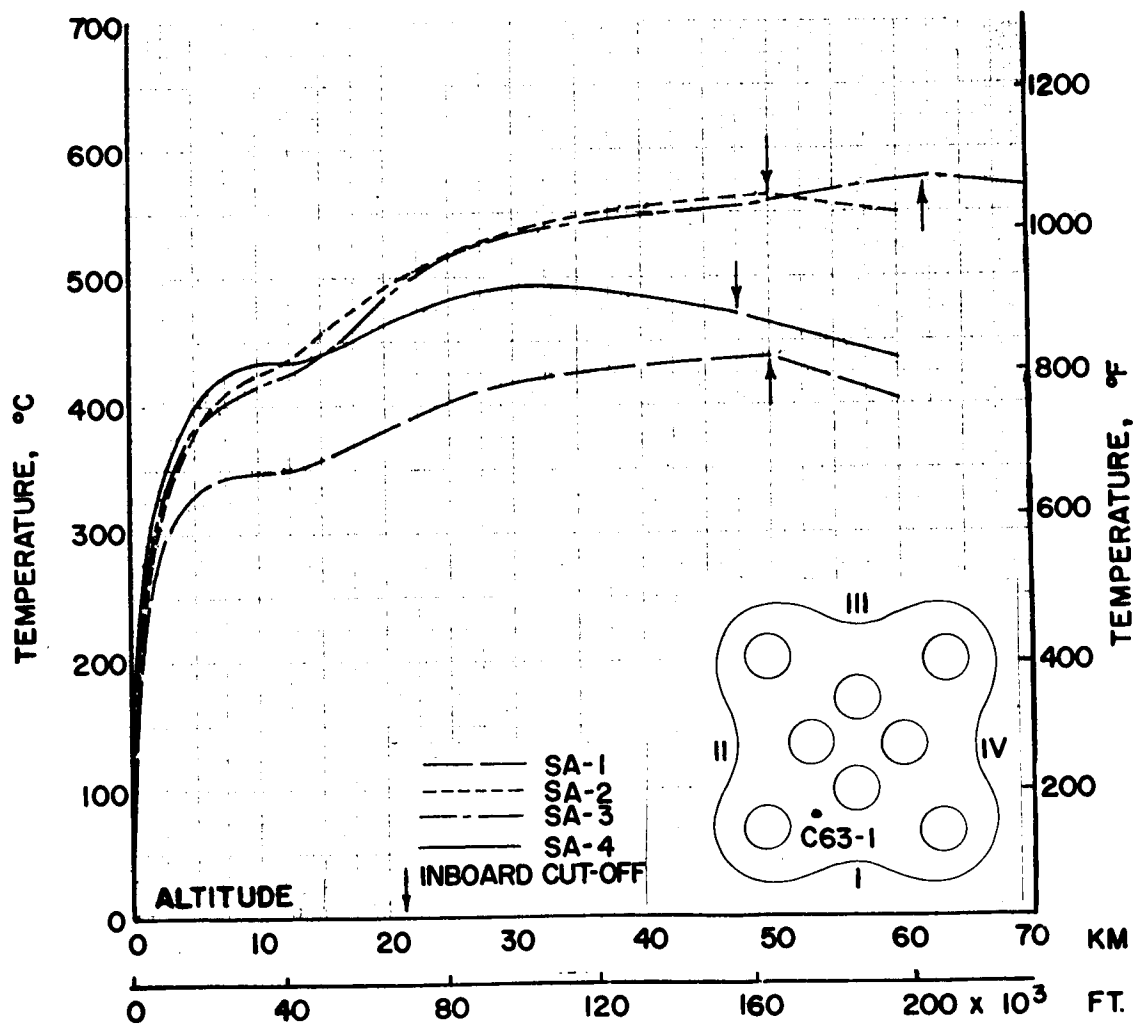
FIGURE 27. COMPARISON OF CALORIMETER SLUG TEMPERA-
TURE ON BASE OF SATURN I BLOCK I VEHICLES
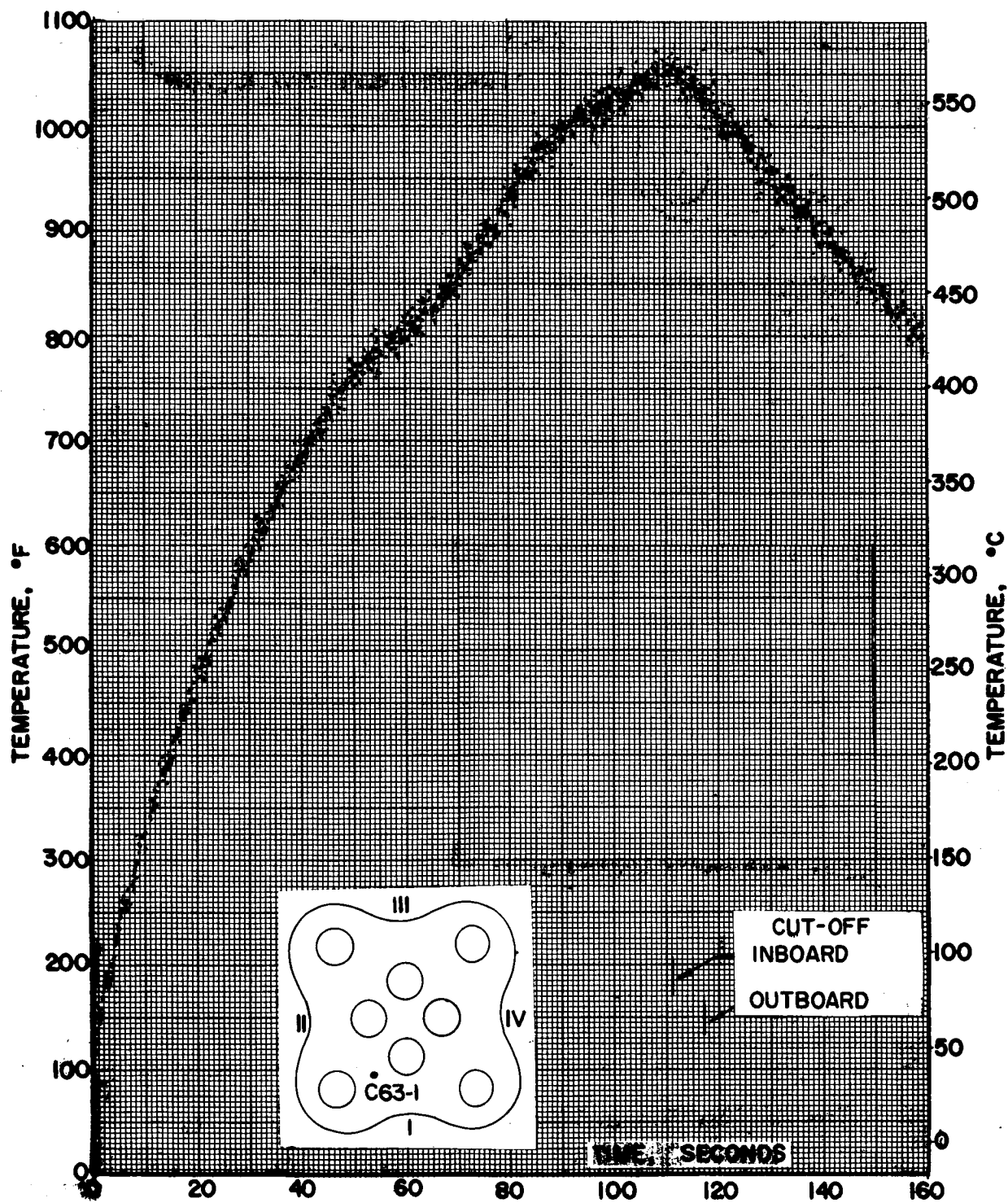
FIGURE 28. SATURN SA-2 FLIGHT TELEMETERED DATA

INFLIGHT CALIBRATION METHOD
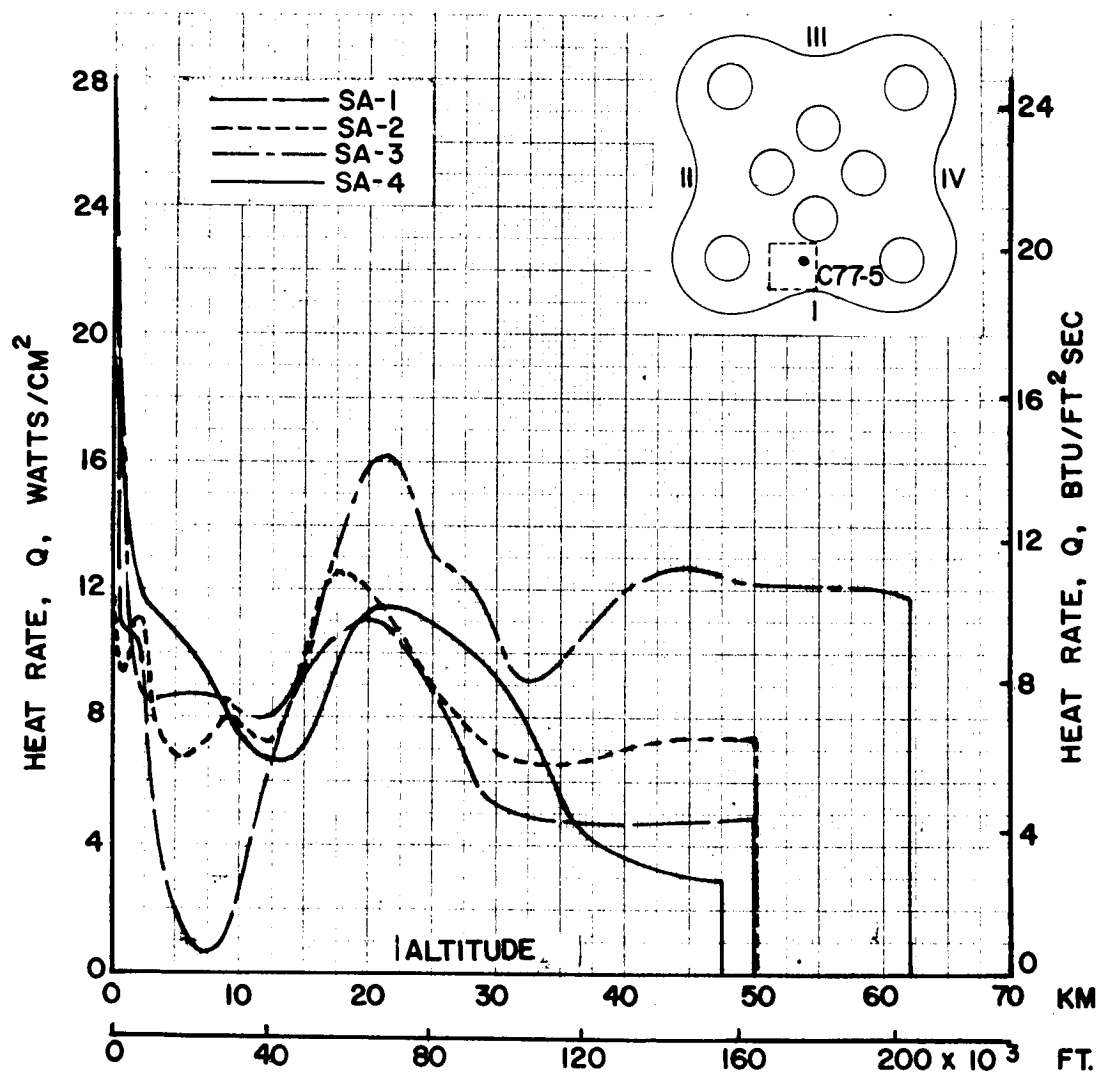
FIGURE 29a. COMPARISON OF TOTAL HEATING RATES ON
BASE OF SATURN I BLOCK I VEHICLES

INFLIGHT CALIBRATION METHOD
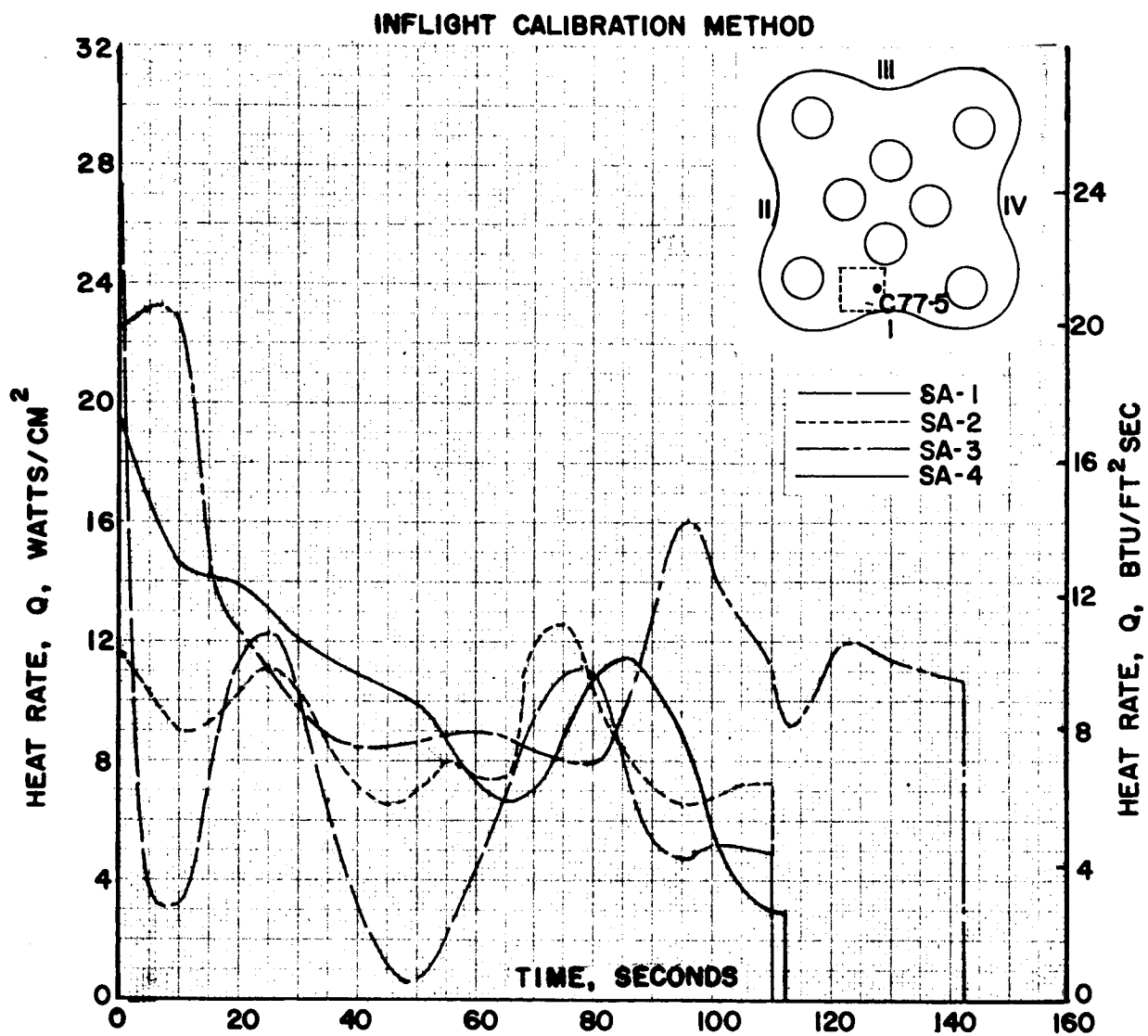
FIGURE 29b. COMPARISON OF TOTAL HEATING RATES ON
BASE OF SATURN I BLOCK I VEHICLES
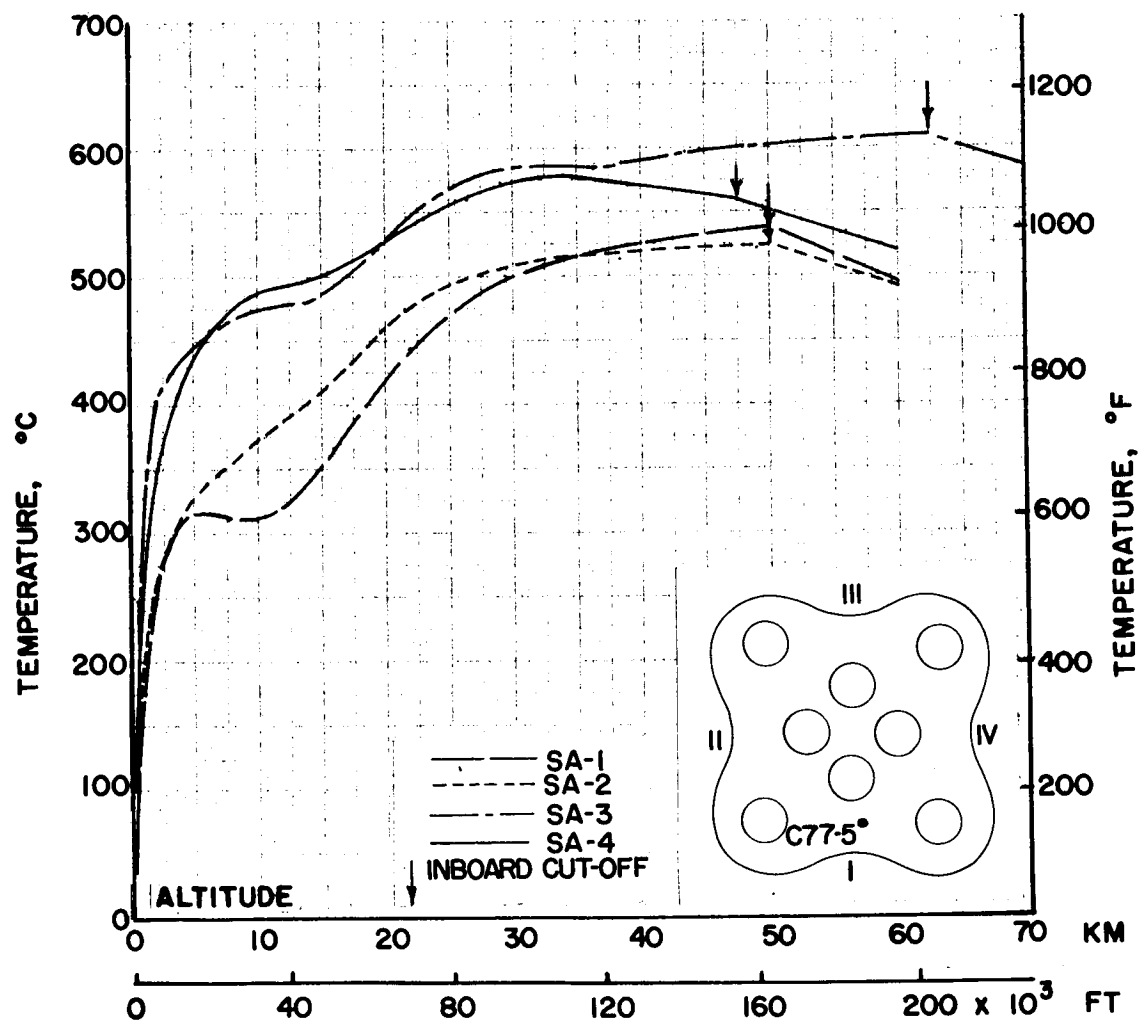
FIGURE 30. COMPARISON OF CALORIMETER SLUG TEMPERA-
TURE ON BASE OF SATURN I BLOCK I VEHICLES

74
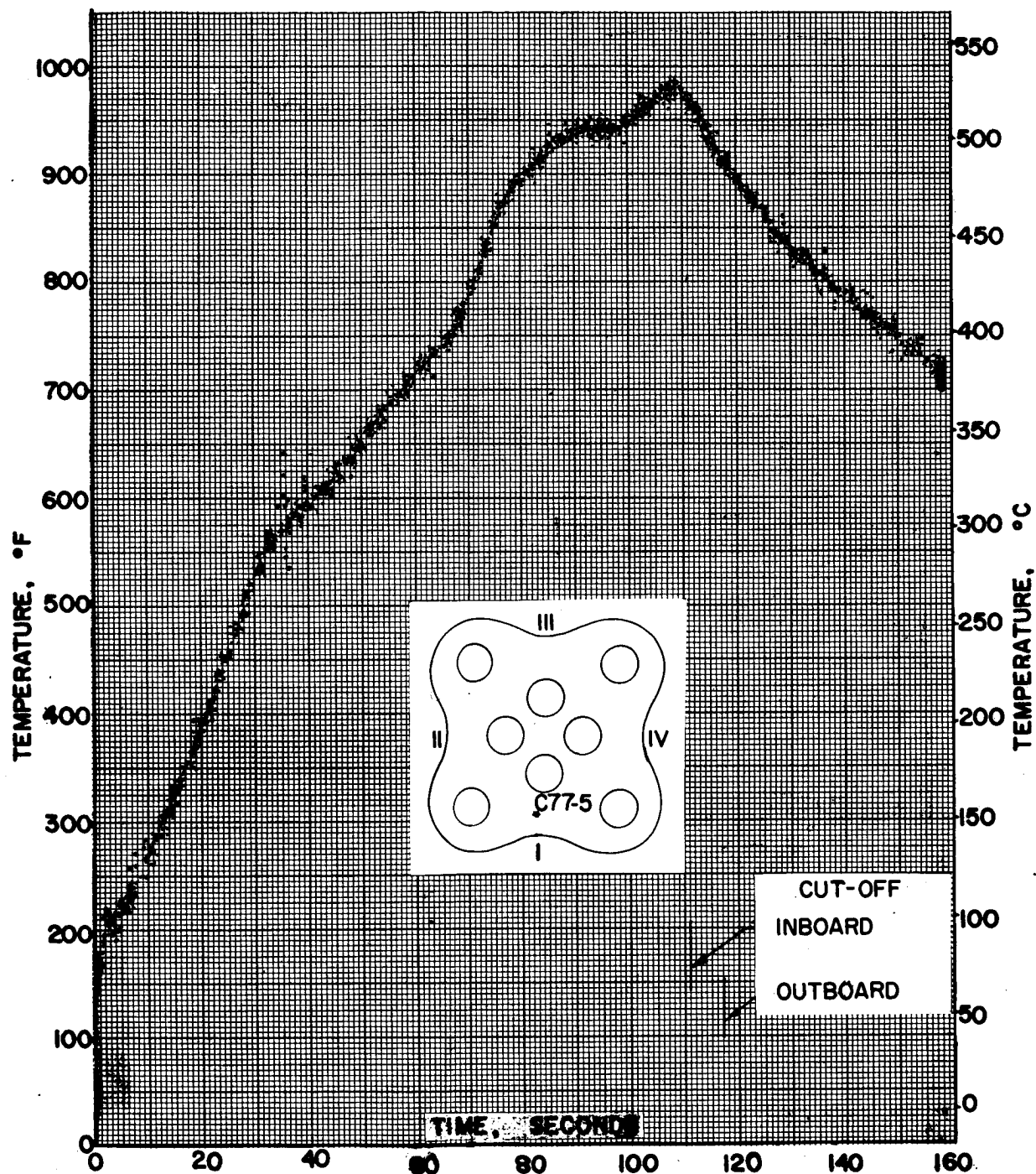
FIGURE 31. SATURN SA-2 FLIGHT TELEMETERED DATA
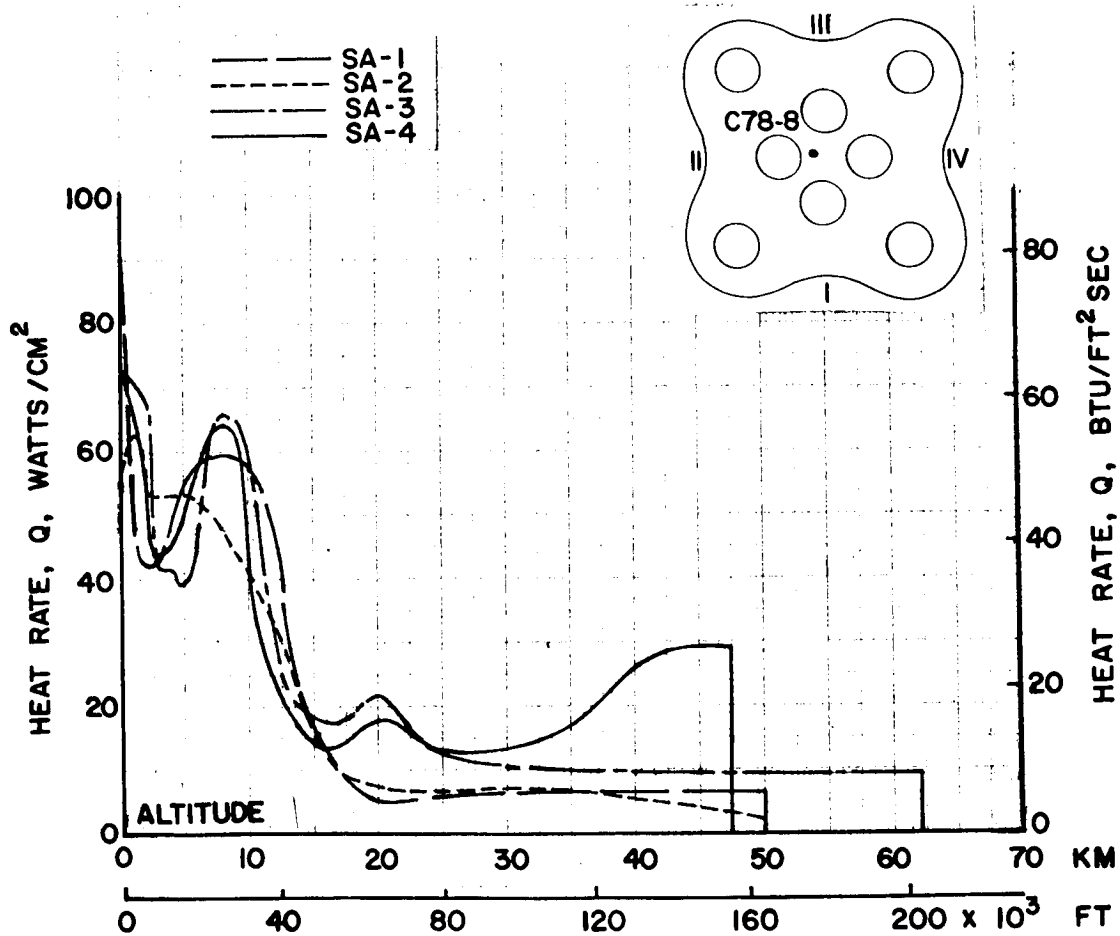
FIGURE 32a. COMPARISON OF FLAME SHIELD HEATING
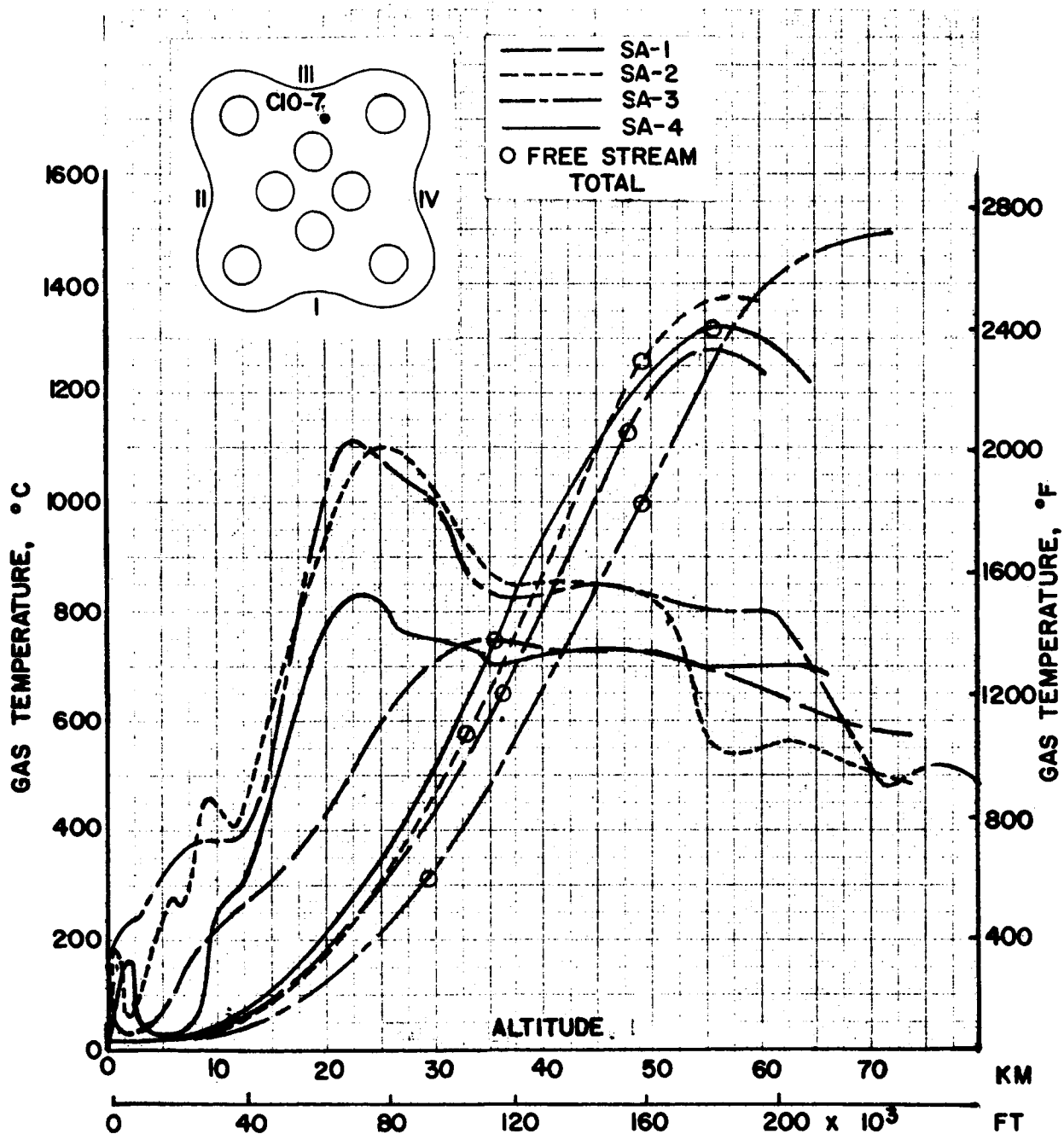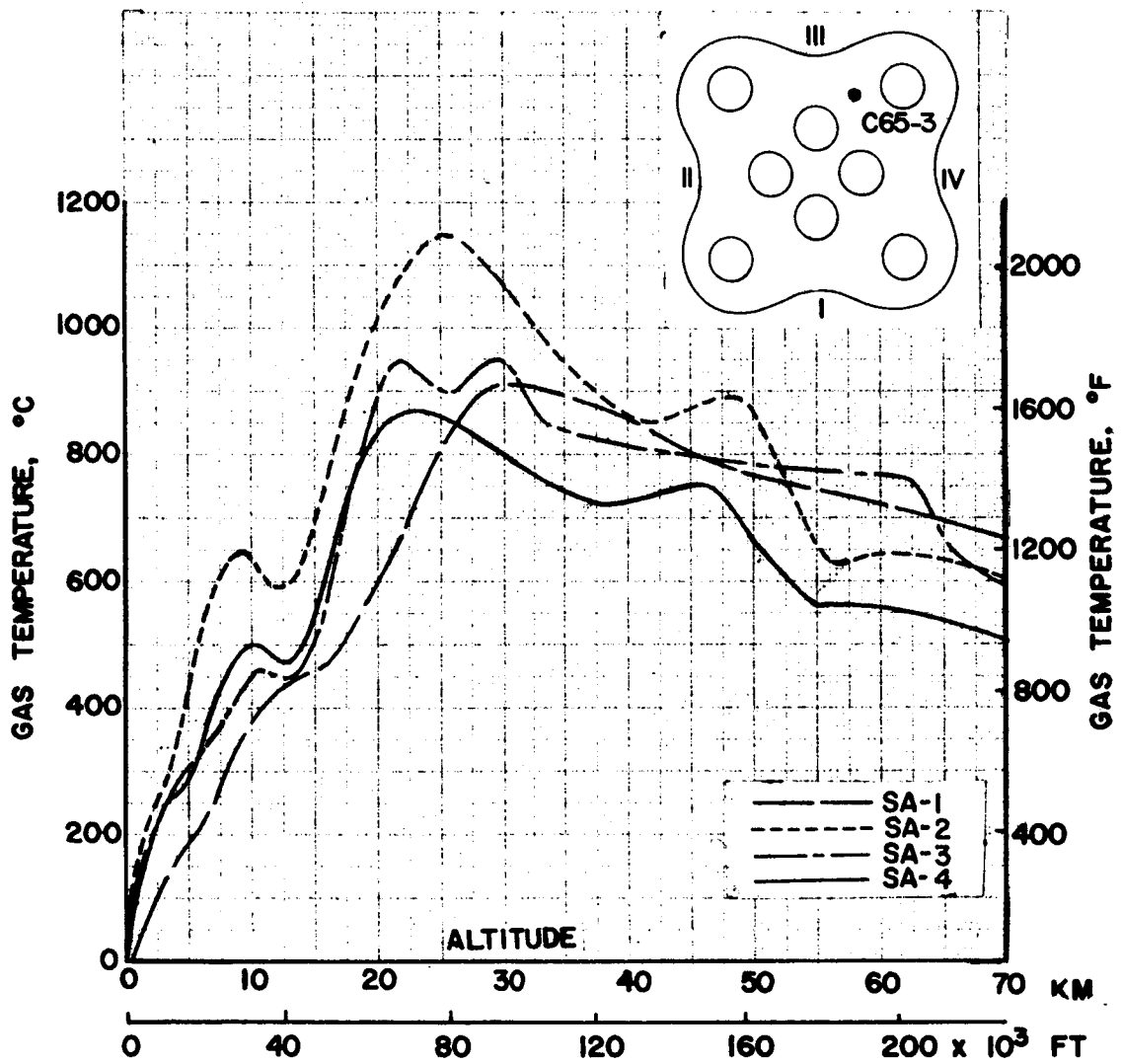RATES ON SATURN I BLOCK I VEHICLES
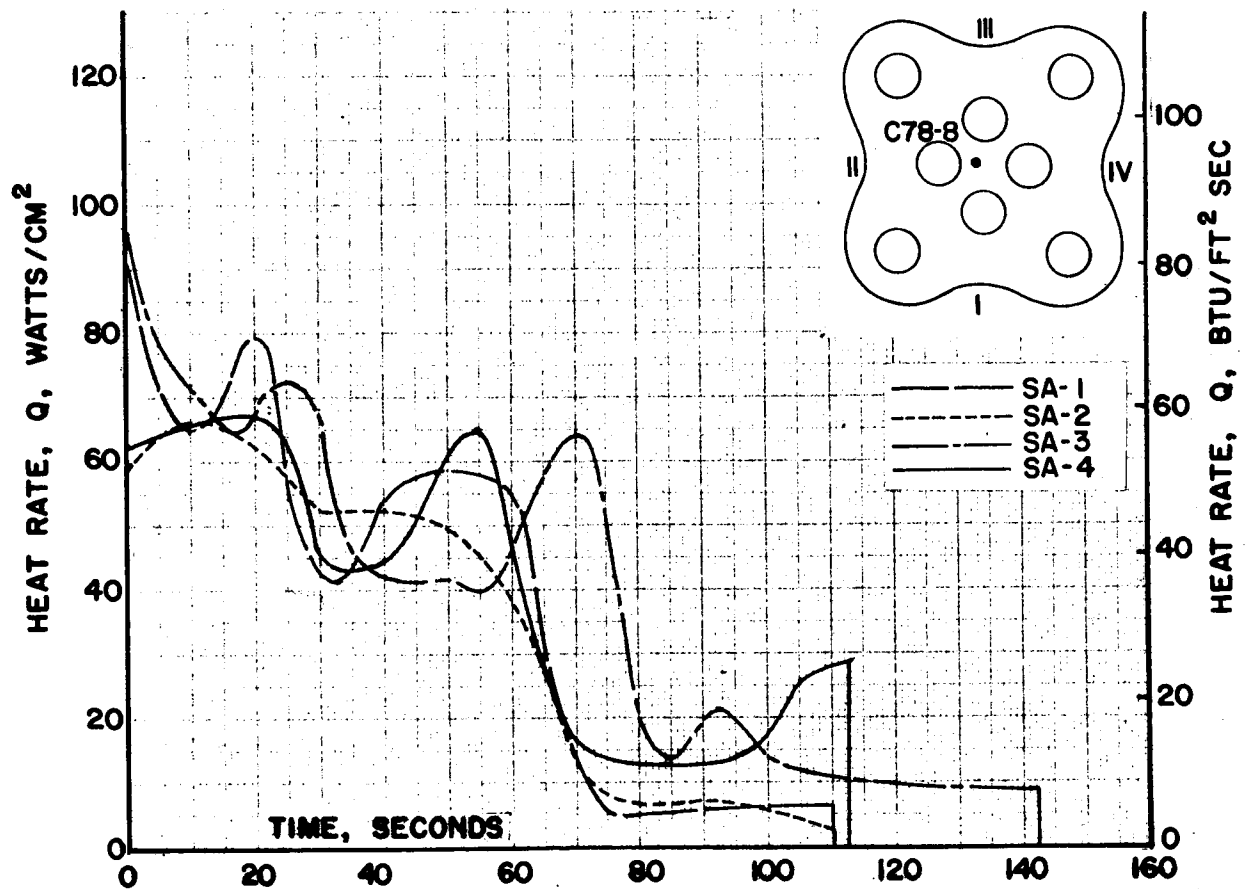
FIGURE 32b. COMPARISON OF FLAME SHIELD HEATING
RATES ON SATURN I BLOCK I VEHICLES

77
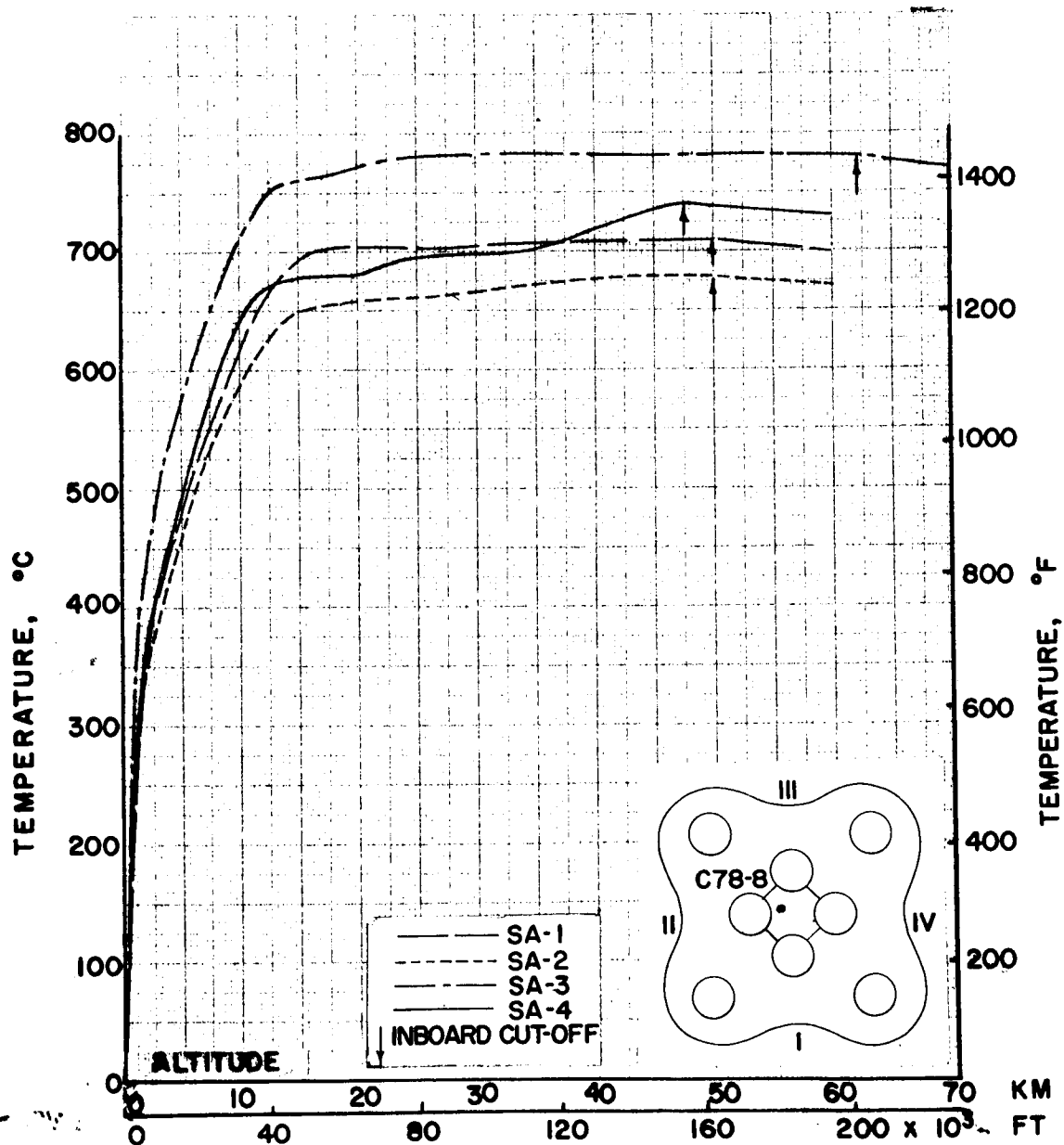
FIGURE 33. COMPARISON OF FLAME SHIELD CALORIMETER
        SLUG TEMPERATURE ON BASE OF SATURN I
        BLOCK I VEHICLES
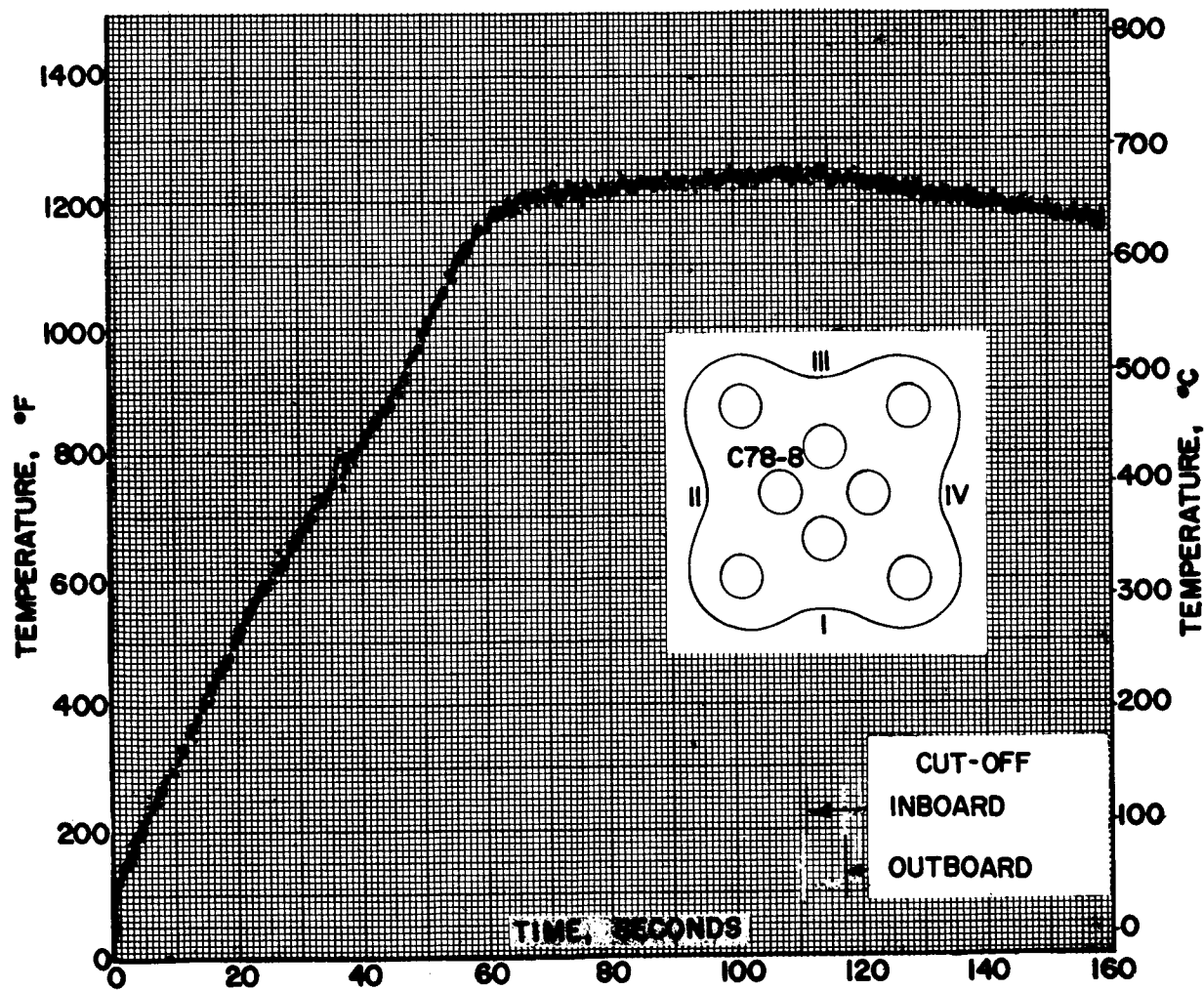
FIGURE 34. SATURN SA-2 FLIGHT TELEMETERED DATA

FLAME SHIELD

HEAT SHIELD

FLAME SHIELD

LOW ALTITUDE FLOW

SHOCK   WAKE

FLAME SHIELD

HIGH ALTITUDE FLOW
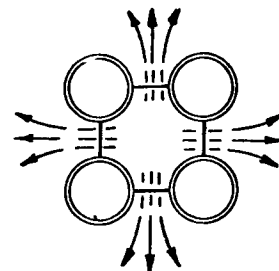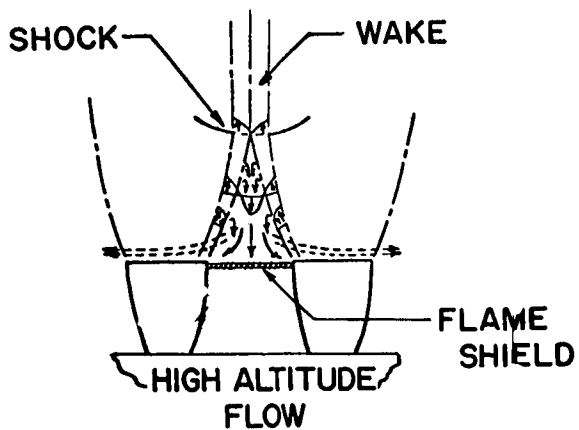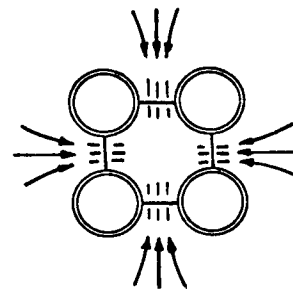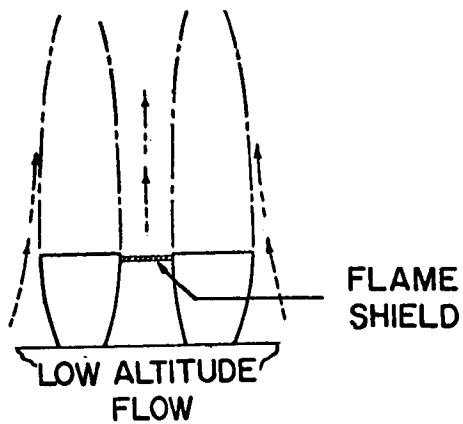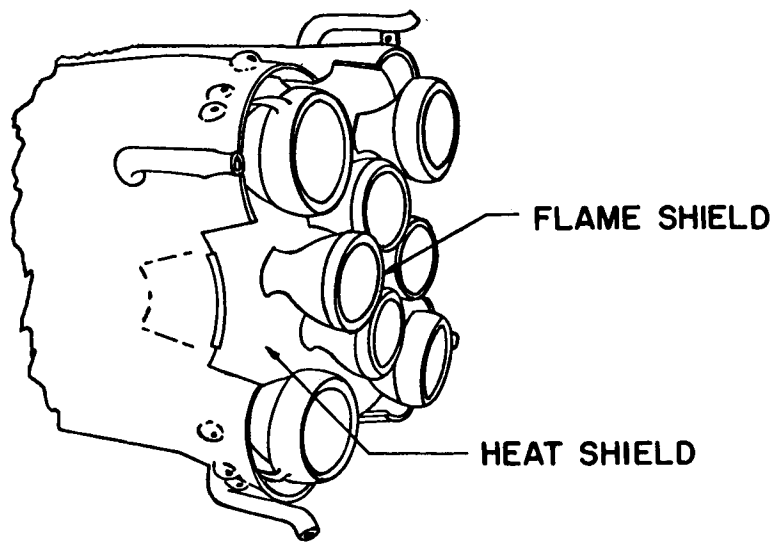
FIGURE 35.   FLOW ABOUT SATURN FLAME SHIELD
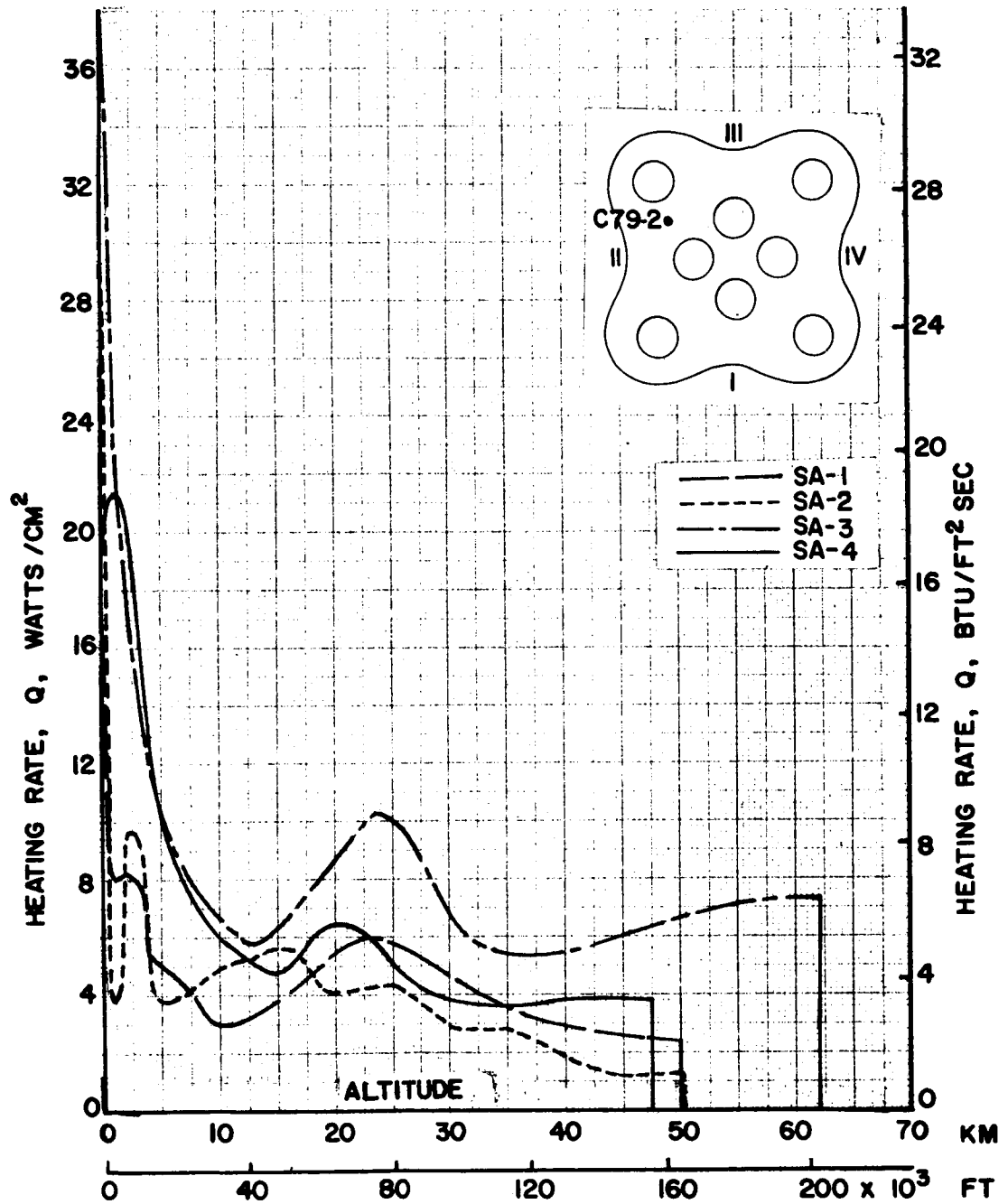
FIGURE 36a. COMPARISON OF RADIATIVE HEATING RATES ON BASE OF SATURN I BLOCK I VEHICLES

INFLIGHT CALIBRATION METHOD
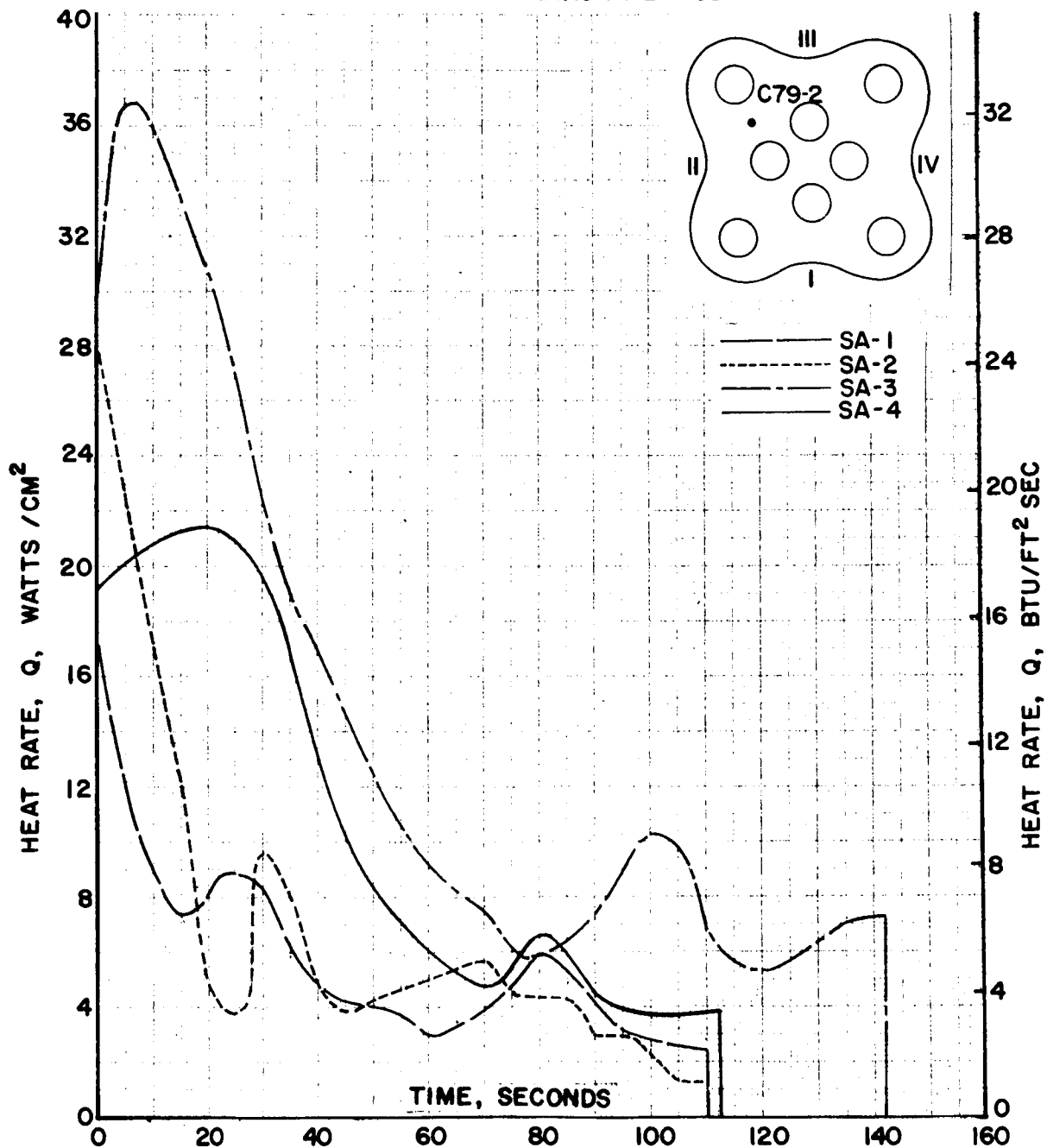
FIGURE 36b. COMPARISON OF RADIATIVE HEATING RATES
ON BASE OF SATURN I BLOCK I VEHICLES
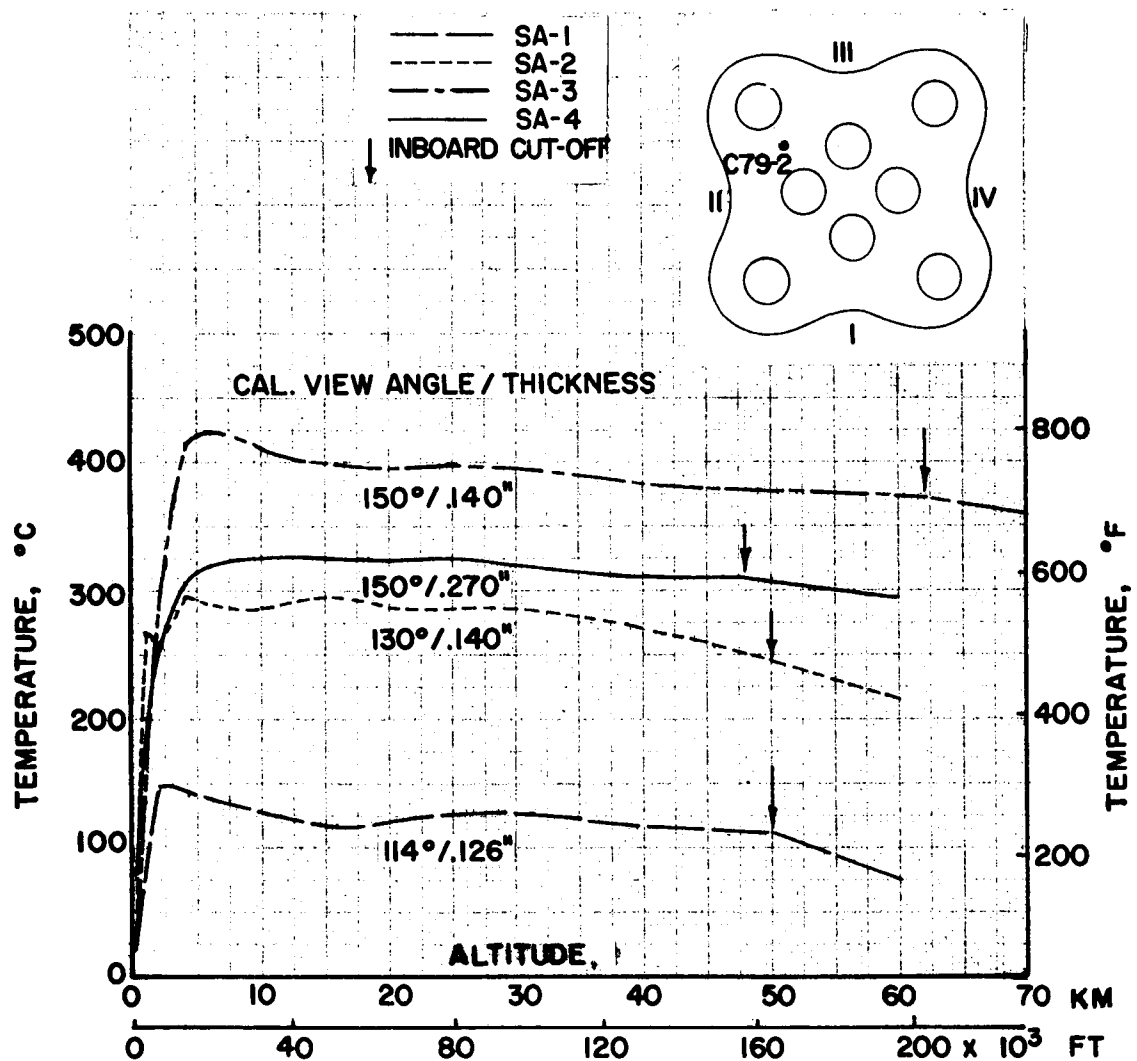
FIGURE 37. COMPARISON OF RADIATION CALORIMETER
SLUG TEMPERATURE ON BASE OF SATURN I
BLOCK I VEHICLES
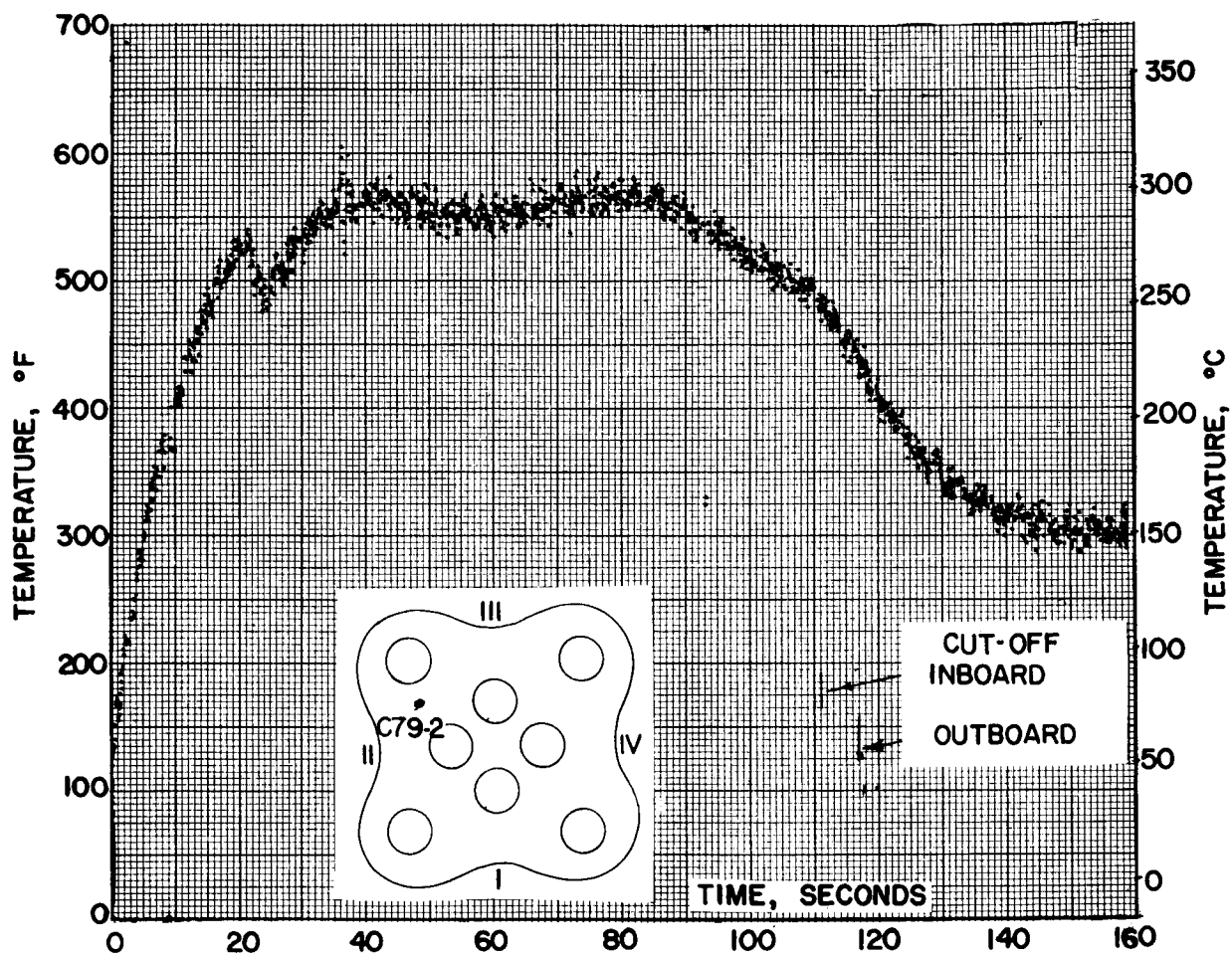
FIGURE 38. SATURN SA-2 FLIGHT TELEMETERED DATA
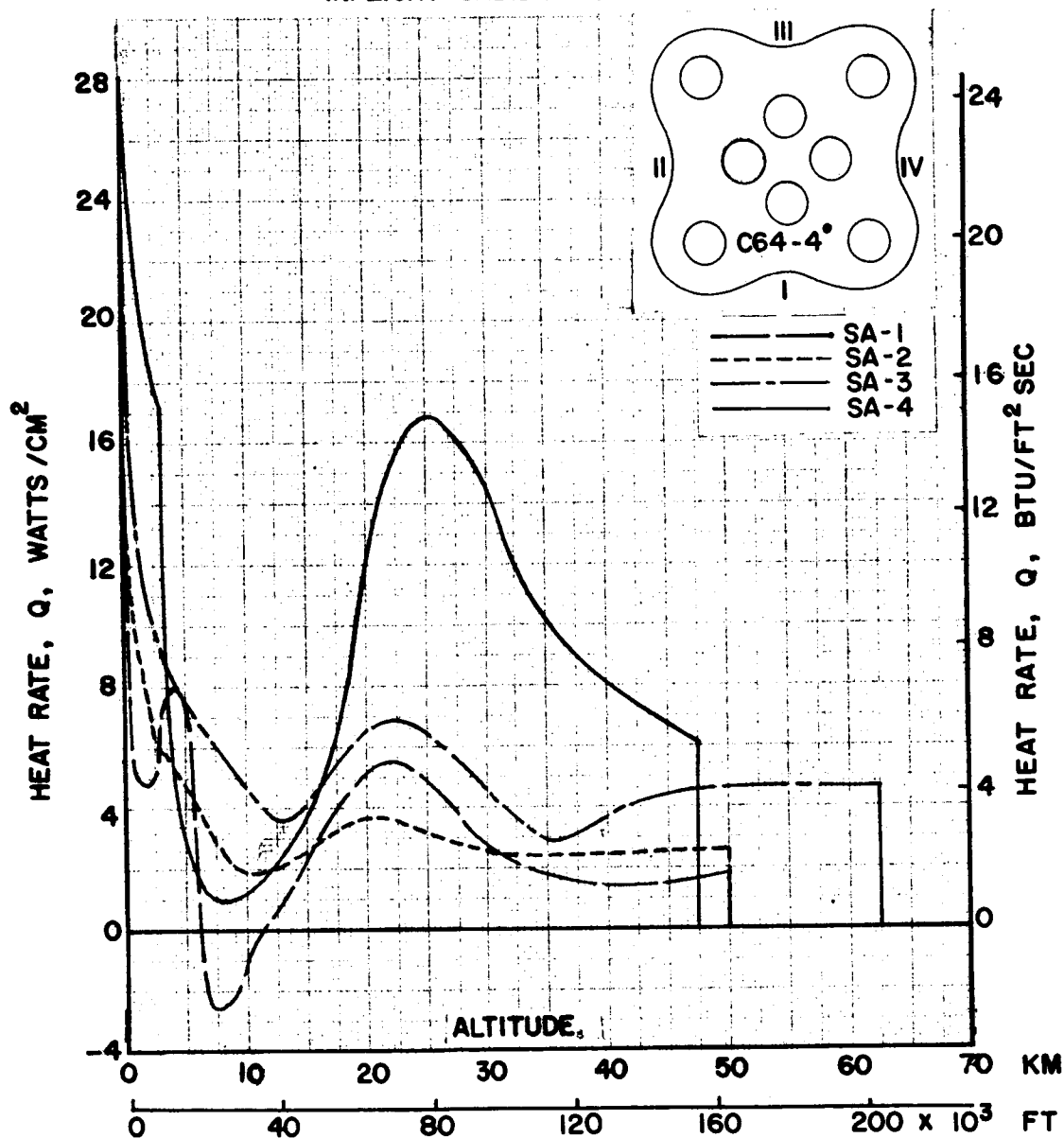
FIGURE 39a. COMPARISON OF RADIATIVE HEATING RATES
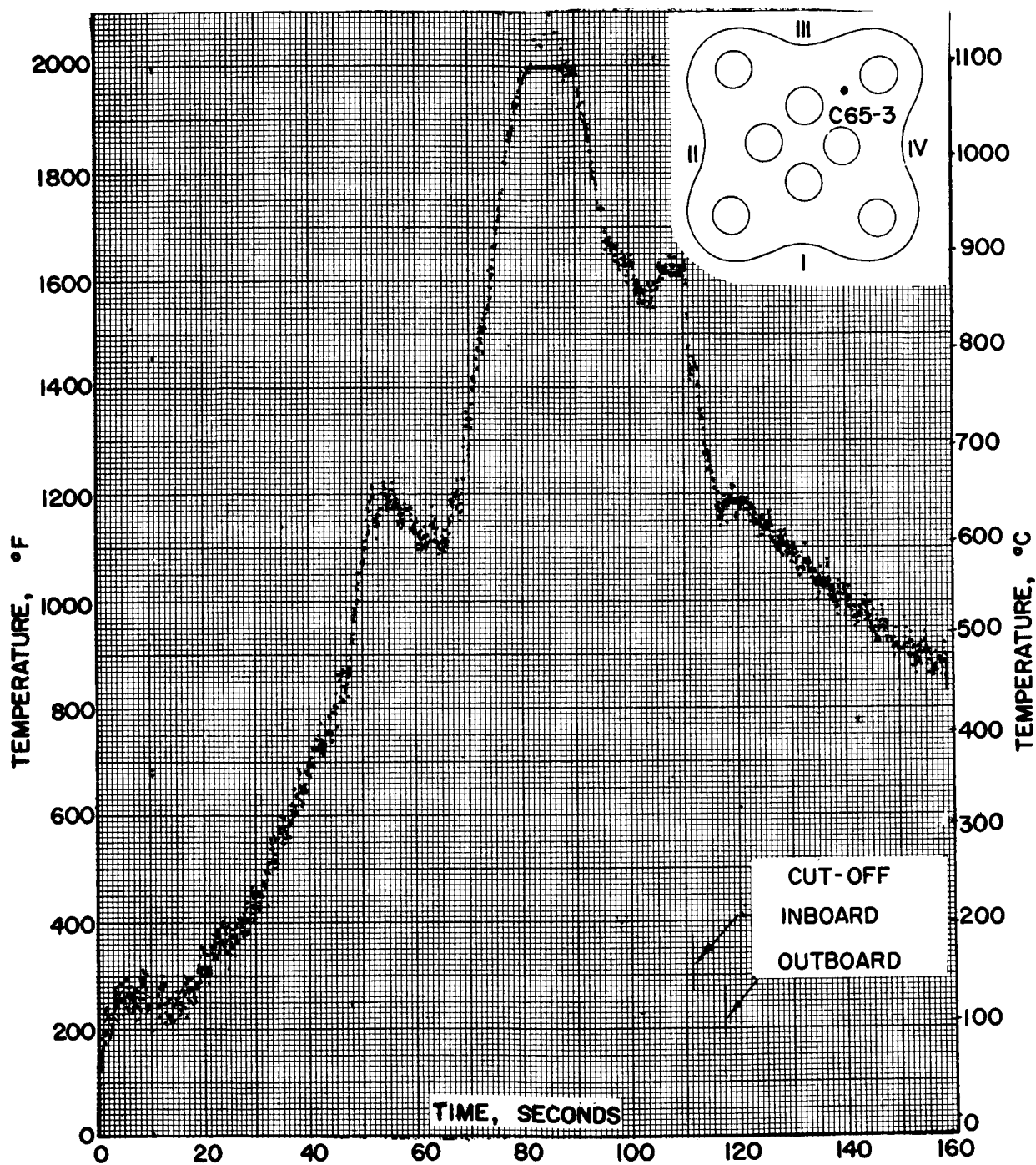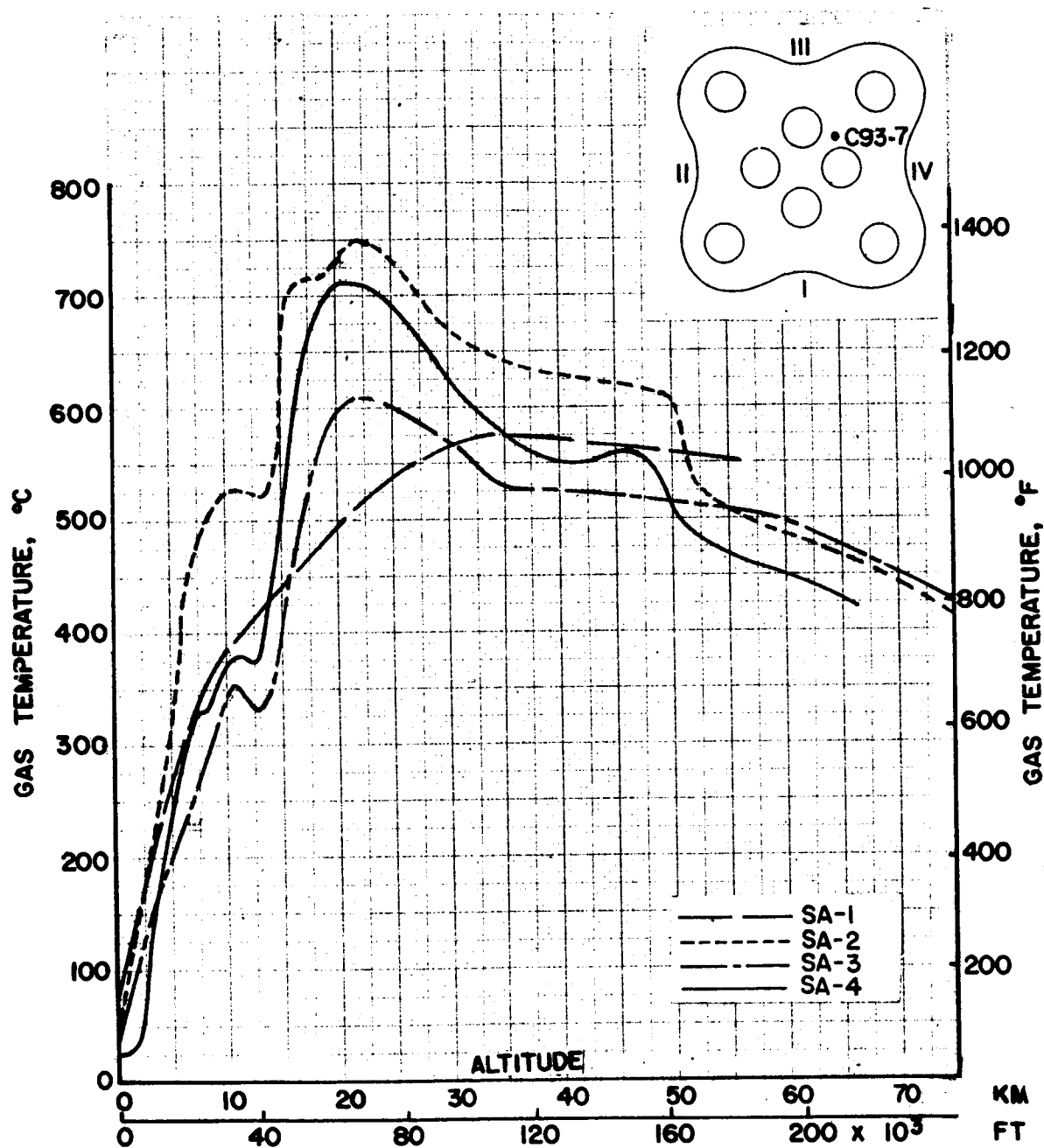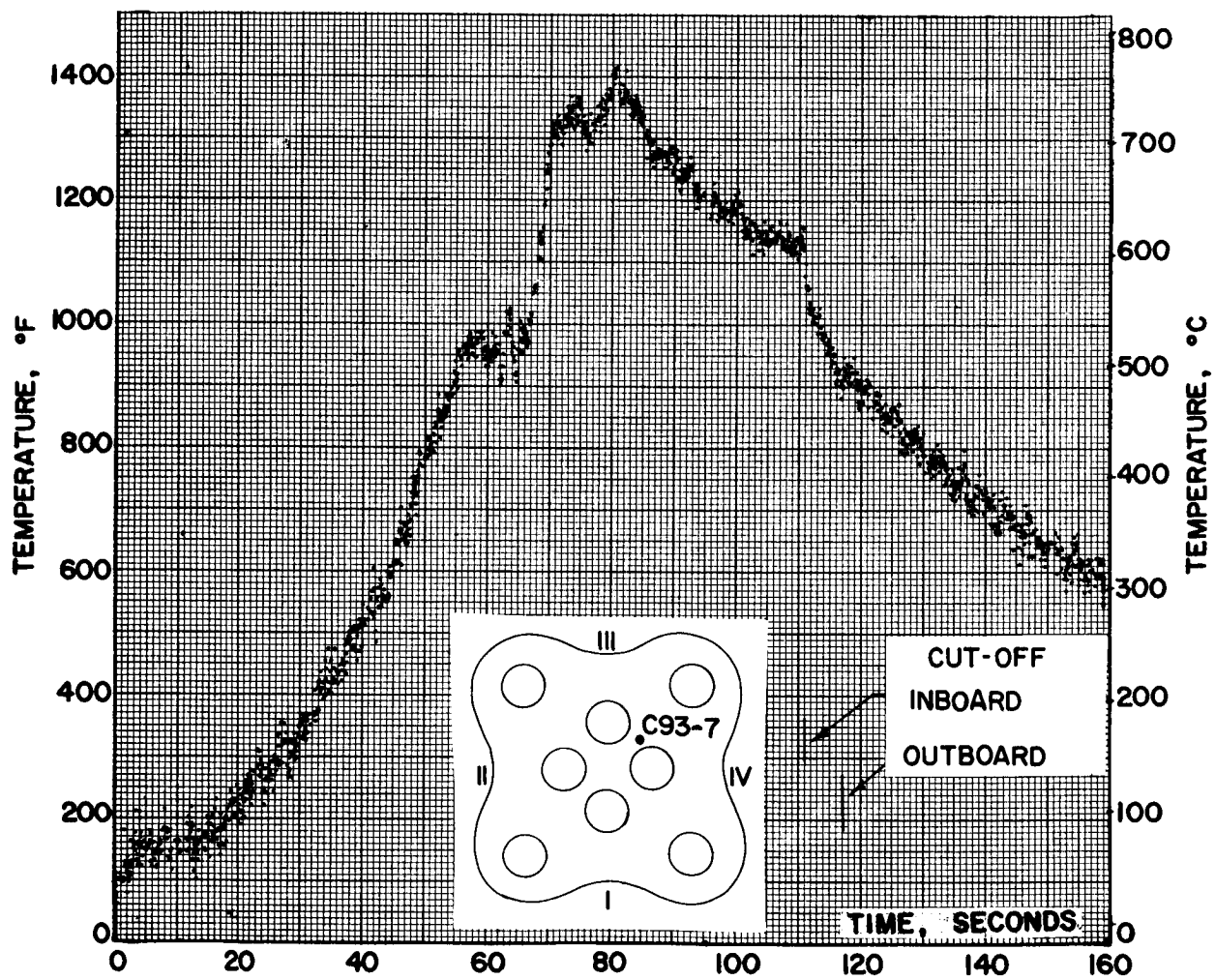ON BASE OF SATURN I BLOCK I VEHICLES

INFLIGHT CALIBRATION METHOD
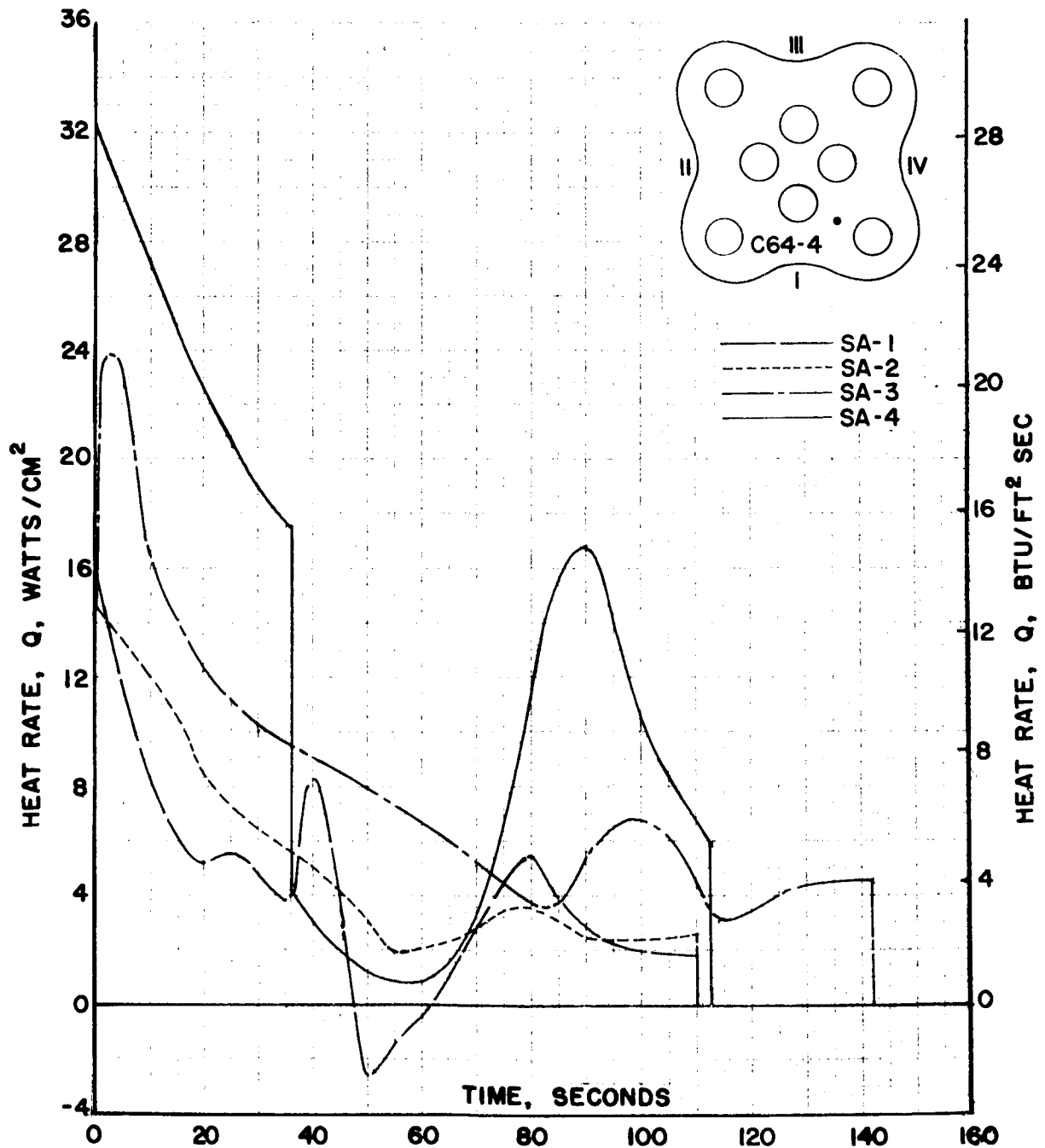
FIGURE 39b. COMPARISON OF RADIATIVE HEATING RATES
ON BASE OF SATURN I BLOCK I VEHICLES

86
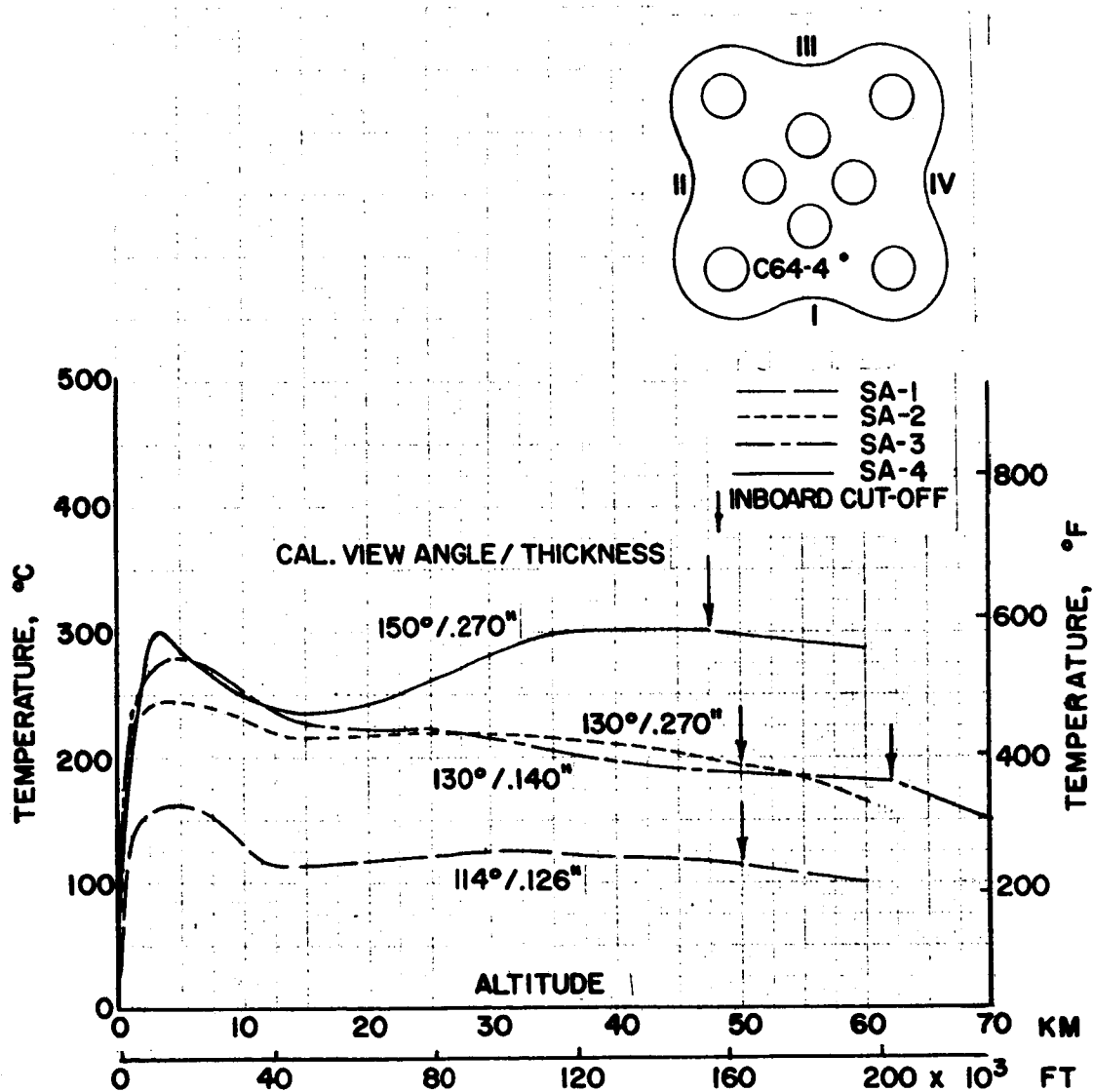
FIGURE 40. COMPARISON OF RADIATION CALORIMETER
SLUG TEMPERATURE ON BASE OF SATURN I
BLOCK I VEHICLES

FIGURE 41. SATURN SA-2 FLIGHT TELEMETERED DATA

88
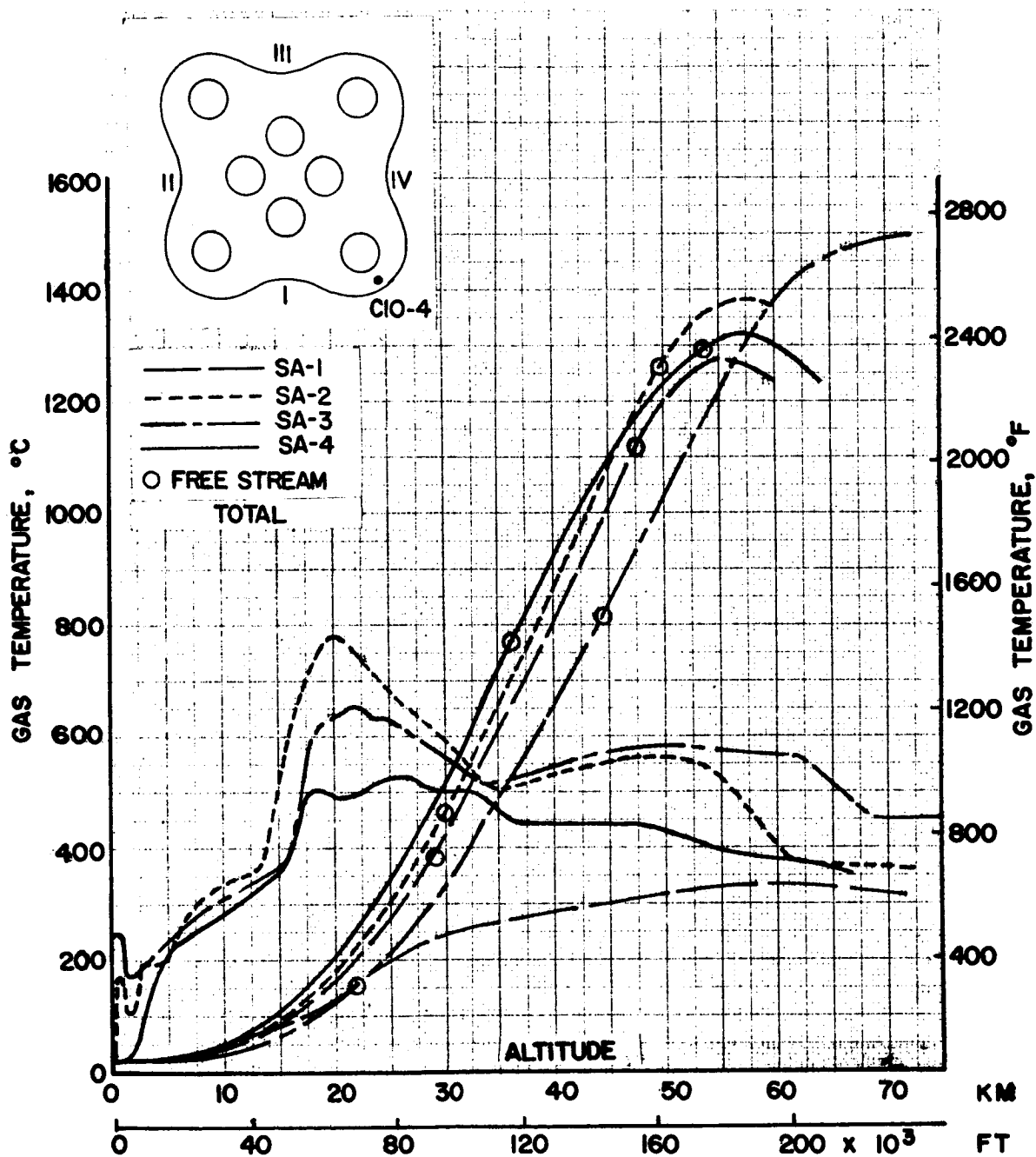
FIGURE 42. COMPARISON OF GAS TEMPERATURES ON
BASE OF SATURN I BLOCK I VEHICLES

89
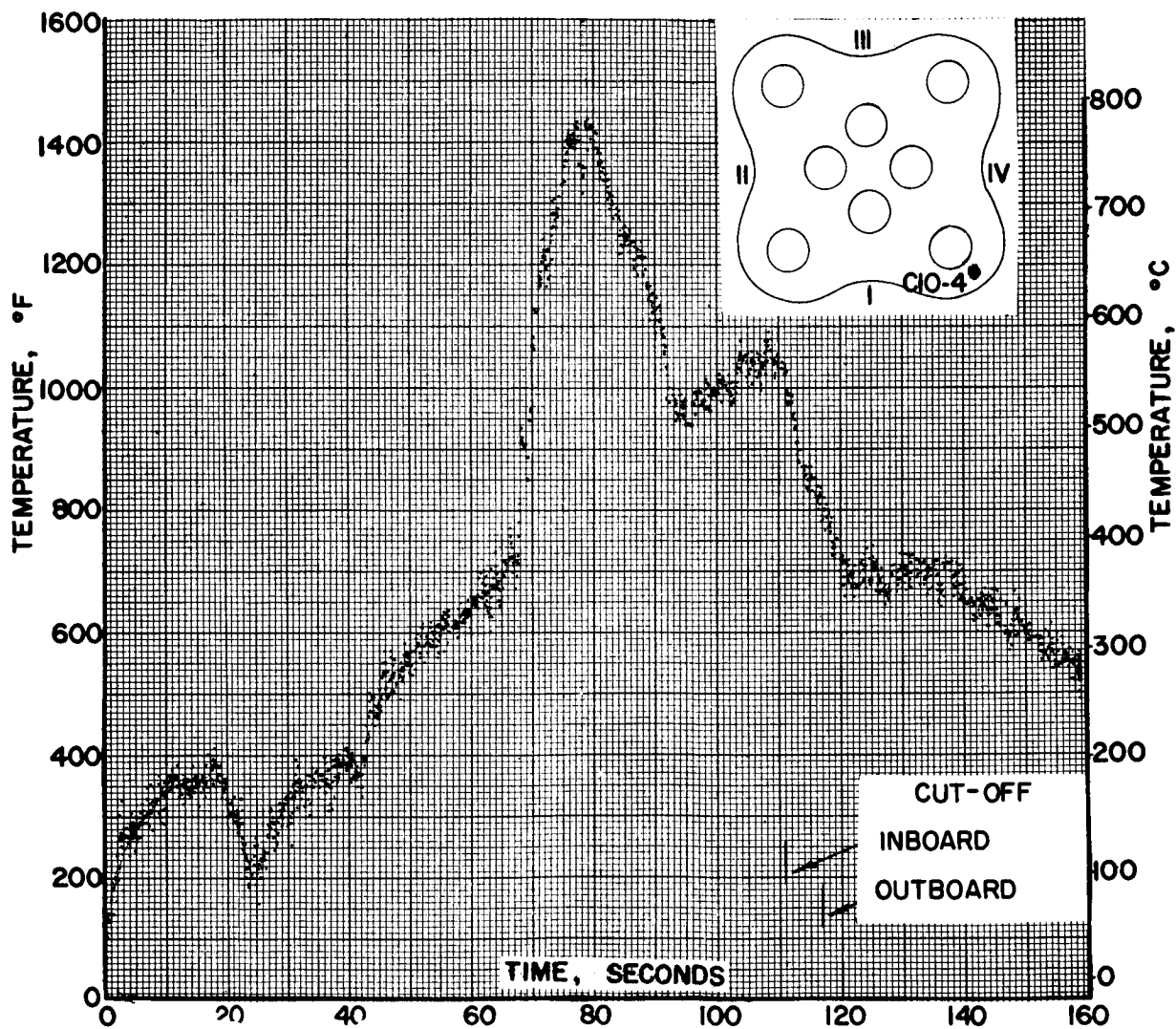
FIGURE 43. SATURN SA-2 FLIGHT TELEMETERED DATA
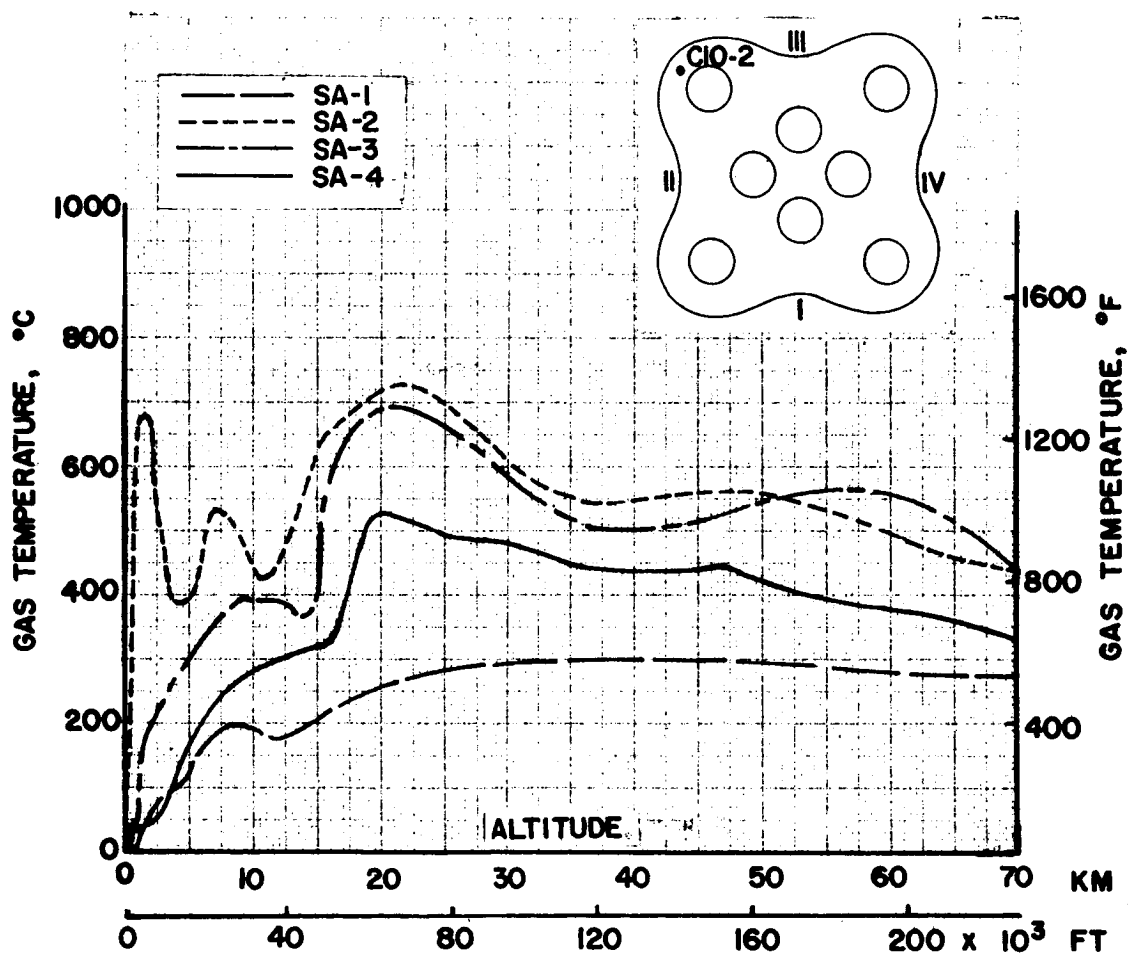
FIGURE 44. COMPARISON OF GAS TEMPERATURES ON
BASE OF SATURN I BLOCK I VEHICLES
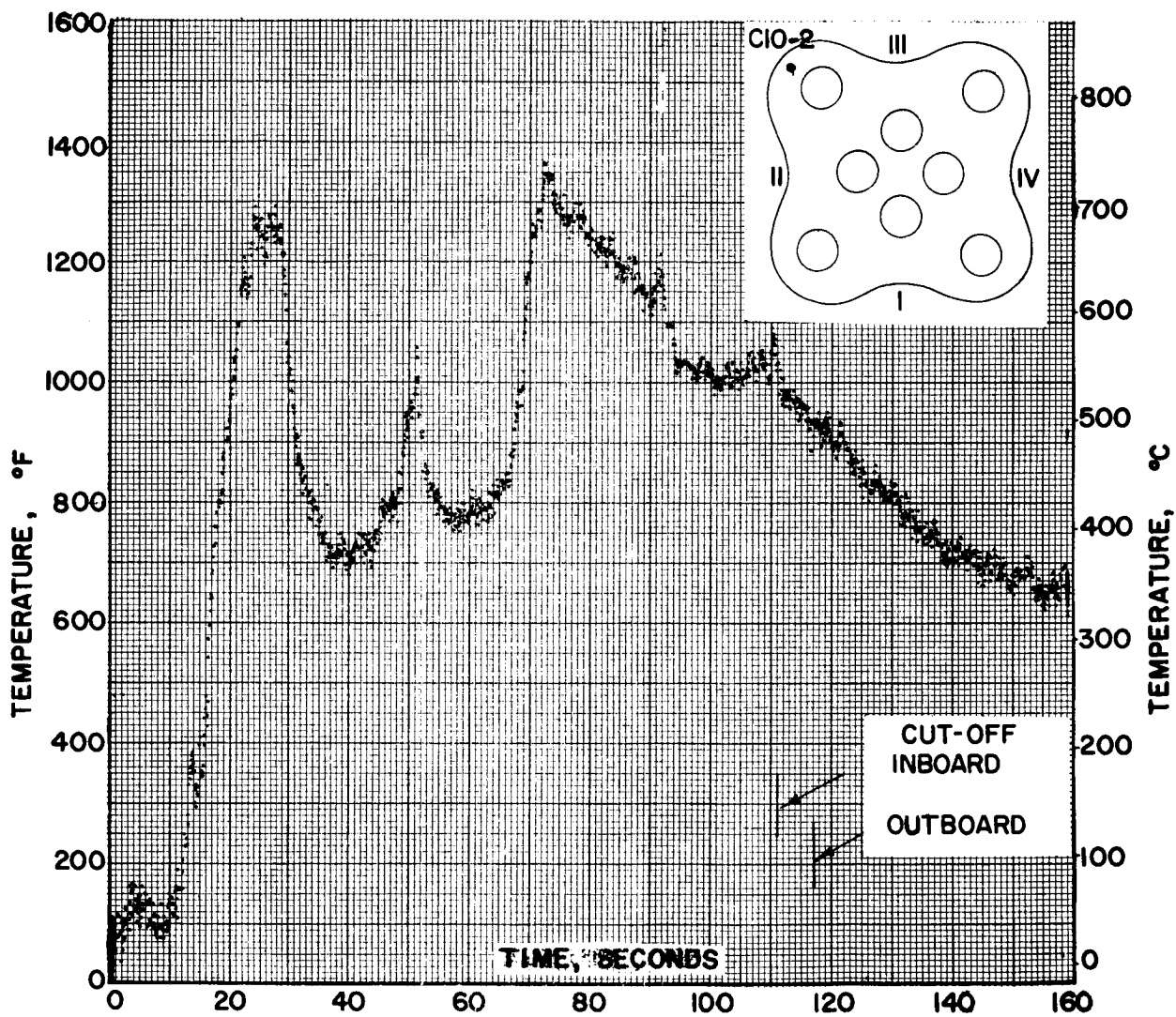
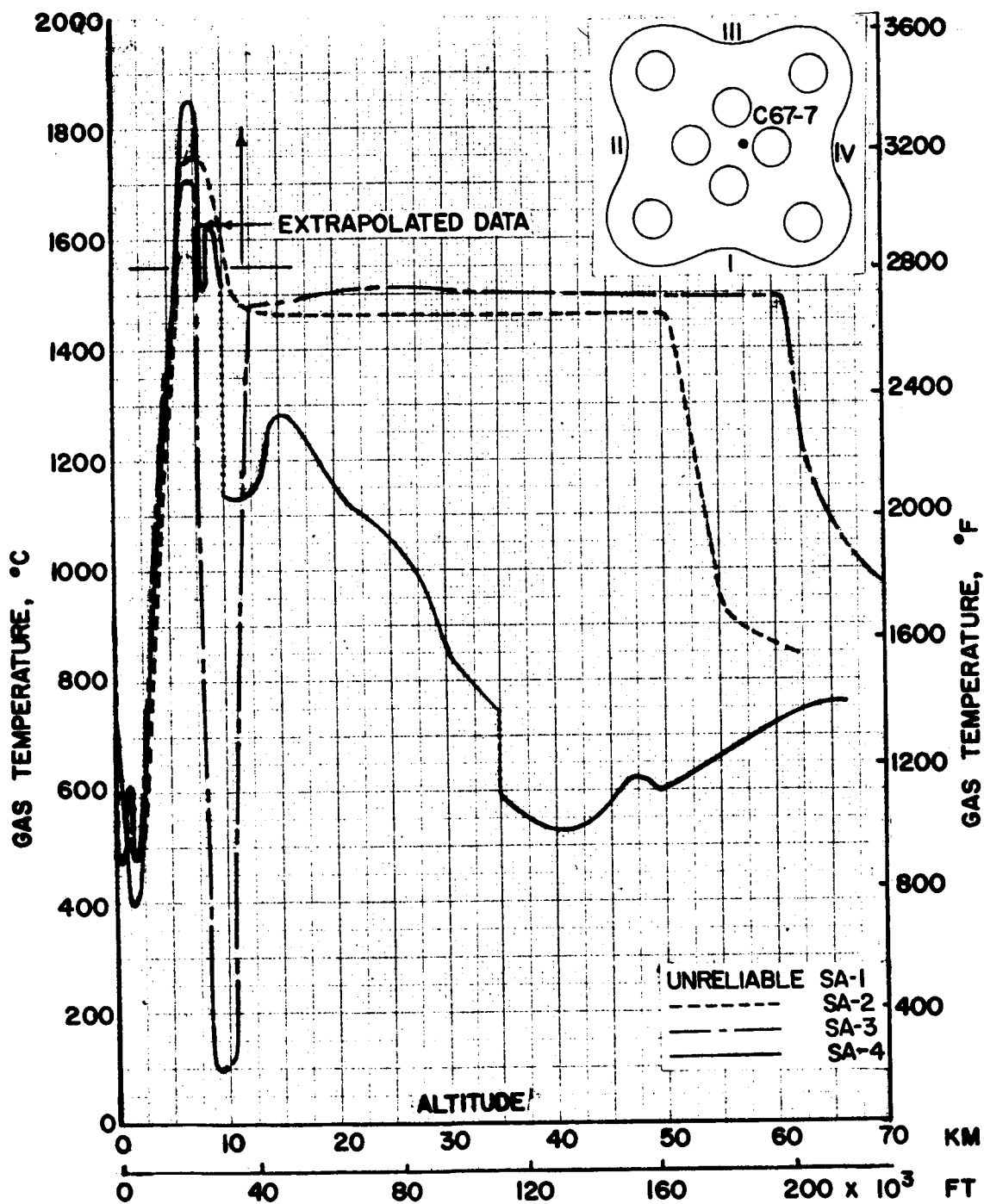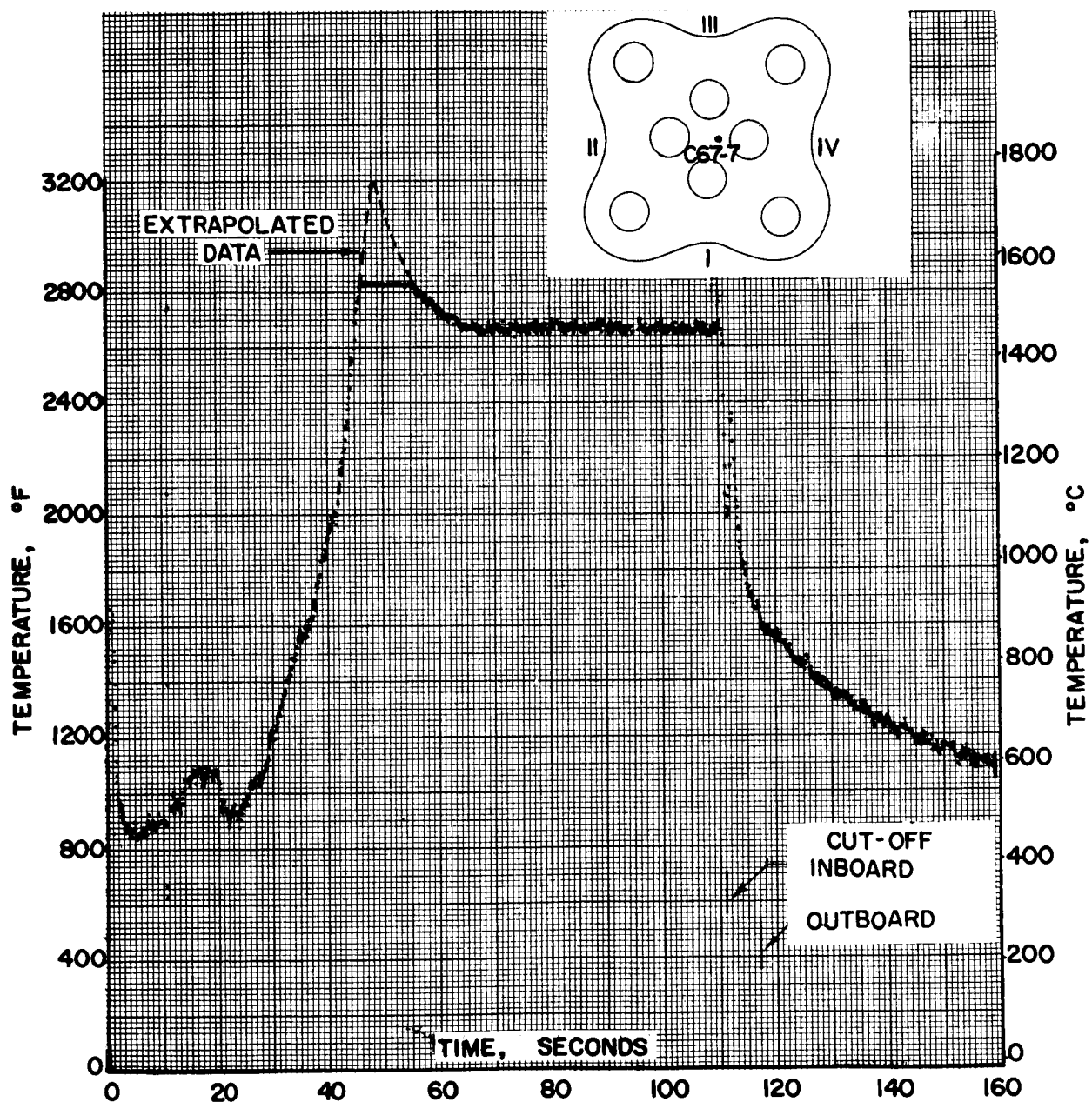FIGURE 45. SATURN SA-2 FLIGHT TELEMETERED DATA

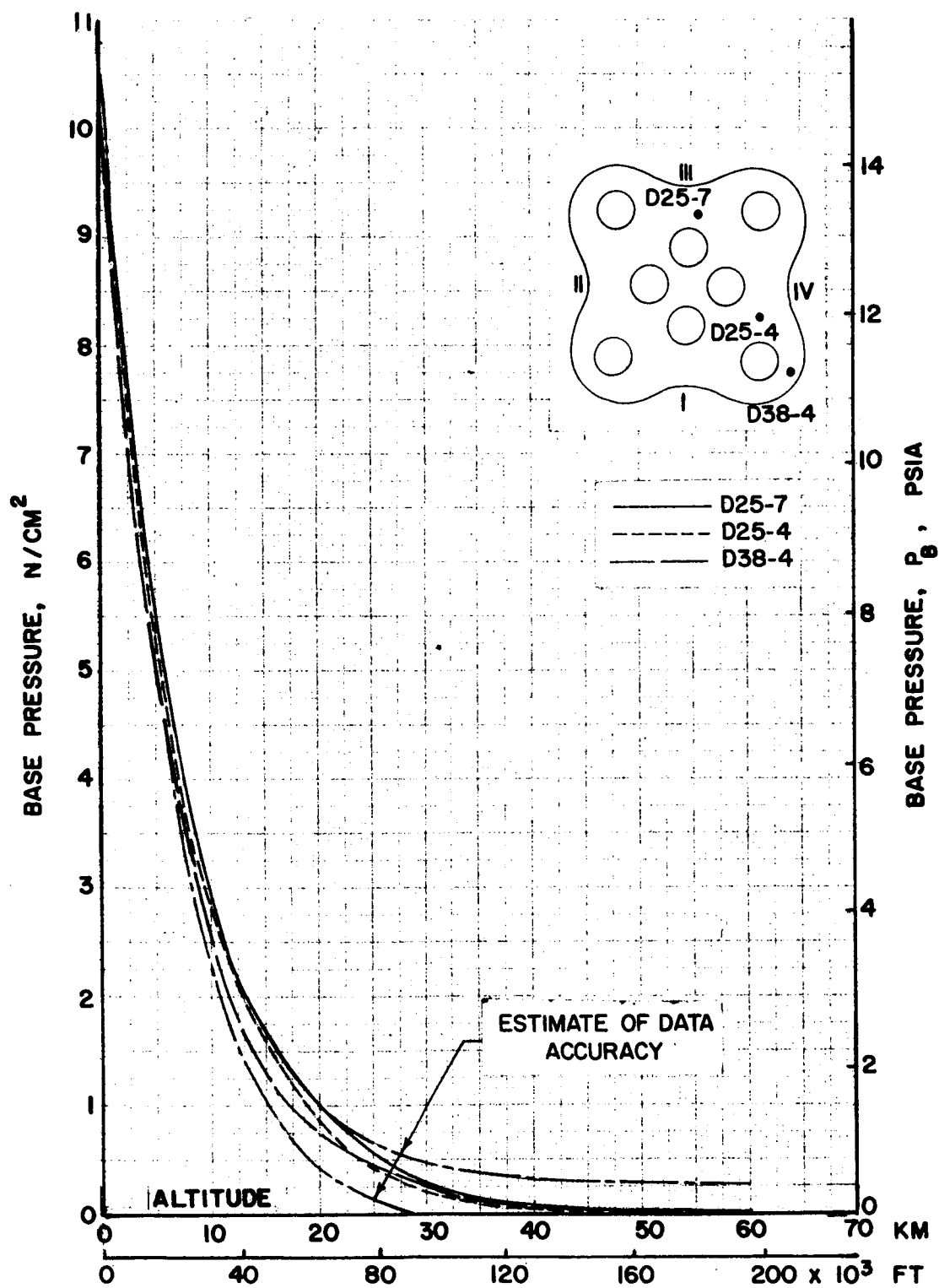FIGURE 46. COMPARISON OF GAS TEMPERATURES ON
BASE OF SATURN I BLOCK I VEHICLES
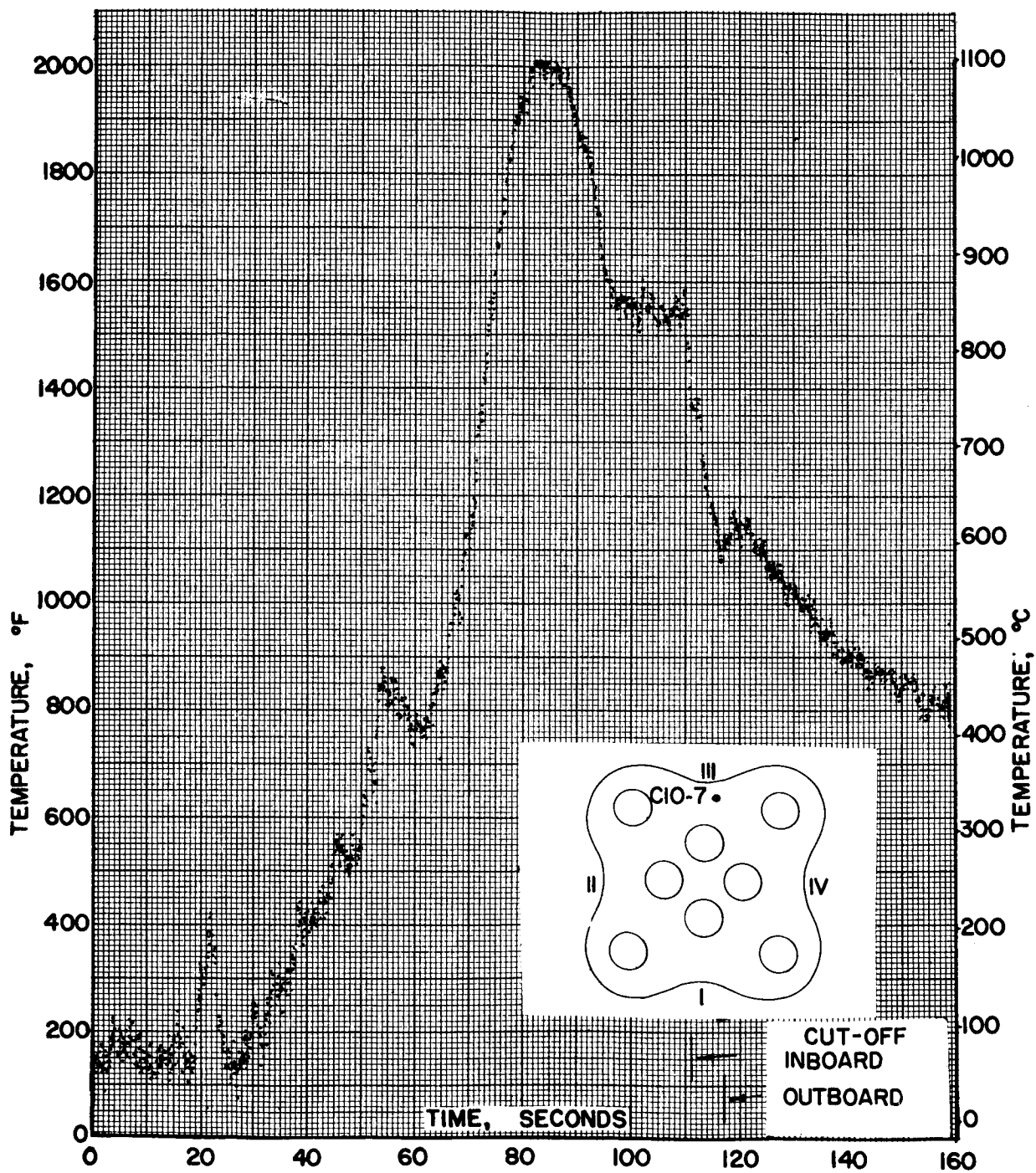
FIGURE 47. SATURN SA-2 FLIGHT TELEMETERED DATA

FIGURE 48. COMPARISON OF GAS TEMPERATURES
ON BASE OF SATURN I BLOCK I VEHICLES

FIGURE 49. SATURN SA-2 FLIGHT TELEMETERED DATA
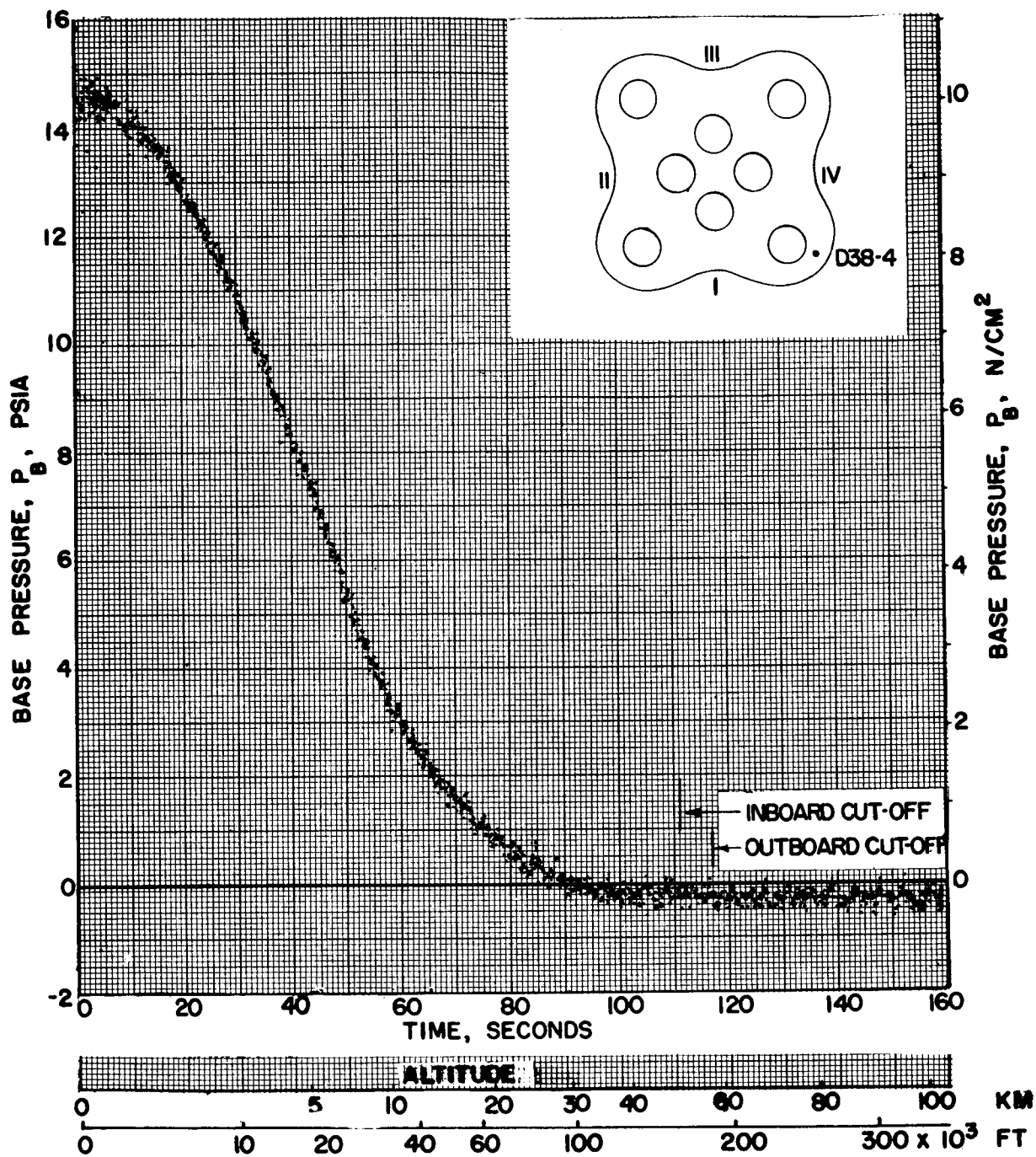
FIGURE 50. COMPARISON OF GAS TEMPERATURE ON
BASE OF SATURN I BLOCK I VEHICLES

FIGURE 51. SATURN SA-2 FLIGHT TELEMETERED DATA

FIGURE 52. COMPARISON OF FLAME SHIELD GAS TEMPERA-
TURE ON BASE OF SATURN I BLOCK I VEHICLES

FIGURE 53. SATURN SA-2 FLIGHT TELEMETERED DATA

FIGURE 54. COMPARISON OF BASE PRESSURES ON
SA-4 FLIGHT

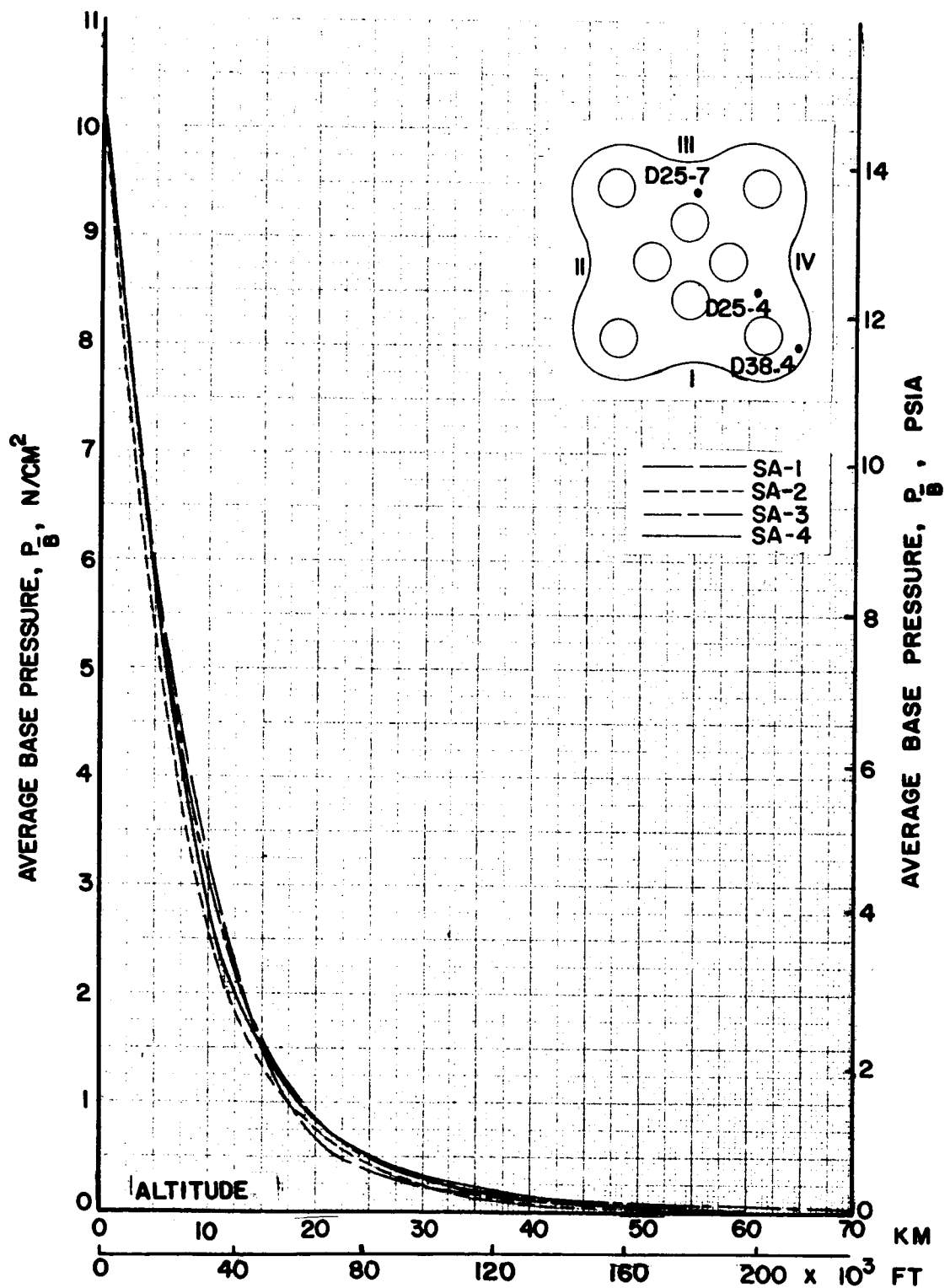FIGURE 55. SATURN SA-2 FLIGHT UNCORRECTED
TELEMETERED DATA

FIGURE 56. COMPARISON OF AVERAGE BASE PRESSURE
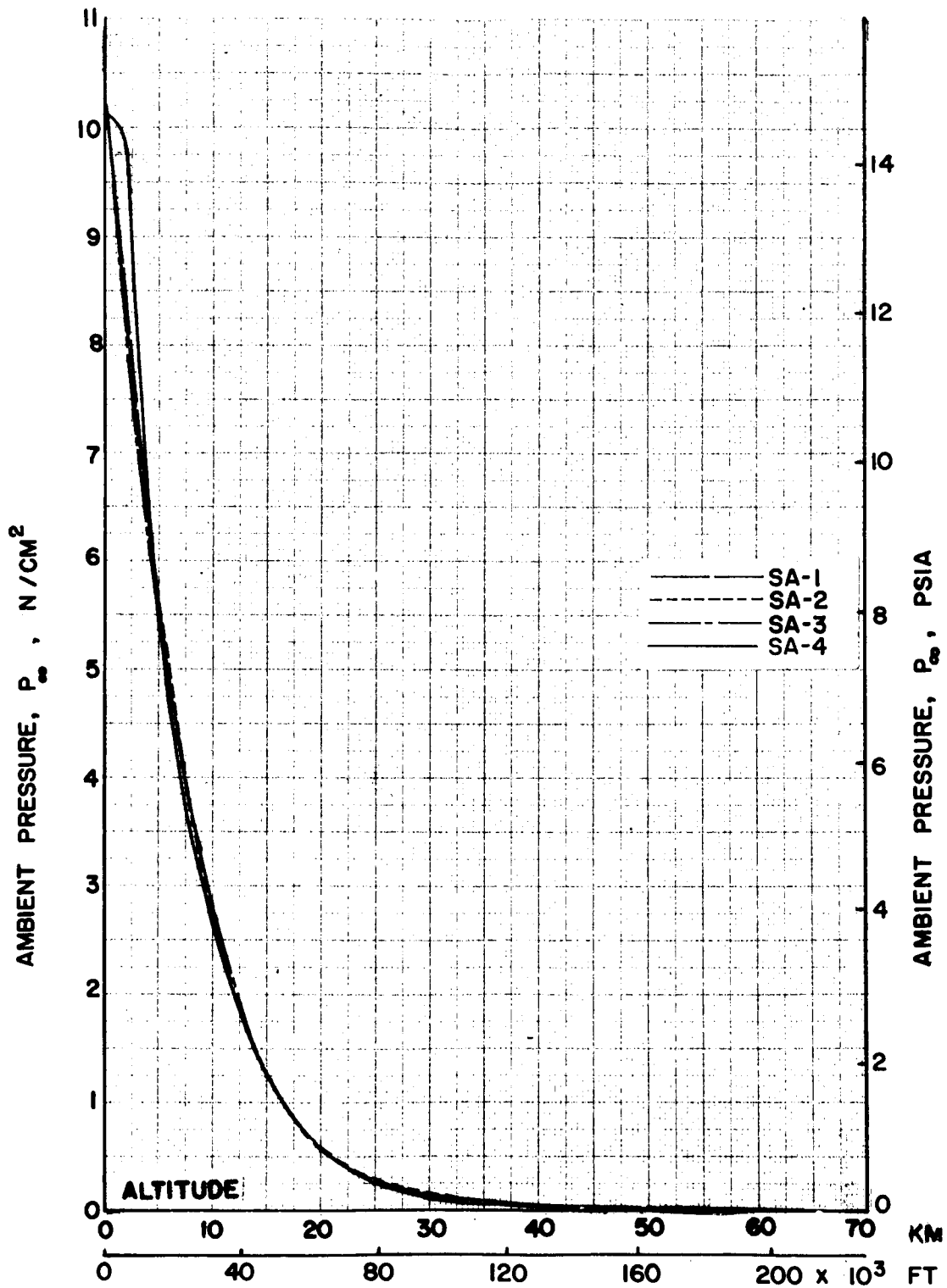ON HEAT SHIELD OF SATURN I BLOCK I VEHICLES

FIGURE 57. COMPARISON OF AMBIENT PRESSURES
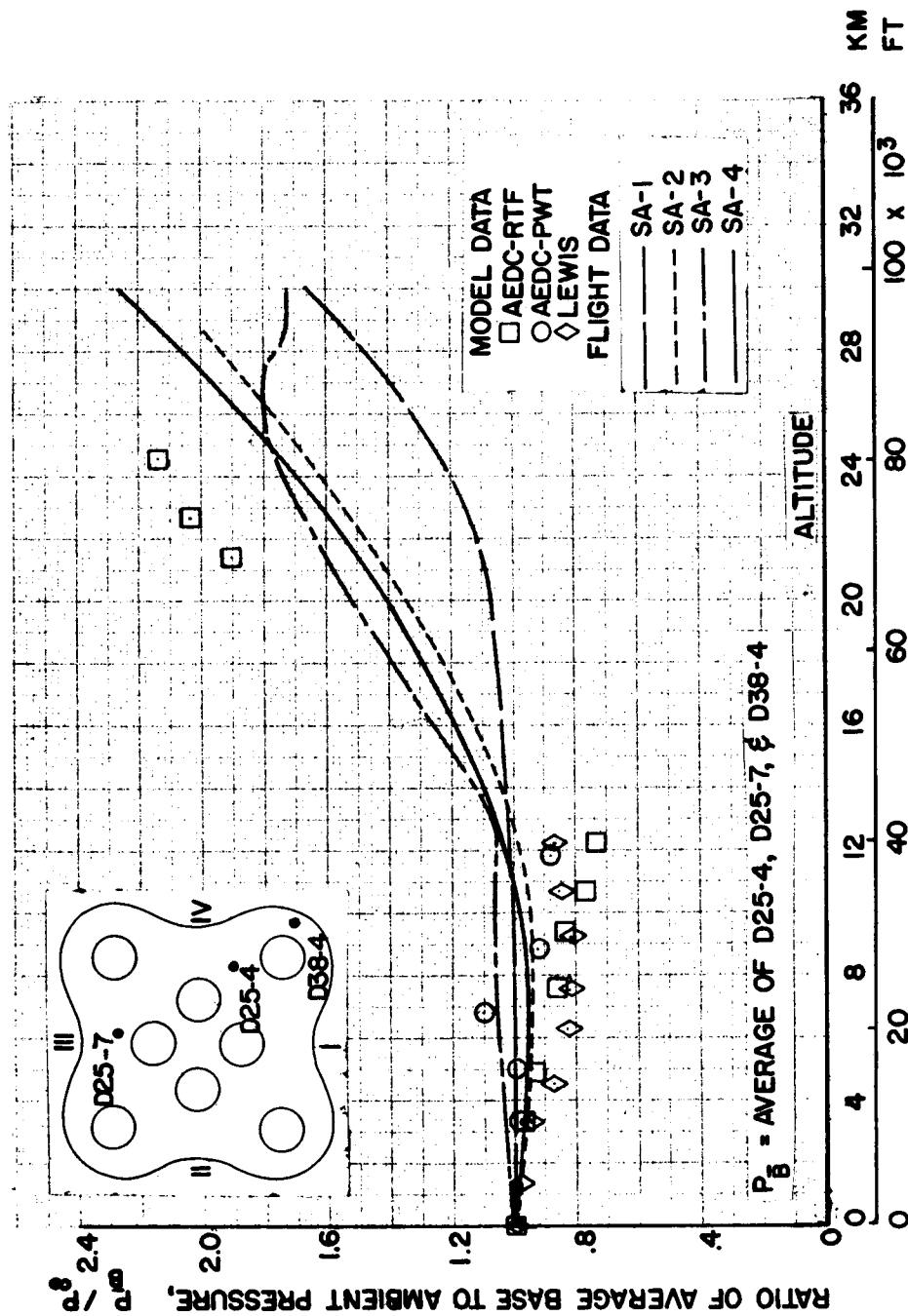FOR THE SATURN I BLOCK I FLIGHTS

104

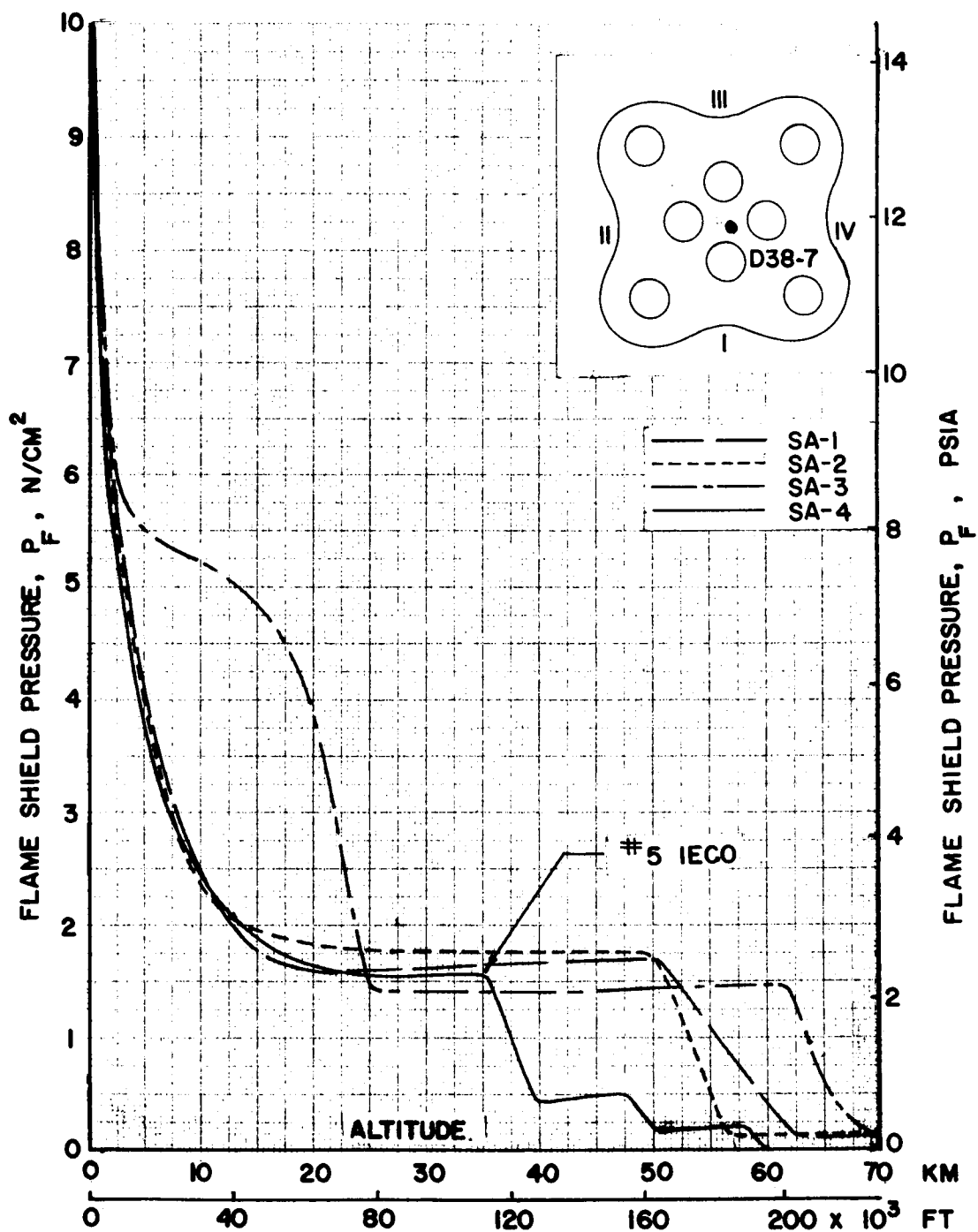FIGURE 58. COMPARISON OF RATIO OF AVERAGE BASE PRESSURE TO AMBIENT PRESSURE ON SATURN I BLOCK I VEHICLES

FIGURE 59. COMPARISON OF FLAME SHIELD PRESSURE
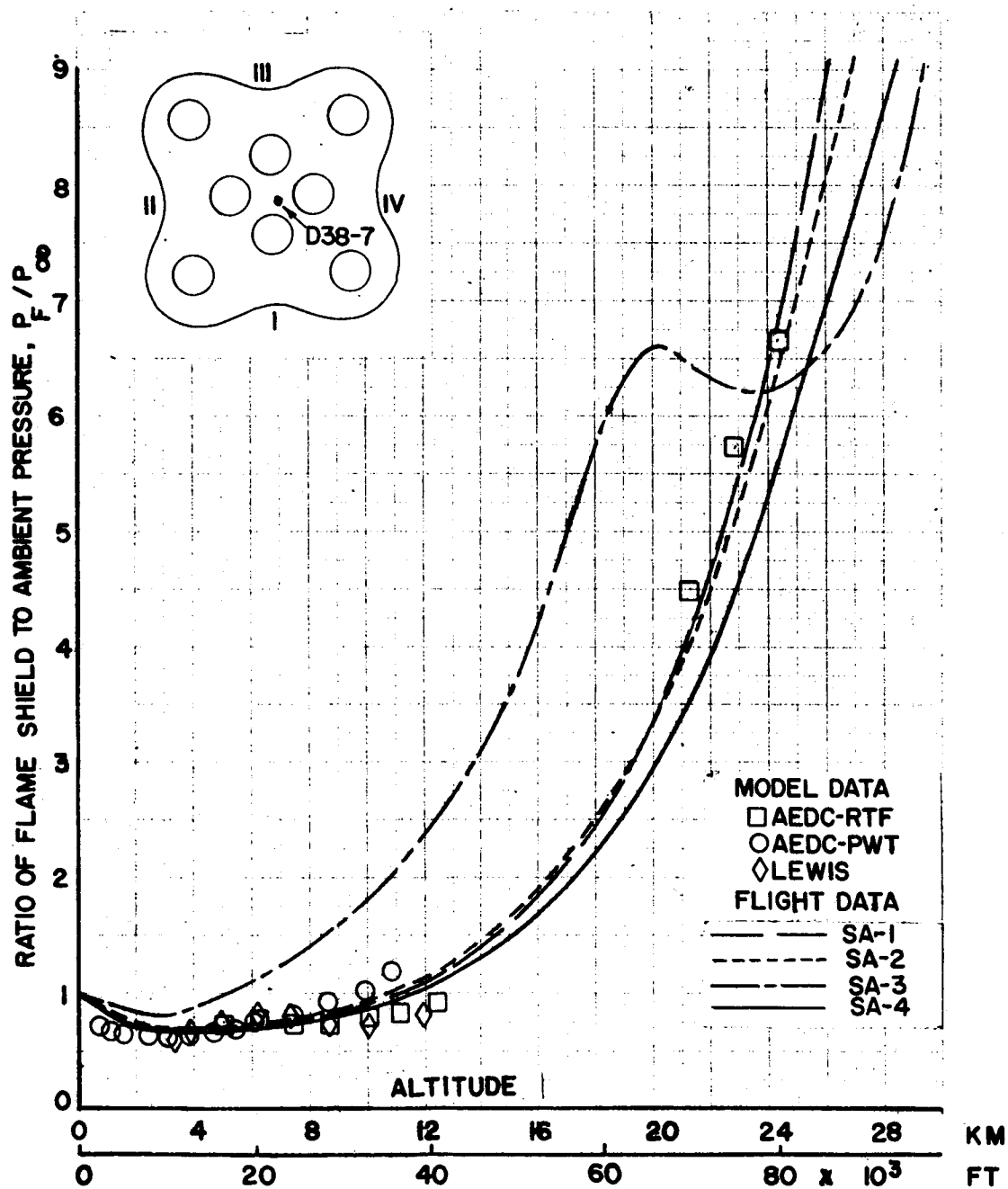ON BASE OF SATURN I BLOCK I VEHICLES

FIGURE 60. COMPARISON OF RATIO OF FLAME SHIELD
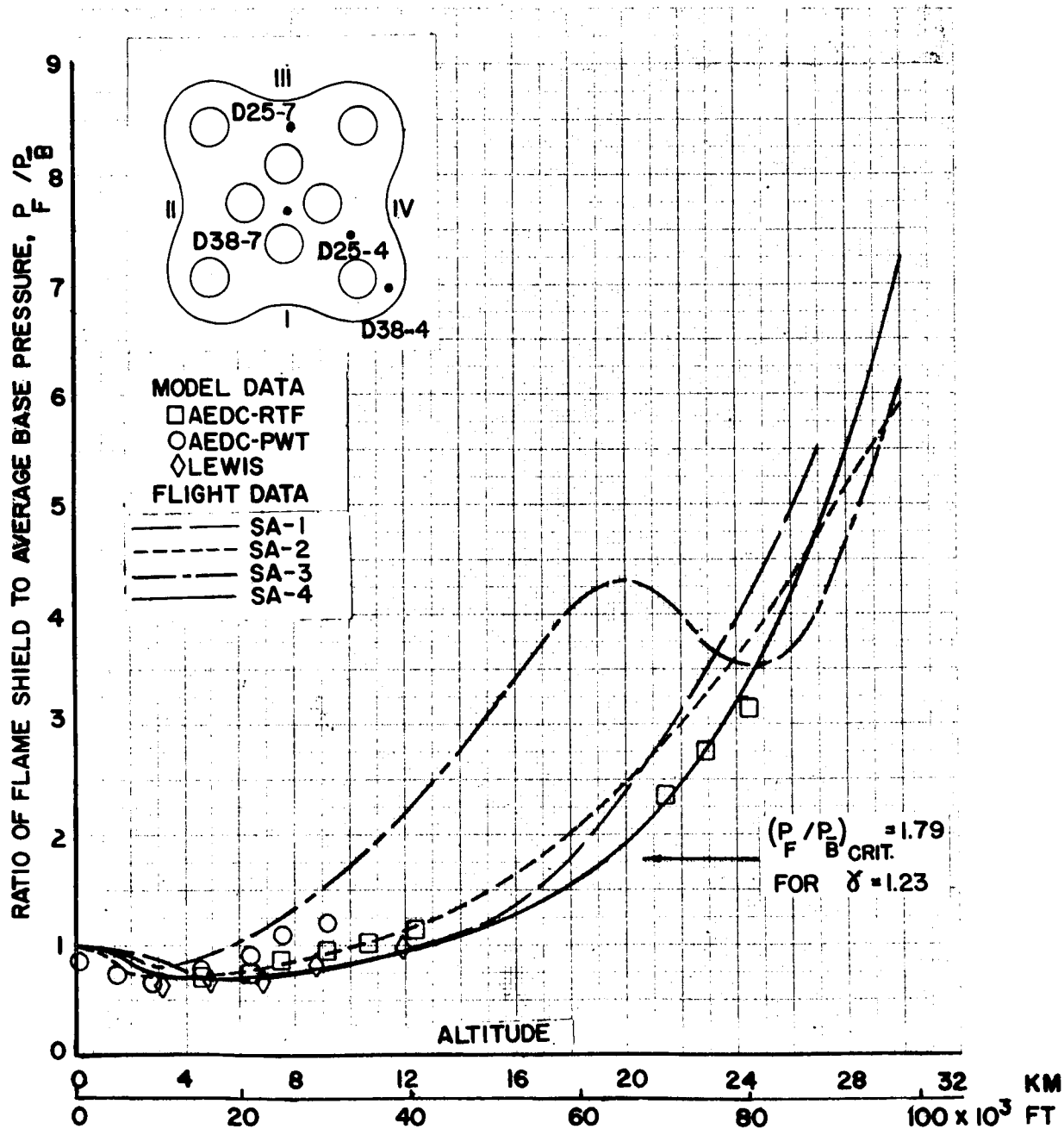TO AMBIENT PRESSURE FOR SATURN I
BLOCK I VEHICLES

FIGURE 61. COMPARISON OF RATIO OF FLAME SHIELD TO AVERAGE BASE PRESSURE FOR SATURN I BLOCK I VEHICLES

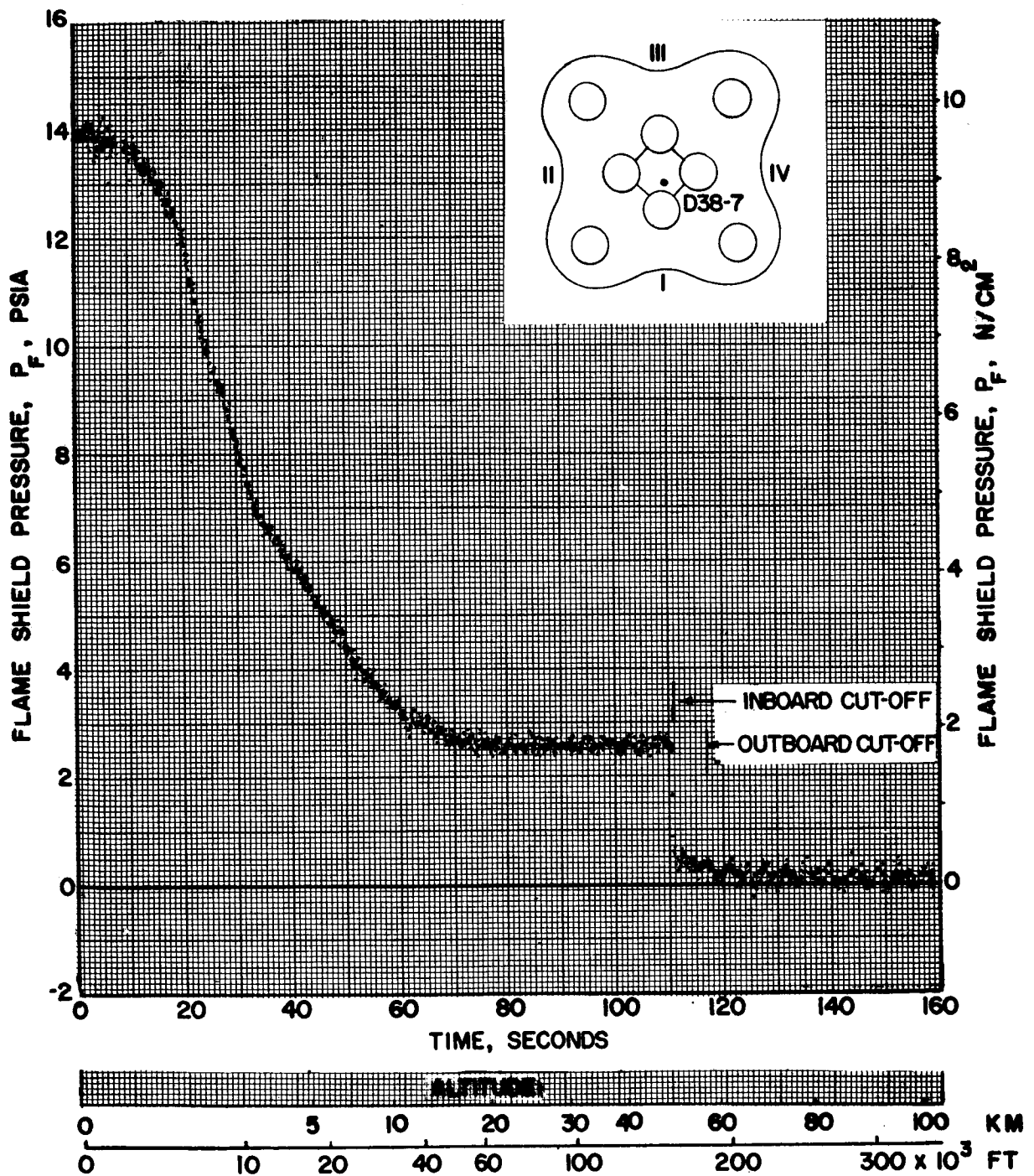FIGURE 62. SATURN SA-2 FLIGHT UNCORRECTED
TELEMETERED DATA

COMPARISON OF RADIATIVE HEATING RATES ON MODEL
AND FLIGHT TESTS ON SATURN I VEHICLES
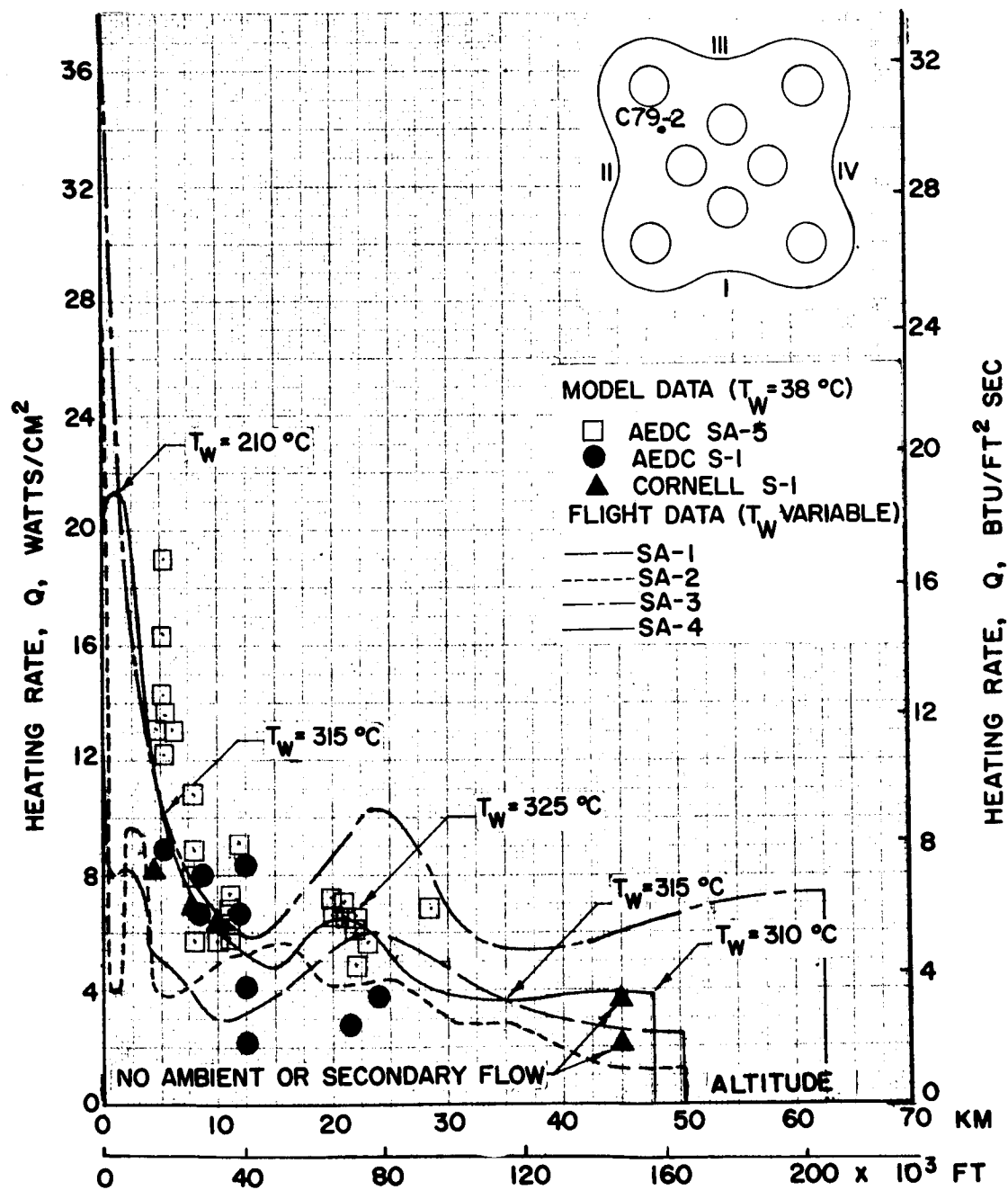

FIGURE 63. COMPARISON OF RADIATIVE HEATING RATES ON
MODEL AND FLIGHT TESTS ON SATURN I VEHICLES
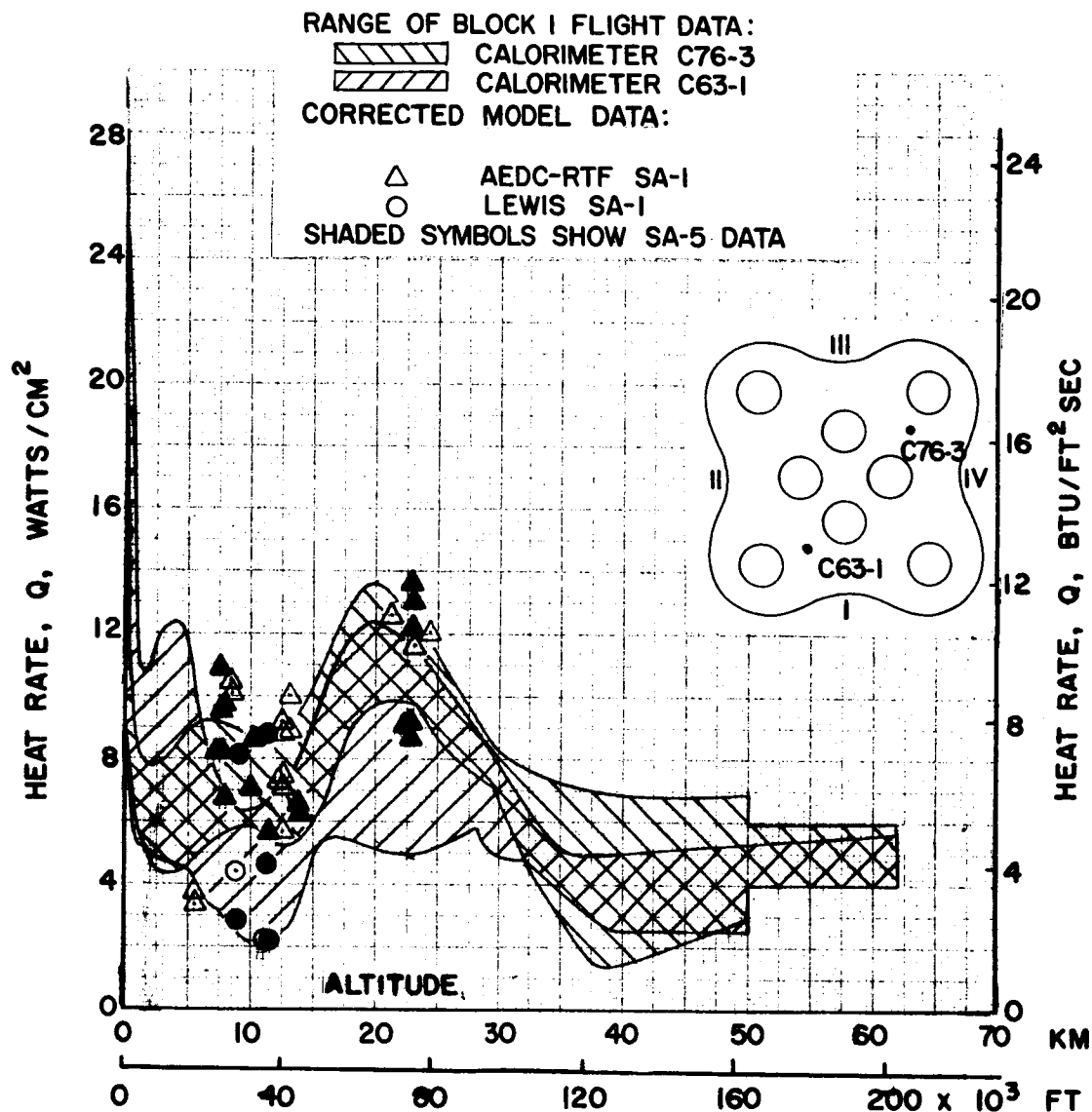
FIGURE 64. COMPARISON OF HEATING RATES FROM
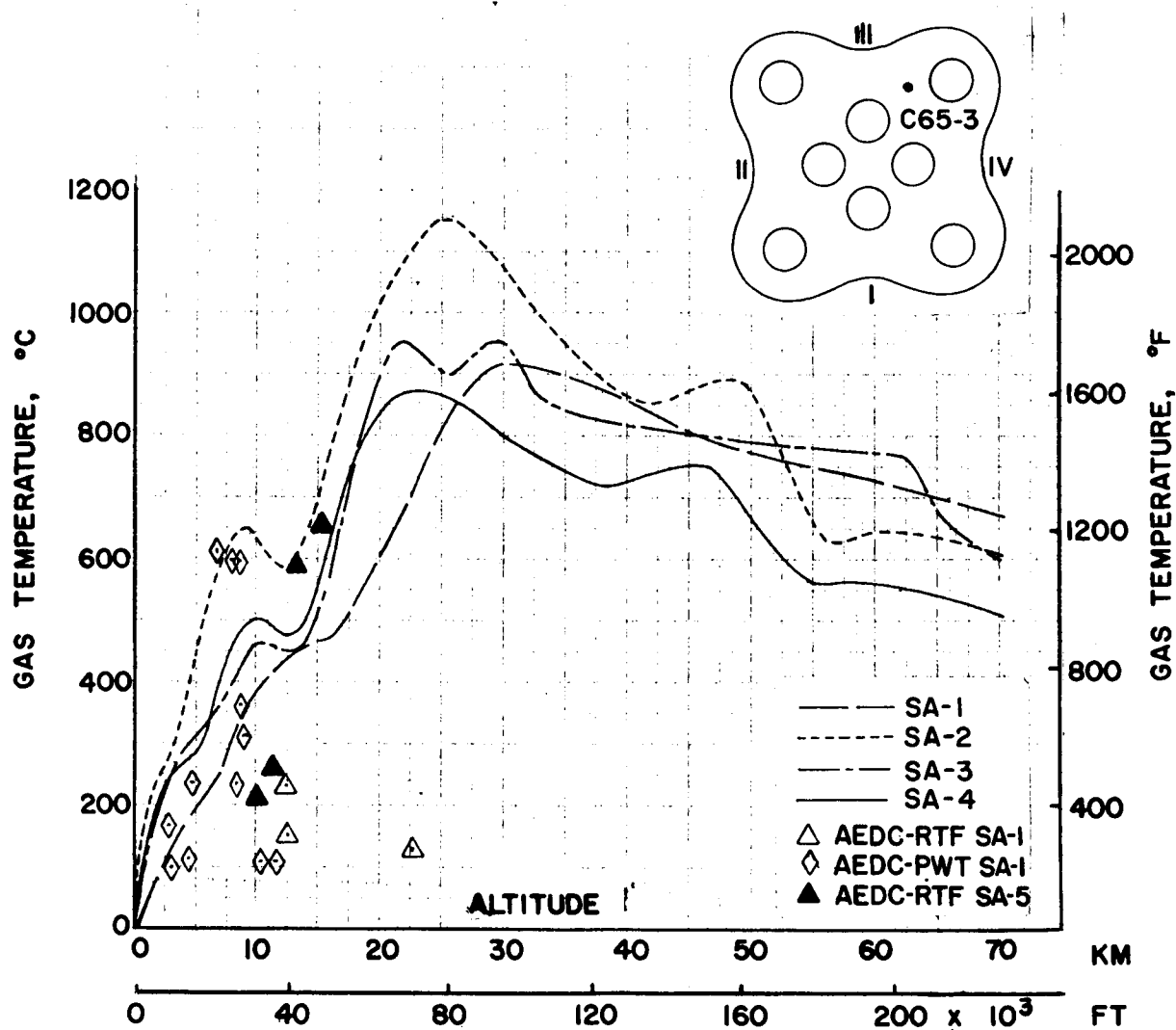SATURN I BLOCK I FLIGHT DATA
WITH MODEL DATA

FIGURE 65. GAS TEMPERATURES FROM SATURN I BLOCK I
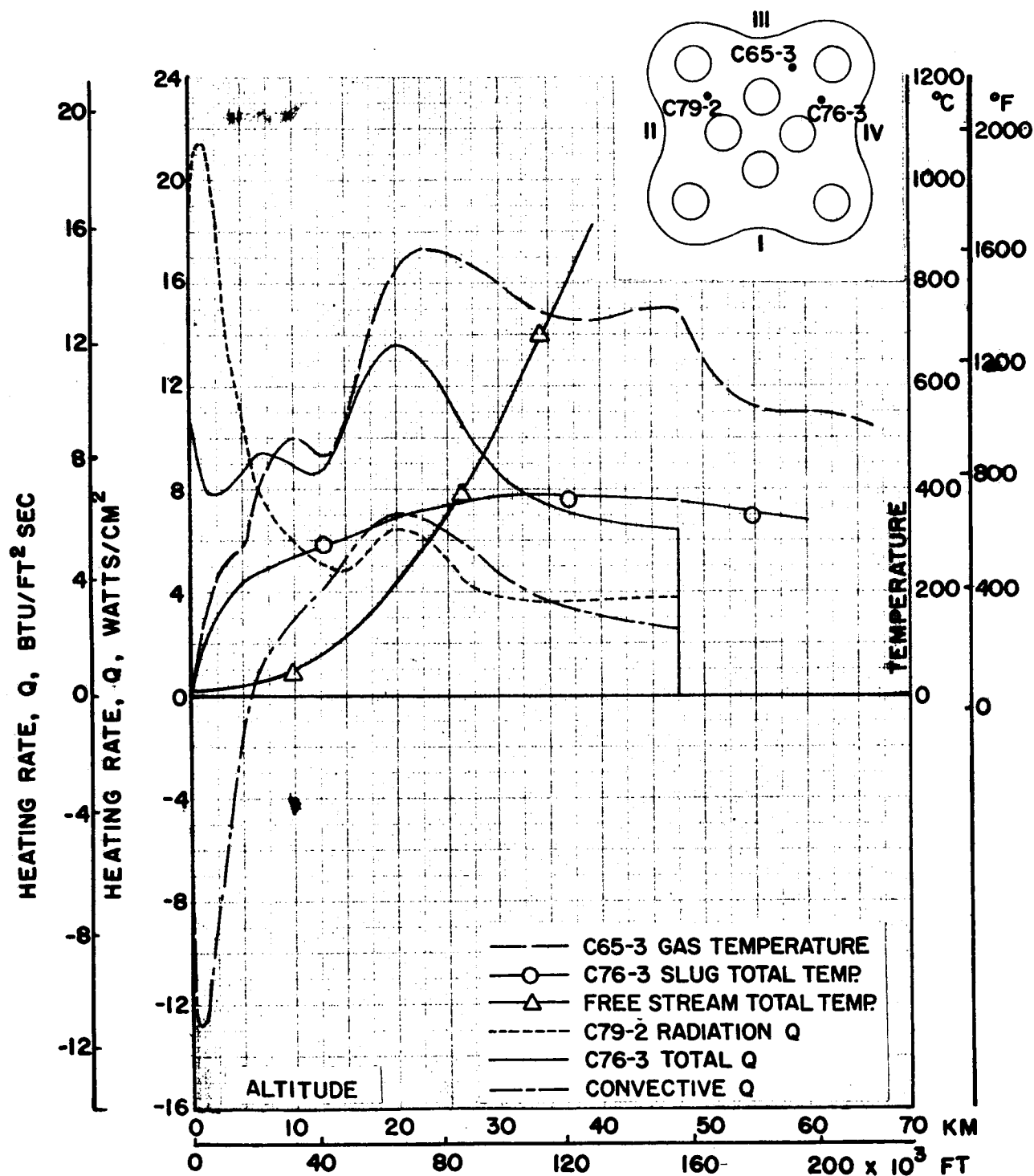FLIGHT DATA COMPARED WITH MODEL DATA

FIGURE 66. MEASUREMENTS USED TO DETERMINE THE
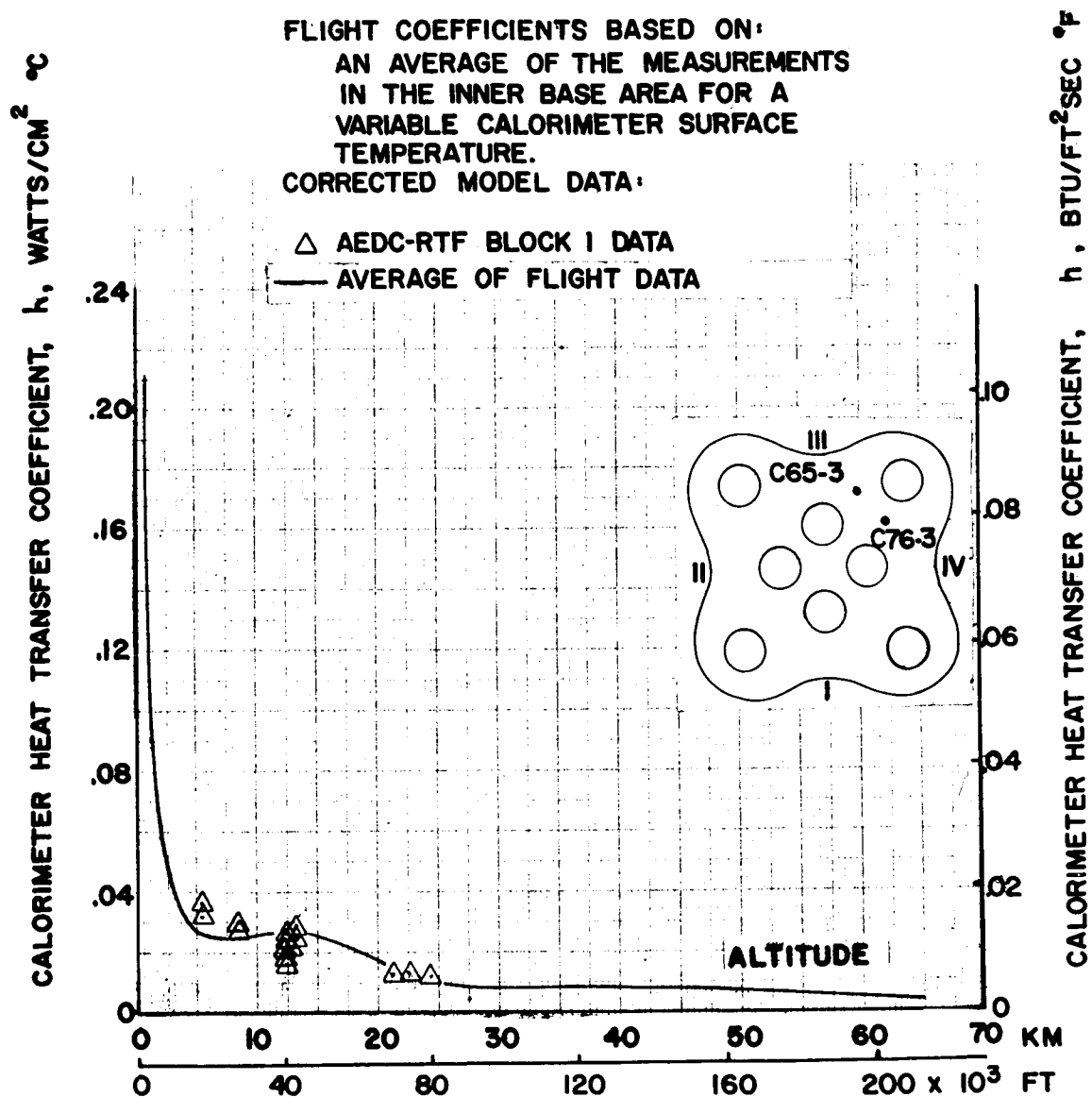BASE HEAT TRANSFER COEFFICIENTS —
TYPICAL DATA SA-4 FLIGHT

FIGURE 67. COMPARISON OF SATURN I BLOCK I FLIGHT HEAT TRANSFER COEFFICIENTS WITH MODEL DATA

APPENDIXES A, B, AND C

LIST OF ILLUSTRATIONS

APPENDIX A

APPENDIX A

SECONDARY CALIBRATION TECHNIQUES

1. Preflight Calibration Technique

Before each flight the total and radiation calorimeters were calibrated using an infrared lamp bank as a heat source. Time-temperature curves were obtained for a range of heating rates which were determined by using a low loss reference calorimeter as a standard. A typical preflight calibration for radiation calorimeter C79-2 is shown in Figure A-1a for the SA-4 flight. The flight time history is shown to indicate the flight temperature range covered by the calibration. The slopes for each constant heating rate were measured and plotted as a function of the slug temperature as shown in Figure A-1b. A cross plot of this figure yields the working plot shown in Figure A-1c. Using the flight data plotted as shown in Figure A-1b for SA-4, the calorimeter heating rate is determined from Figure A-1c.

A comparison of the preflight and inflight calibration methods (section III-c) is shown in Figure A-2 for the radiation measurement C79-2 for both the SA-1 and SA-4 flights. The preflight method yields much higher heating rates for both flights over most of the trajectory than the inflight method. The preflight calibration was performed for the SA-4 with partially simulated conditions of the heat shield. This calibration generally lowered the heating rates, but they were still in excess of those found by the inflight method.

In Figures A-3a, A-3b, and A-3c preflight calibrations curves are given for the total calorimeter measurement C63-1 for the SA-4 flight. The calorimeter was flush-mounted in an M-31 panel simulating the heat shield and contained a nickel slug. Since the total calorimeters exceeded the temperature range by a large amount, the greater part of the heating rate data is based on extrapolations of the calibrations. Since the calibrations are made on the actual flight units, the upper limit of 600°F (315°C) on the slug temperature is maintained to prevent any possible damage to the units. The lower temperature data are not obtained because of the slow heating of the calibration lamps which would result in a transient heating rate in this region.

A comparison of the preflight and inflight calibrations is shown in Figure A-4 for total calorimeter measurement C63-1 for both the SA-1 and SA-4 flights. The comparison is found to be much better for the total calorimeters than for the radiation calorimeters. The effects of simulating the heat shield cannot be

obtained from Figure A-4 by comparing SA-1 flight with SA-4, since the SA-1 had an X-258 heat shield and used a copper slug calorimeter and for the SA-4 flight the calorimeter had a nickel slug and was flush mounted in an M-31 heat shield.

Reference 8 shows that the copper calorimeters had much higher conduction losses than the nickle calorimeters. In Figure A-5 the conduction loss factor as defined in the figure for a copper and nickel flight calorimeter is compared. At low slug temperatures, a 40 percent reduction in the loss factor is obtained with the nickel slug; this increases to approximately 50 percent at 600°F (315°C). This sizable loss reduction prompted the change in all the heat shield total calorimeters to nickel starting with the SA-4 flight.

2. Post Flight Calibration Technique

An additional test technique has proved useful in evaluating the calorimeter base heating rates. Reference 34 gives the results of the postflight calibration procedure for the SA-4 flight.

The postflight calibration method (Fig. A-6) takes the flight temperature-time curve of a particular calorimeter and with the aid of a "Data-Trak" controller connected to an infrared lamp bank and a duplicate flight calorimeter mounted in a heat shield panel, a programmed power setting for the lamp bank is determined which will reproduce the flight-time-temperature curve from the duplicate calorimeter. The programmed "Data-Trak" is then rerun using the above determined power setting with a water cooled "asymptotic" standard calorimeter installed under the lamp bank. The output of the calorimeter can be converted directly to a heating rate and plotted with an automatic x-y plotter as shown in Figure A-7. The preflight and inflight calibration methods can then be compared with this technique as shown in Figure A-7. Reasonable comparisons have been obtained by this procedure, and many postflight evaluation problems have been investigated and solved by employing this test procedure.

FIGURE A-1a. SA-4 PREFLIGHT CALIBRATION OF RADIATION
CALORIMETER C79-2

119
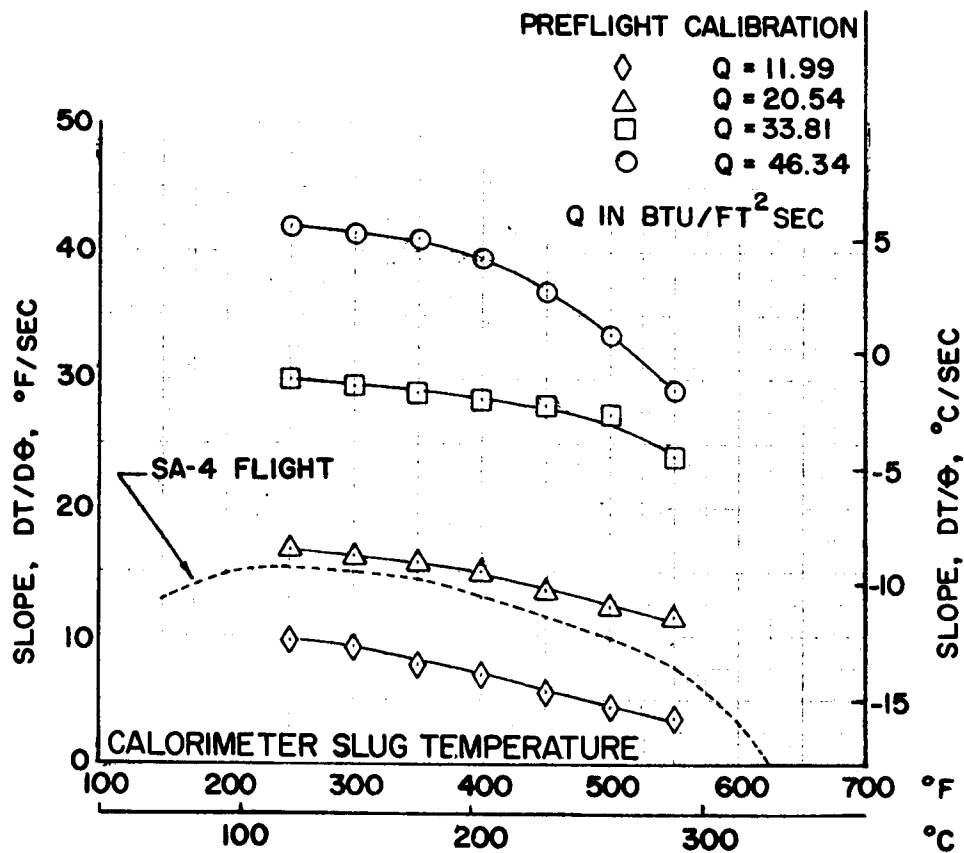
FIGURE A-1b. SA-4 PREFLIGHT CALIBRATION OF
RADIATION CALORIMETER C79-2
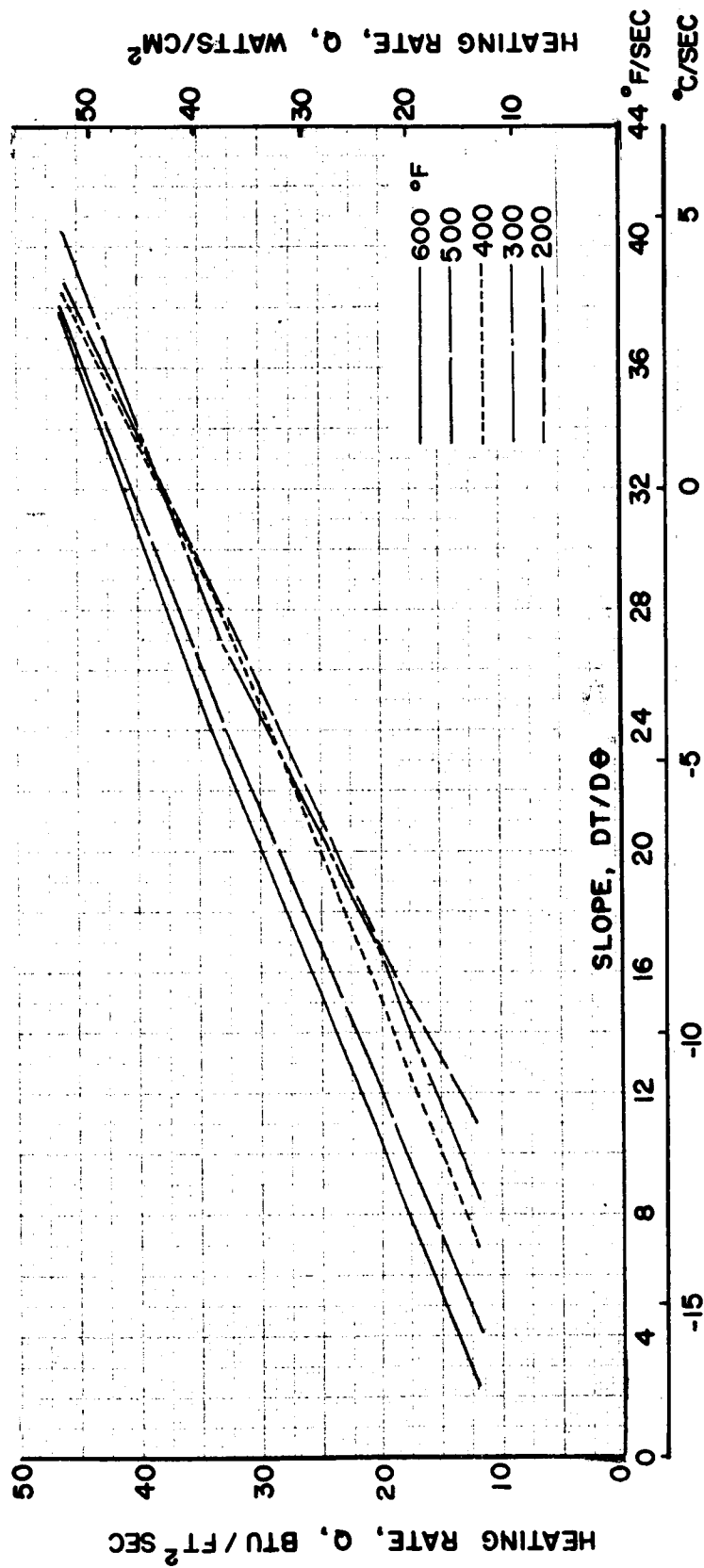
FIGURE A-1c. SA-4 PREFLIGHT CALIBRATION CURVE FOR RADIATION CALORIMETER C79-2

121

FIGURE A-2. COMPARISON OF PREFLIGHT AND
INFLIGHT CALIBRATION METHODS
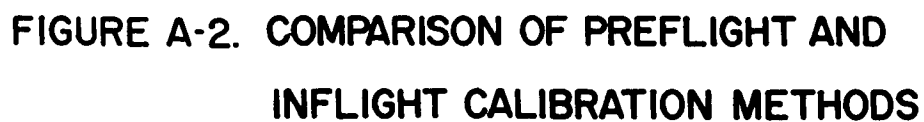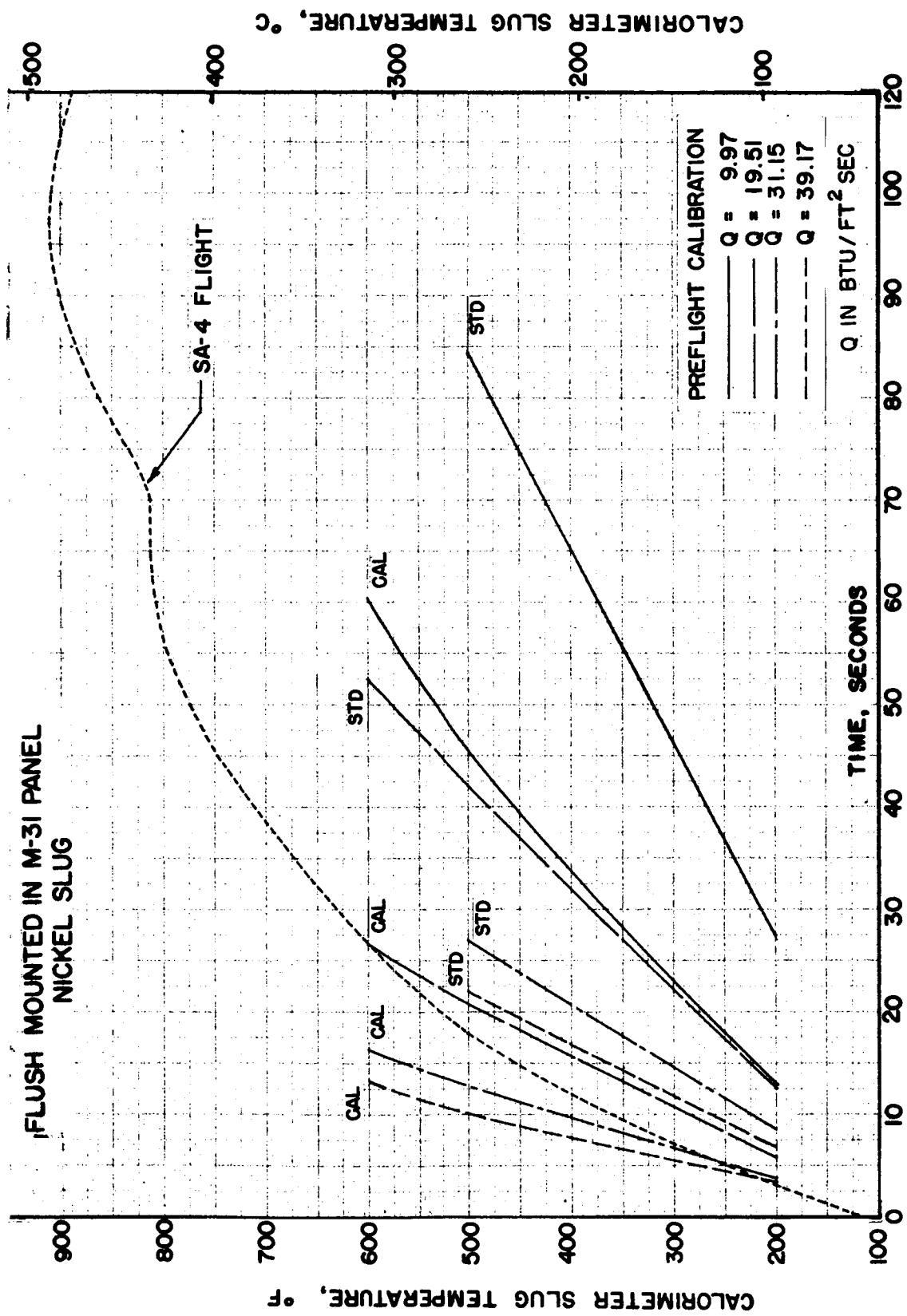
FIGURE A-3a. SA-4 PREFLIGHT CALIBRATION OF TOTAL CALORIMETER C63-1

FLUSH MOUNTED IN M-31 PANEL
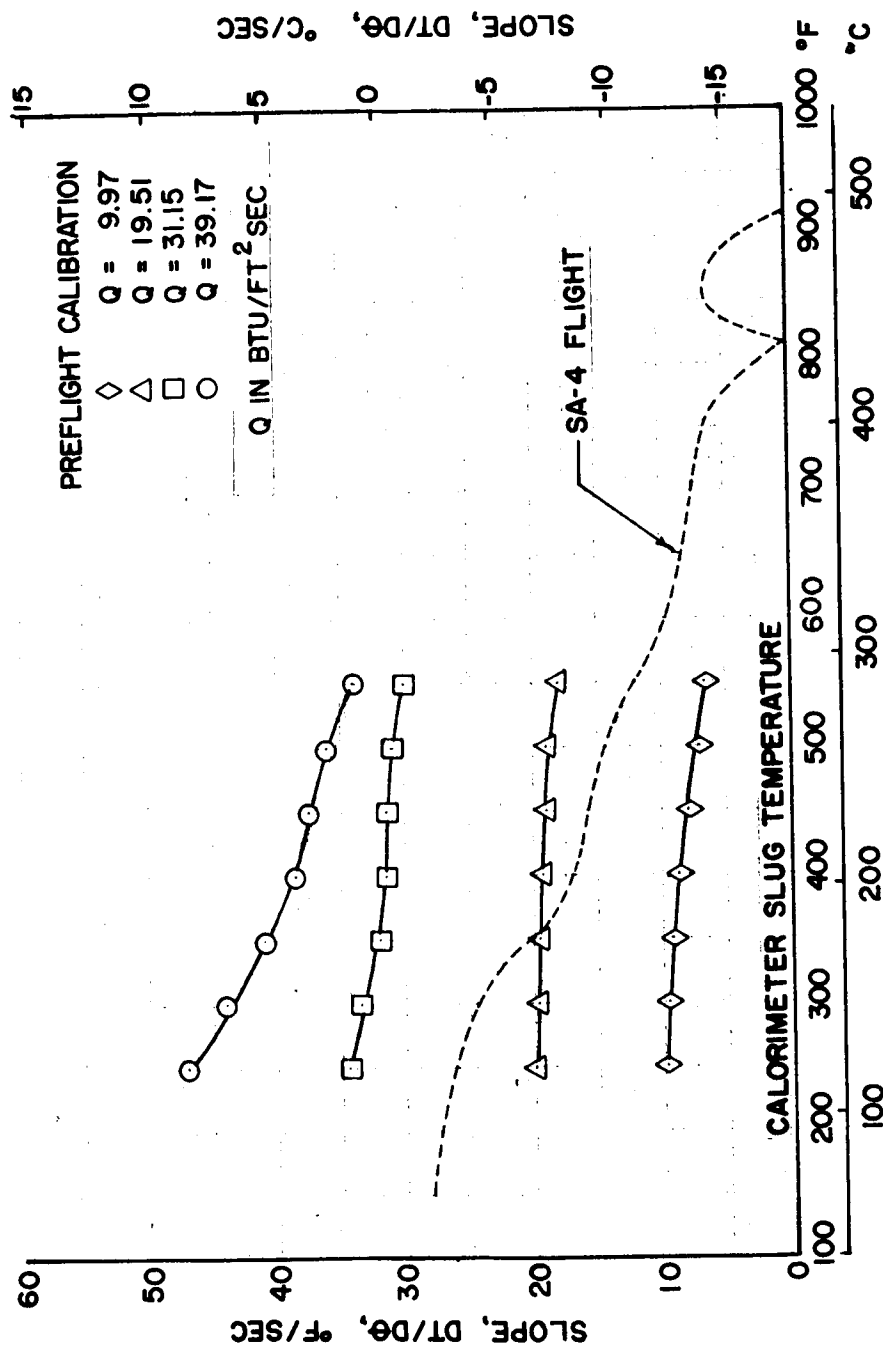
FIGURE A-3b. SA-4 PREFLIGHT CALIBRATION OF TOTAL CALORIMETER C63-I
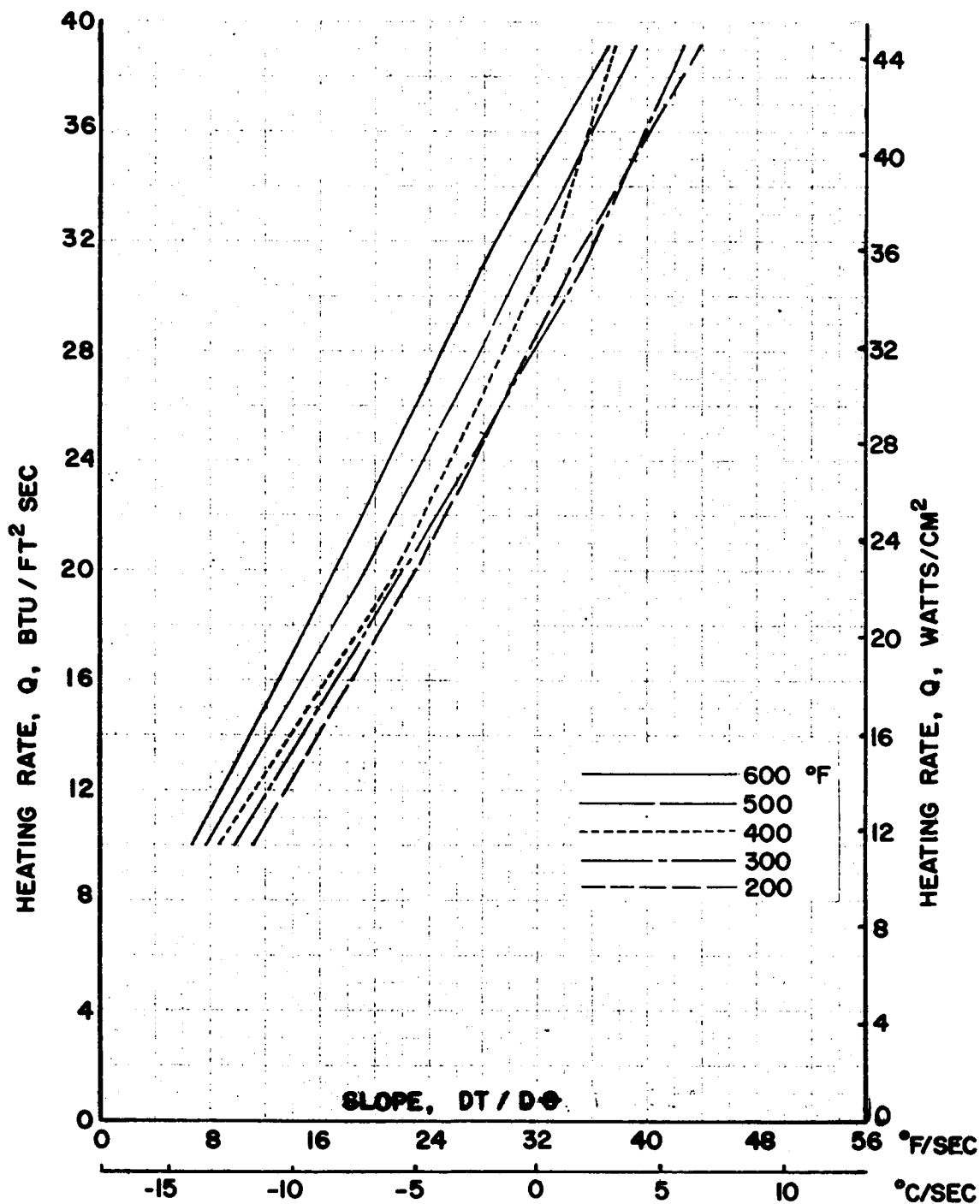
FIGURE A-3c. SA-4 PREFLIGHT CALIBRATION CURVE
FOR TOTAL CALORIMETER C63-1
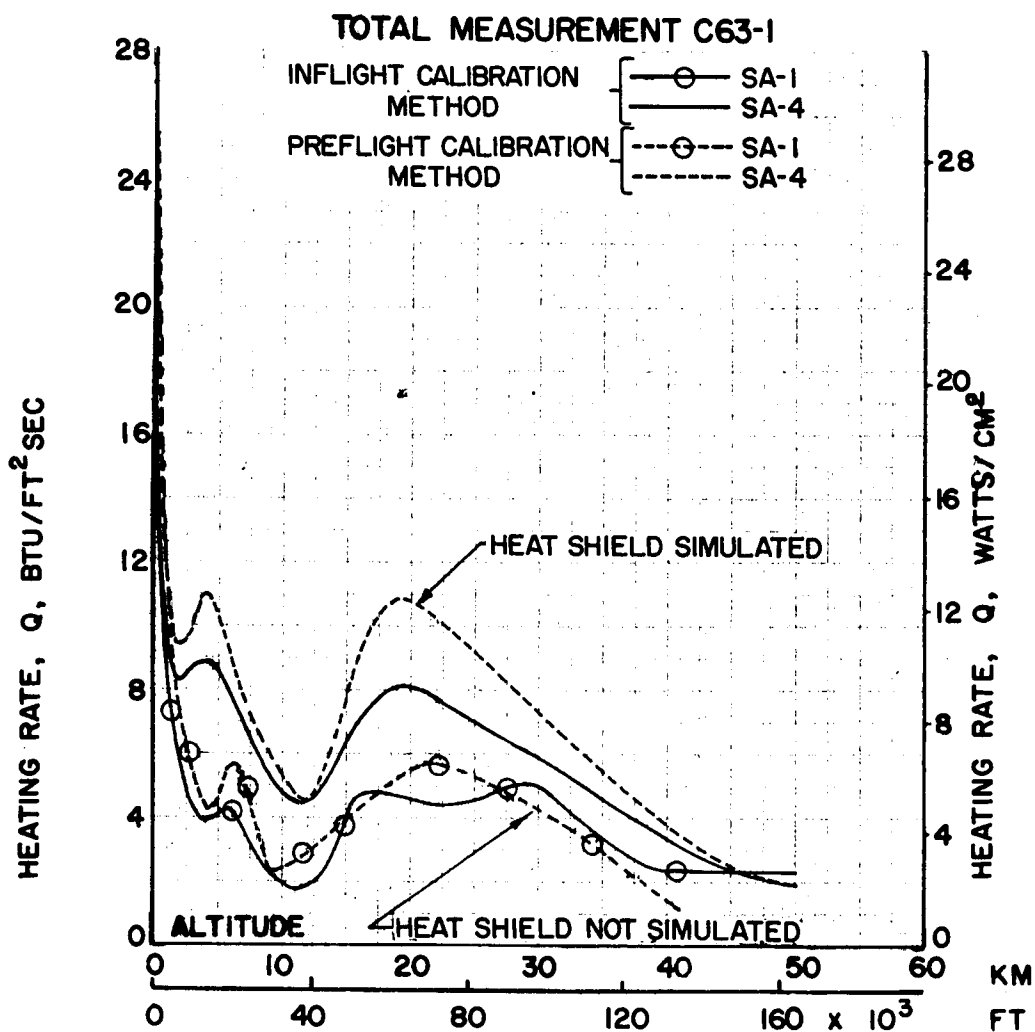
FIGURE A-4. COMPARISON OF PREFLIGHT AND INFLIGHT
CALIBRATION METHODS

M-31 FLIGHT HEAT SHIELD SIMULATED

TYPE SLUG	C_p	ρ	t	$C_p \rho t$
	BTU/lb•F	lb/ft³	in.	BTU/ft²•F
NICKEL	.12	550	.12	.660
COPPER	.096	555	.12	.639

$$K = \frac{\dot{Q}_{ref.}}{(C_p \rho t) \; dT/d\theta}$$

WHERE $\dot{Q}_{ref.}$ = 9.0 BTU/ft² sec (FROM .4" THICK COPPER STD.)

$\dfrac{dT}{d\theta}$ = SLOPE OF CALORIMETER TIME-TEMP. CURVE FOR $\dot{Q}_{ref.}$
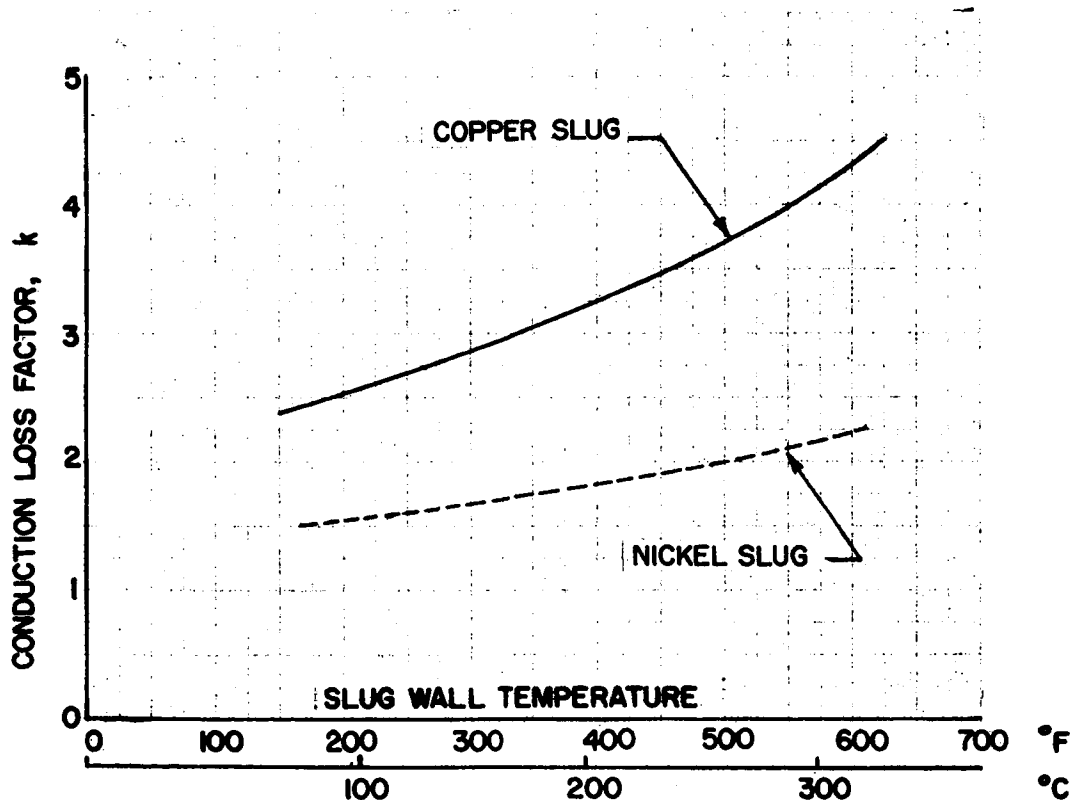
FIGURE A-5. COMPARISON OF CONDUCTION LOSS FACTOR
FOR COPPER AND NICKEL TOTAL FLIGHT
CALORIMETERS

STEP I

DETERMINE LAMP BANK POWER SETTING TO PRODUCE FLIGHT TIME-TEMPERATURE CURVE FROM THE DUPLICATE CALORIMETER
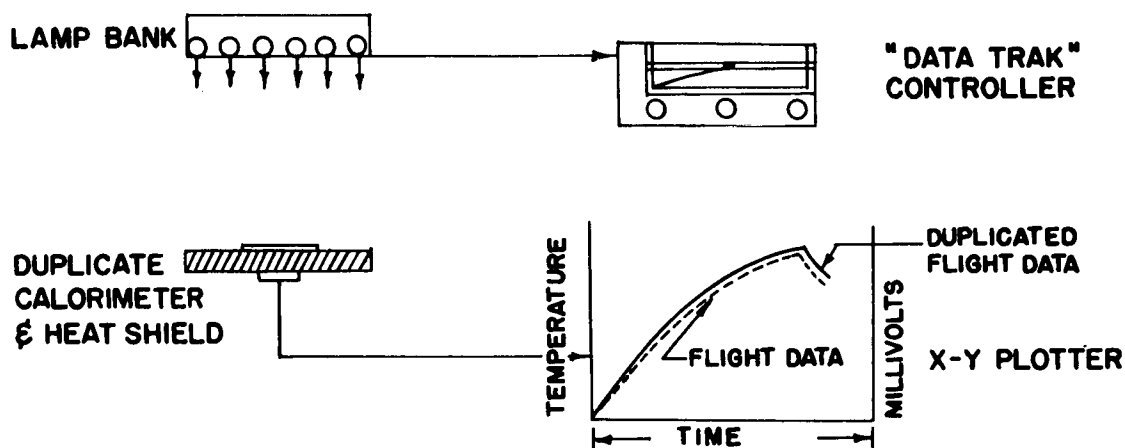
STEP II

USING THE POWER SETTING ESTABLISHED IN STEP I THE HEATING RATE IS MEASURED DIRECTLY WITH AN ASYMPTOTIC WATER COOLED SENSOR
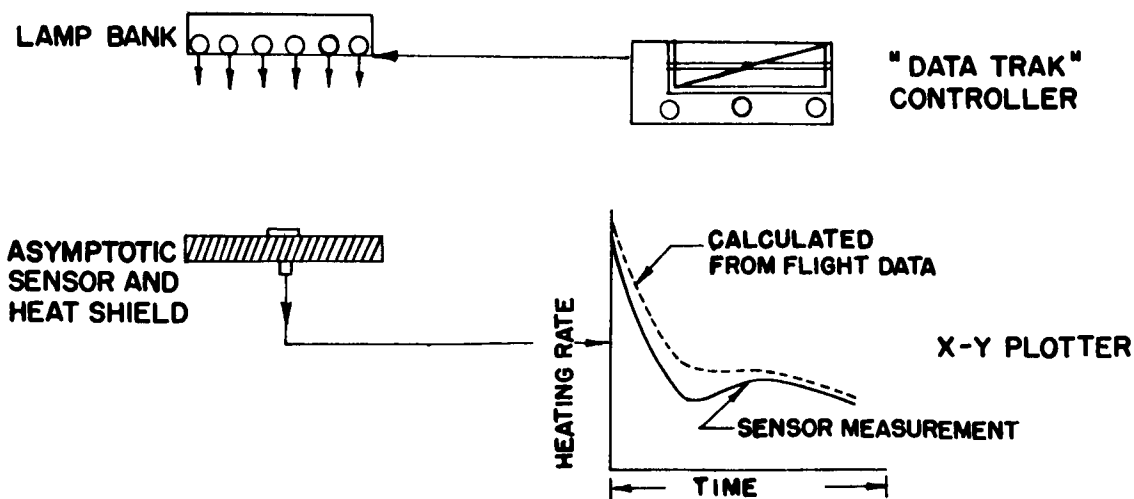
FIGURE A-6. POSTFLIGHT CALIBRATION TECHNIQUE
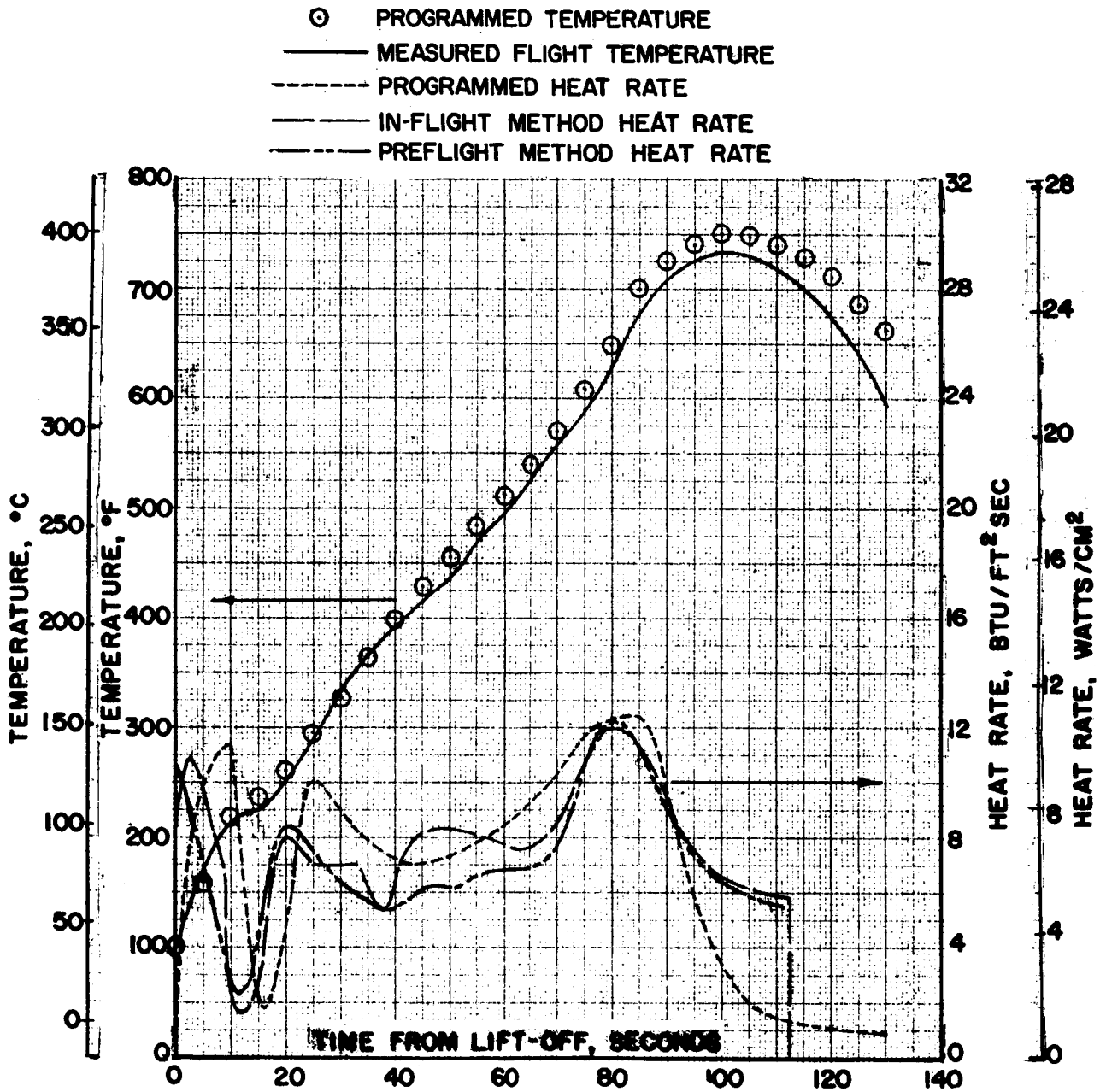
FIGURE A-7. POSTFLIGHT CALIBRATION METHOD COMPARED WITH PREFLIGHT AND INFLIGHT METHODS

LIST OF ILLUSTRATIONS

APPENDIX B

APPENDIX B

RADIATION CALORIMETER LOSSES

Additional information on the losses found in the radiation calorimeters used for the Block I vehicles is included here.

Figure B-1 indicates the effects of the calorimeter view angle on calibration factor K (calorimeter heating rate ratioed to a low loss 180-degree view angle reference calorimeter) with distance from a radiation source. The three different view angle calorimeters that were flown are presented. The 150-degree calorimeter indicated the lowest calibration factor and was the least influenced by the distance of the normal radiation source. As the view angle decreased, the calibration factor increased and changed more rapidly with the location of the radiation source.

The 114-degree view angle calorimeter used on the SA-1 flight was tested in Reference 15 for the effects of a variable angle of incidence.

Figure B-2 indicates that there is only a nominal change in the calibration factor between the normal angle of incidence and 30 degrees. For the 60-degree angle of incidence, the initial level is seen to be much larger, and a sharp rise in the calibration factor is found with increasing distance from the source. Since the distance and angle of incidence of the jet plume radiation varies with altitude, an evaluation of the correction for the flight conditions cannot be made.

The window transmissivity of the flight calorimeters are known to have some effect on the calorimeter output as previously discussed. In Figure B-3 the percent transmission through the sapphire window is shown as a function of the angle of incidence of the radiation source. The curve is shown for the average value of the refractive index (r) in the 2-3 micron spectral range where radiation from the rocket exhaust is the most intense. For this range the absorption coefficient (d) is taken as zero based on information found in Reference 13. The calorimeter view angle is shown for each flight and indicates that for the SA-1 flight, if the radiation came from an angle of incidence equal to the view angle, the transmission would be 80 percent; whereas, the SA-3 and SA-4 flights would be 57 percent. This rapid decrease in transmission offsets partially the effects of the increased view angle of the later flights. It is not possible to determine the error involved since the incidence angle and radiation intensity vary with altitude; but since the plume radiation is not great at the higher altitudes (where the angle of incidence would be the highest due to plume expansion) the absolute heating rate error is expected to be small.

DATA FROM REFERENCE 19

A_C = CALORIMETER AREA OF VIEW AT A UNIT DISTANCE

A_{SA-1} = CALORIMETER AREA OF VIEW AT A UNIT DISTANCE FOR SA-1

$$\dot{Q}_{REF} = K\left[\rho\, C_p\, D\left(\frac{DT}{Dt}\right)\right]$$

$$K = \frac{\dot{Q}_{REF}}{\dot{Q}_{CAL}}$$

CALIBRATION FACTOR BASED ON 180° VIEW ANGLE REFERENCE CALORIMETER, K

β = 114°
A_C/A_{SA-1} = 1.00

CALORIMETER
○ SA-3,-4
△ SA-2
□ SA-1

β = 130°
A_C/A_{SA-1} = 1.94

β = 150°
A_C/A_{SA-1} = 5.87

DISTANCE FROM RADIANT SOURCE, INCHES
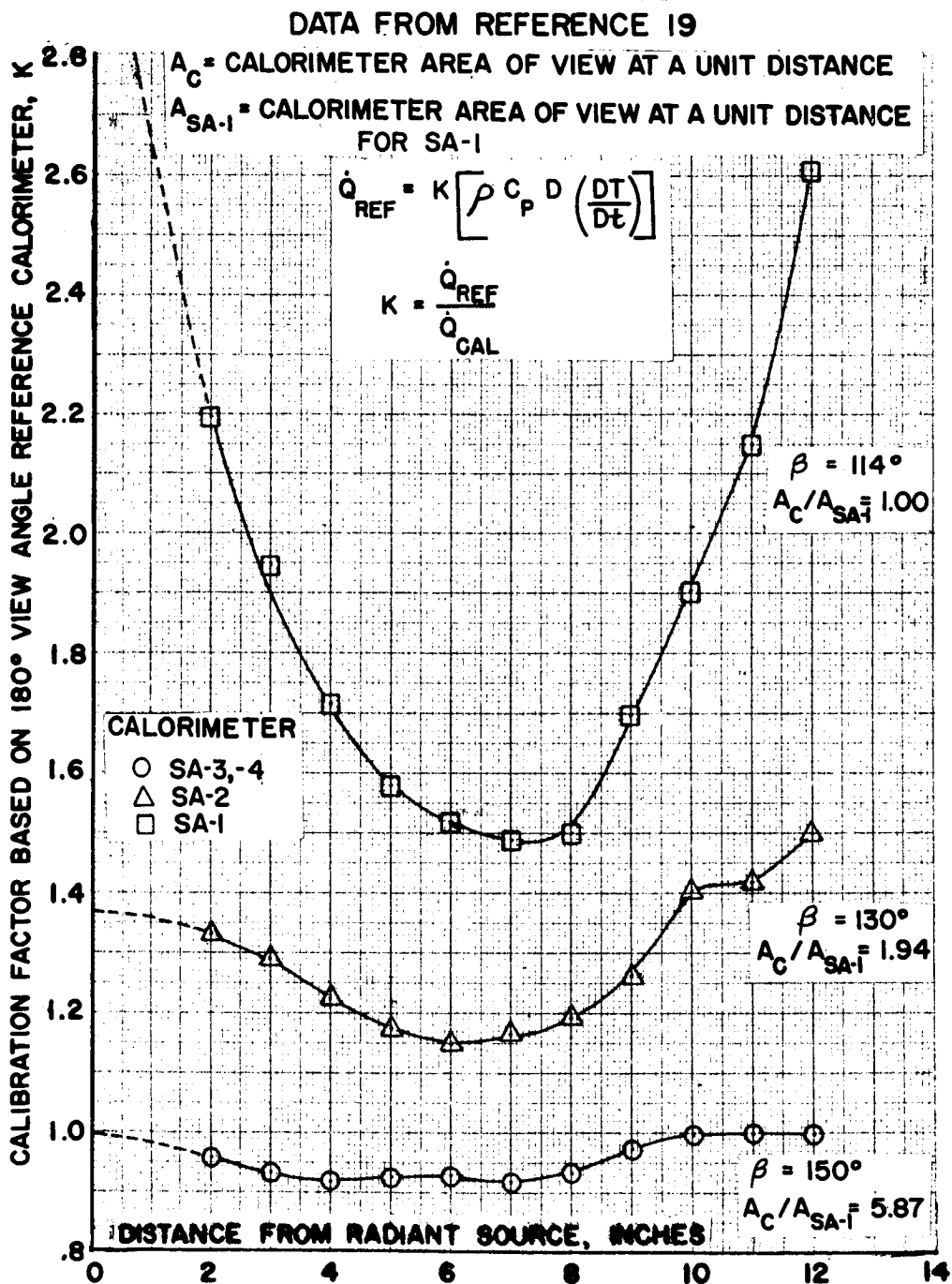
FIGURE B-1. CALIBRATION FACTOR FOR THE SATURN FLIGHT RADIATION CALORIMETER COMPARED TO A 180° VIEW ANGLE REFERENCE CALORIMETER

TOTAL VIEW ANGLE = 114°

$$K = \dot{Q}_{REF} / \dot{Q}_{SA-1}$$
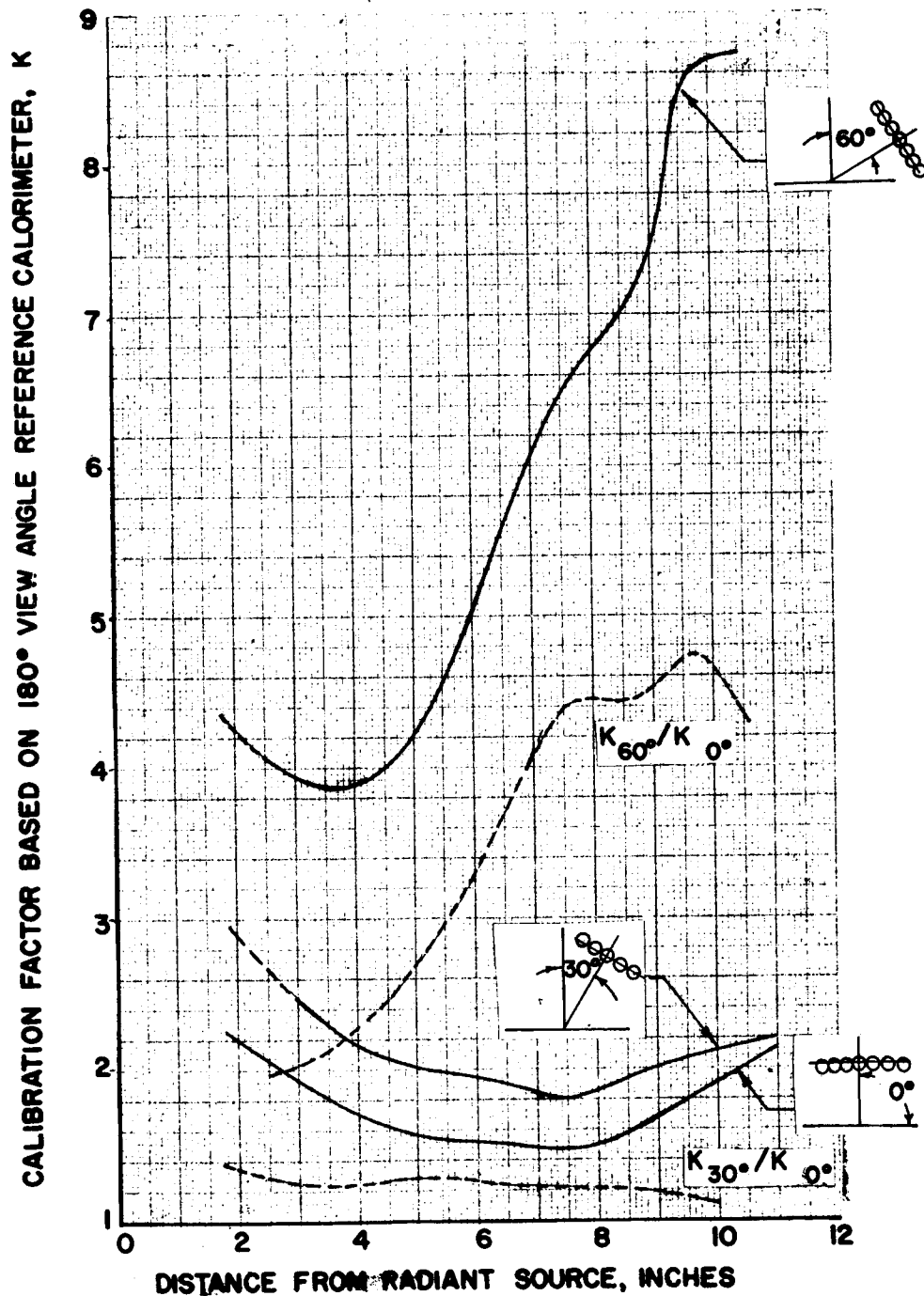
FIGURE B-2. EFFECT OF ANGLE OF INCIDENCE ON THE SA-1 RADIATION CALORIMETER

(MULTIPLE REFRACTION CONSIDERED-WINDOW 1 MM THICK)
Γ = 1.725 (AVERAGE VALUE OF REFRACTIVE INDEX OVER
SPECTRAL RANGE OF 2-3 MICRONS)
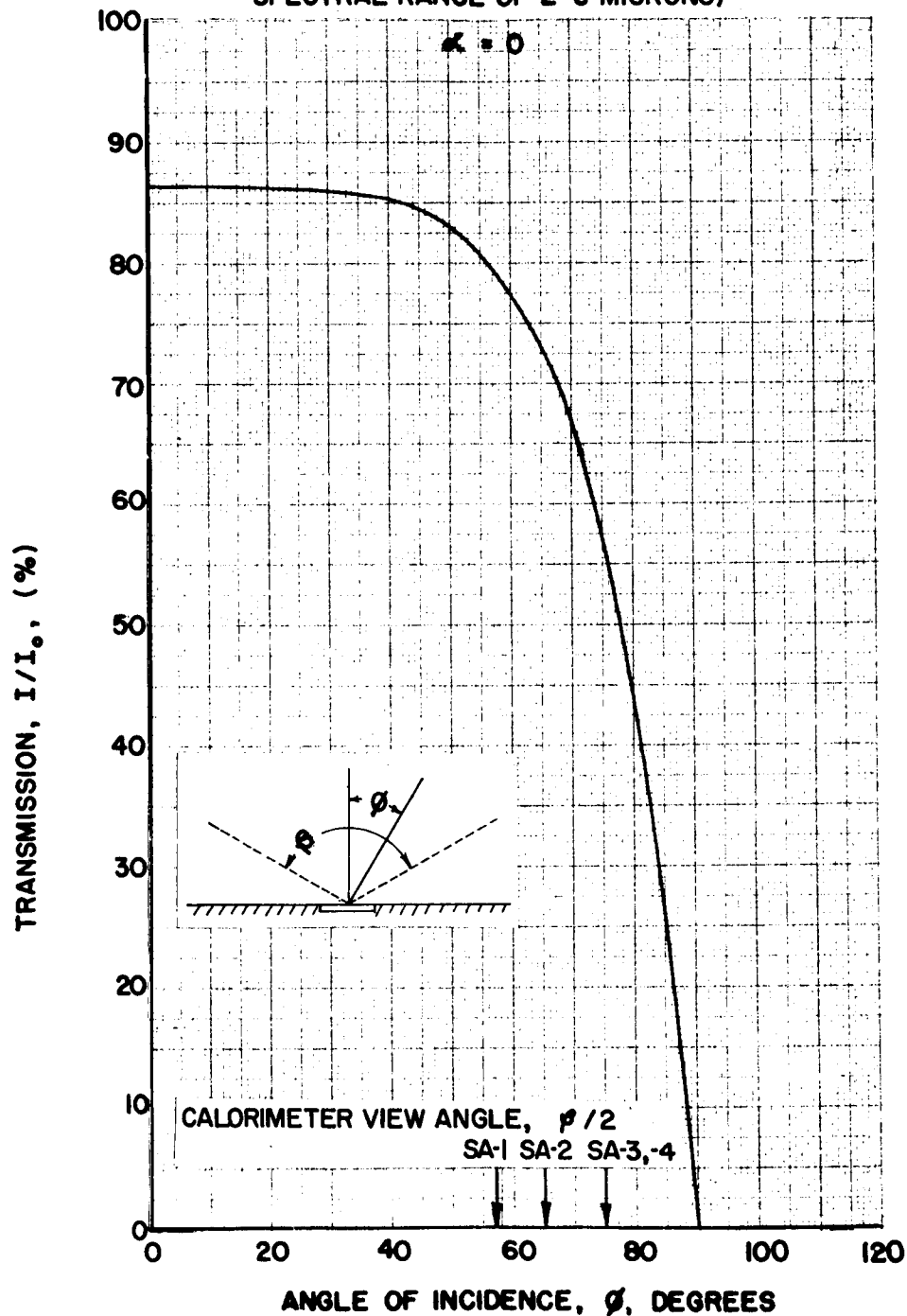
FIGURE B-3. RATIO OF THE RADIATION TRANSMITTED
TO THE INCOMING INTENSITY OF THE
SAPPHIRE WINDOW

LIST OF ILLUSTRATIONS

APPENDIX C.

APPENDIX C

MODEL SCALING METHOD

The problem of scaling model convective heating rate data as discussed in the body of this report has been a very difficult one. The procedure used for the included data has been based on the work found in References 30, 31, and 32. The analysis admittedly does not account for many of the dissimilar effects between model and prototype and the condition of a hot gas circulating in the base. It was found that the local heat transfer by forced convection from the base surface of blunt bodies correlated satisfactorily using an equation of the type.

$$\text{Nusselt Number} = \text{Constant (Reynolds Number)}^{2/3}$$

$$\frac{hD}{K} = C \left(\frac{U_\infty D}{\nu}\right)^{2/3} , \tag{1}$$

where h = heat transfer coefficient

K = thermal conductivity of air

U_∞ = freestream velocity

C = constant

ν = kinematic viscosity

D = vehicle base diameter

Solving equation (1) for h, we obtain

$$h = C K \left(\frac{U_\infty}{\nu}\right)^{2/3} D^{-1/3}$$

under the assumption that the air flow properties over the model and prototype are the same.

Then,

136

$$\frac{\cdot h}{D^{-1/3}} = \text{Constant.} \tag{3}$$

For model scaling

$$\frac{h_{mod}}{D_{mod}^{-1/3}} \cdot = \frac{h_{flt}}{D_{flt}^{-1/3}} \quad , \tag{4}$$

or

$$h_{flt} = h_{mod} \left(\frac{D_{mod}}{D_{flt}}\right)^{1/3} \quad , \tag{5}$$

where flt = the flight value

mod = the model value.

The value of D_{mod}/D_{flt} is actually the model scale and for the Cornell and AEDC tests h

$$h_{flt} = h_{mod} (.0547)^{.333} = .378 \ h_{mod} \quad , \tag{6}$$

and for the Lewis tests

$$h_{flt} = h_{mod} (.0357)^{.333} = .329 \ h_{mod} \quad . \tag{7}$$

Now, to correct the model convective heating rates to a flight equivalent, the heat transfer coefficient is defined as

$$h = \frac{\dot{q}_c}{(T_R - T_w)} \quad , \tag{8}$$

where $\dot{q}_c$ = convective component of the heating rate from a total calorimeter

T_R = recovery temperature

T_w = calorimeter slug temperature .

Substituting in equation (5) the appropriate flight and model values

$$(\dot{q}_c)_{flt} = (\frac{D_{mod}}{D_{flt}})^{1/3} (T_r - T_w)_{flt} h_{mod} \tag{9}$$

or

$$(\dot{q}_c)_{flt} = (\frac{D_{mod}}{D_{flt}})^{1/3} \frac{(T_R - T_w)_{flt}}{(T_R - T_w)_{mod}} \dot{q}_{c_{mod}} \tag{10}$$

For the flight data, T_R is taken as the measured gas temperature (T_g) in the base region near the point where the heating rate was measured.

The model value of T_R is found by plotting the calorimeter measured heating rate (for a constant condition of altitude and Mach number) as a function of the slug wall temperature (Fig. C-1). The constant value of the measured radiation heating rate was subtracted. The intersection of the curve at $\dot{q}_c = 0$ yields the value of the recovery temperature (T_R).

The model heating rates, when plotted versus the calorimeter slug temperature, usually peaked near 38°C. This value is taken as reference temperature when model heating rates are compared. As seen from Figure C-1, the slope of this curve will yield the model value of the heat transfer coefficient (h_{mod}).
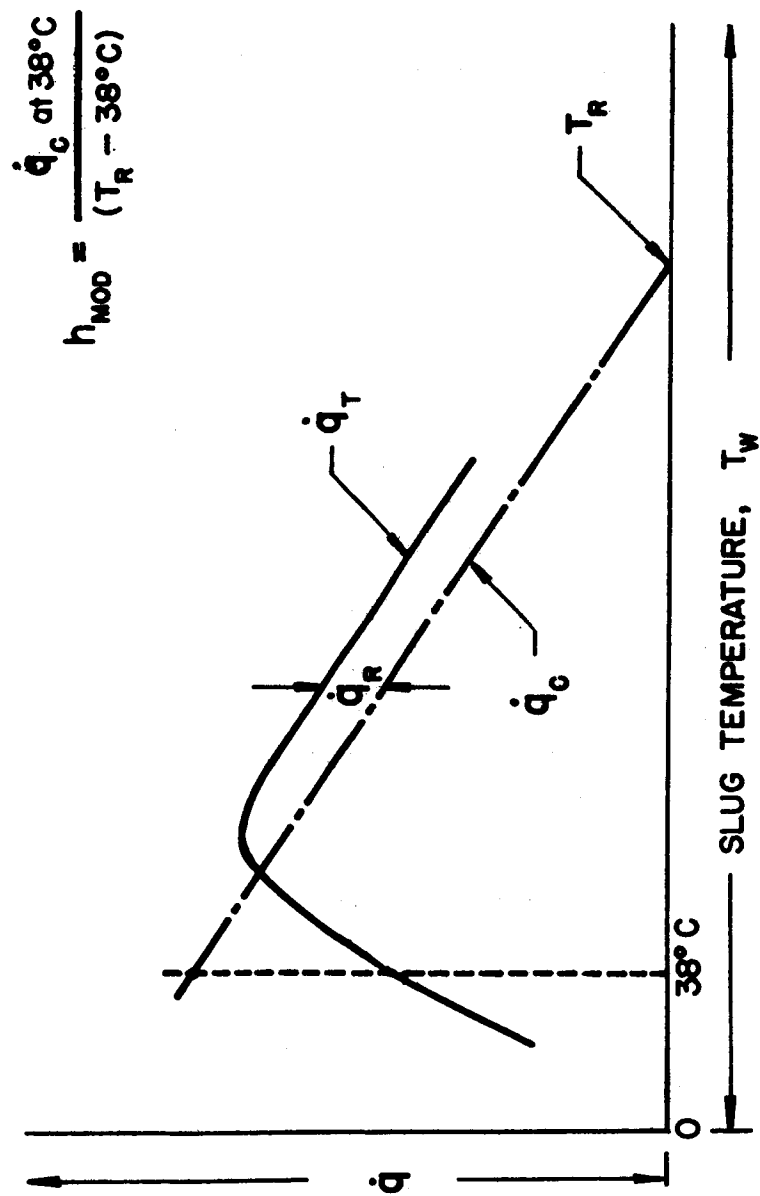
138

$$h_{MOD} = \frac{\dot{q}_c \text{ at } 38°C}{(T_R - 38°C)}$$

FIGURE C-I.   EVALUATION OF MODEL HEAT TRANSFER COEFFICIENT
AND RECOVERY TEMPERATURE

139

REFERENCES

1. Saturn Flight Evaluation Working Group, MSFC, Saturn SA-1 Flight Evaluation. MPR-SAT-WF-61-8, December 1961, Confidential.

2. Saturn Flight Evaluation Working Group, MSFC; Saturn SA-2 Flight Evaluation. MPR-SAT-WF-62-5, June 1962, Confidential.

3. Saturn Flight Evaluation Working Group, MSFC; Saturn SA-3 Flight Evaluation. MPR-SAT-63-1, Vol. I and II, January 1963 Confidential.

4. Saturn Flight Evaluation Working Group, MSFC; Results of the Fourth Saturn I Launch Vehicle Test Flight. MPR-SAT-63-6, May 1963 Confidential.

5. Fitzpatrick, E. J.: Jupiter Base Heating. ABMA Report No. DSD-TM-25-59, October 1959, Secret.

6. Etemad, G. A.; Parker, G. H.; Sheeren, M. L.: Flow Characteristics, Convective and radiative Heating in Base Areas of the Polaris Missile. Lockheed Aircraft Corp., LMSD-480445, November 20, 1959, Secret.

7. Jones, L.: A compilation of Work Performed to Date at HTL Concerning Evaluation of Saturn I Flight Calorimeters. Heat Technology Laboratory, HTL-TR-16, April 6, 1964.

8. Hoberg, Otto A.: Evaluation of Type 5 Total Heat Calorimeter for Thermal Losses when Mounted in Heat Conducting Structure. NASA-MSFC Memo M-ASTR-IM-63-66, February 18, 1963.

9. Hoberg, Otto A.: Preflight Calibration of Total-Heat Type Calorimeters for SA-4 Flight. NASA-MSFC Memo M-ASTR-IM-63-117, March 25, 1963.

10. Jones, D. L.: Reduction of Data from the Hy-Cal C-1080 Calorimeter Space Technology Laboratory, Inc., STL/TOR 6120-6242-N-0-000, January 11, 1962.

11. Hornbaker, D. R.: Analytic Investigations of Heat Rate Meters. Advanced Technology Laboratories, Division of American Standard Co., ATL-D-711, October 31, 1961.

REFERENCES (Cont'd)

12. Westkaemper, J. C.: An Analysis of Slug-Type Calorimeters for Measuring Heat Transfer from Exhaust Gases. AEDC-TN-60-202, November 1960.

12. Rubesin, Morris W.: The Effect of an Arbitrary Surface-Temperature Variation along a Flat Plate on the Convective Heat Transfer in an Incompressible Turbulent Boundary Layer. NASA TN 2345, April 1961.

14. Sprinks, Tudor: Influence of Calorimeter Heat Transfer Gages on Aerodynamic Heating. American Institute of Aeronautics and Astronautics Journal, Vol. 1, No. 2, February 1963, pp. 497-498.

15. Sogin, H. H.; Subramanian, V. S.; and Sogin, R. S.: Heat Transfer from Surfaces of Non-uniform Temperature Distribution, Final Report Part I -- Local Rates of Mass Transfer from Circular Cylinders in Cross Flow. AFOSR Technical Report 60-78, 1960.

16. Sogin, H. H.; Richardson, P. D.: Research to Study the Effects of Flow Separation on Convective Heat Transfer. Brown University, Contract AF 33(616)-5756, Progress Report Number 3, February, 1959.

17. An Investigation of Heat Flux Transducers, Heat Technology Laboratory, Inc., HTL-ER-4, December 13, 1962.

18. Datis, Angelo: Preliminary Results of an Analytical Investigation of a Total Copper-Slug Calorimeter. NASA-MSFC Memo M-AERO-A-34-63. April 11, 1963.

19. Holterman, L. K. A.: Evaluation of View Angles for the Chrysler Radiation Calorimeters Used on Saturn Vehicles SA-1, SA-2, and SA-3. Chrysler Corporation Space Division, Huntsville Operations, Structures and Mechanics Engineering Department, January 24, 1963.

20. Broach, Billy: Simulation of Flight Heat Flux Levels for the SA-5 Flame Shielding Total Heating Calorimeter. Heat Technology Laboratory Memo No. 31, August 1964.

21. Pohl, Henry O.: The Development of a 1/20 Scale Model Saturn Booster for Wind Tunnel Base Heating Studies. NASA-MSFC Internal Note IN-TEST-20-61, December 1961.

REFERENCES (Cont'd)

22.   Kennedy, T. L.; Lowry, J. F.: An Investigation of Base Heating on
        a 5.47-percent Scale Model of the Saturn S-1 Booster at Transonic
        Mach Numbers, AEDC-TN-61-106, August 1961.

23.   Parker, Jr., Joseph R.; Gillard, T. J.: An Investigation of Base
        Heating with a 5.47-percent Saturn SA-1 Booster Model at Mach Numbers
        0.8 and 1.15. AEDC-TN-61-134, November 1961.

24.   Dawson, Jr., John G.: An Investigation of Base Heating on a 5.47-per-
        cent Scale Model Saturn SA-1 Booster Afterbody at Mach Numbers 1.63
        and 3.07. AEDC-TDR-62-9, January 1962.

25.   Parker, Jr., Joseph R.: An Investigation of Base Heating on a 5.47-
        percent Scale Model Saturn SA-5 Booster Afterbody at Mach Numbers
        0.8 and 1.2 and Typical Trajectory Altitudes. AEDC-TDR-62-62,
        April 1962.

26.   Peters, Tom; Dawson, Jr., John G.; Melton, Hershel R.: Base Heating
        and Base Pressure on a Scale Model Saturn SA-5 Booster Afterbody at
        Mach Numbers 1.63 and 3.07. AEDC-TDR-62-147, October 1962,
        Confidential.

27.   Klees, G. T.: Development Testing Techniques Employed in the Saturn
        Hot-Jet Tests Conducted at Lewis Research Center's 8 x 6 Foot Wind
        Tunner Facility. Chrysler Corp. Space Division, Huntsville Operations,
        HSM-R1072, August 1962.

28.   Allen, John L.; Wasko, Robert A.: Base Heat Transfer, Pressure
        Ratios and Configuration Effects Obtained on a 1/27 Scale Saturn (S-1)
        Model at Mach Numbers 0.1 to 2.0. Lewis Research Center, NASA
        TN D-1566, July 1962.

29.   Jones, Jr., Ira P.: Comparison of Long Duration Base Heating Data
        with the Cornell Short Duration Technique. NASA-MSFC Memo No.
        M-AERO-A-78-62, October 15, 1962.

30.   Sogin, H. H.: Heat Transfer from the Rear of Bluff Objects to a Low
        Speed Air Stream. Aeronautical Research Laboratories, United States
        Air Force ARL 62-361, June 1962.

REFERENCES (Concluded)

31. Richardson, P. D.: Estimation of the Heat Transfer from the Rear of an Immersed Body to the Region of Separated Flow. WADD TN-59-1, Air Research and Development Command, United States Air Force, January 1960.

32. Larson, H. K.: Heat Transfer in Separated Flows. Journal of Aerospace Sciences, November 1959, pp. 731-738.

33. Jones, Jr., Ira P.: Some Additional Results of the AEDC Saturn SA-1 Hot Jet Tests. NASA-MSFC Memo No. M-AERO-A-39-62, June 15, 1962.

34. Hoberg, Otto A.: Postflight Calibration of SA-4 Flight Calorimeters. NASA-MSFC Memo M-ASTR-IM-63-155, April 12, 1963.
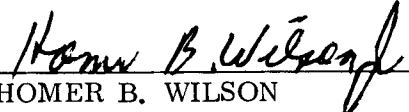
SUMMARY OF BASE THERMAL ENVIRONMENT MEASUREMENTS ON THE SATURN I BLOCK I FLIGHT VEHICLES
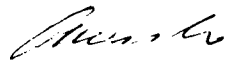
By

Ira P. Jones, Jr.

The information in this report has been reviewed for security classification. Review of any information concerning Department of Defense or Atomic Energy Commission programs has been made by the MSFC Security Classification Officer. This report, in its entirety, has been determined to be unclassified.

This document has also been reviewed and approved for technical accuracy.

HOMER B. WILSON
Chief, Thermal Environment Branch

WERNER K. DAHM
Chief, Aerodynamics Division

E. D. GEISSLER
Director, Aero-Astrodynamics Laboratory

DISTRIBUTION

DIR

DEP-T

I-DIR

I-SE-CH

I-I/IB-DIR
    Col. James

I-MO-MGR
    Dr. Speer
    Mr. Clark

R-DIR
    Mr. Weidner

R-SA-DIR

R-AERO-DIR
    Dr. Geissler
    Mr. Jean

R-AERO-F
    Mr. Lindberg

R-AERO-FFA
    Mr. Garcia

R-AERO-A
    Mr. Dahm
    Mr. Holderer

R-AERO-AA

R-AERO-AD
    Mr. May

R-AERO-AT
    Mr. Wilson
    Mr. Few
    Mr. Jones (20)

R-AERO-T
    Mr. Reed

R-AERO-ADE
    Mr. Andrews

R-AERO-P
    Mr. McNair
    Mr. Teague

R-AERO-ADD
    Mr. Dunn

R-AERO-ATB
    Dr. Farmer
    Mr. Brewer

R-AERO-ATA
    Mr. Elkin
    Mr. Cooper

R-AERO-ATP
    Mr. Huffaker

R-AERO-AF

R-AERO-YE

R-AERO-FFR

R-ASTR-I
    Mr. Hoberg

R-ASTR-IMD
    Mr. Avery

R-ASTR-F

R-ASTR-IMT
    Mr. Burke

R-COMP-RR
    Mr. Cochran

R-P&VE-DIR

R-P&VE-PP

R-P&VE-PTD
    Mr. McAnelly
    Mr. Hopson

R-P&VE-SL

R-P&VE-S

R-P&VE-PT
    Mr. Connell

R-P&VE-P
    Mr. Paul

MS-IL   (8)

MS-IP

MS-H

MS-T   (5)

EXTERNAL

Mr. John O. Windham
MSFC Resident Liaison Engineer
NASA, Langley Research Center
Langley Station, Bldg. 1218
Hampton, Virginia

The Boeing Company
HIC Bldg.
Mail Stop AF-77
Huntsville, Alabama
Attn: R. Mullen
       R. Bender
       K. Halvorson

Chrysler Corporation Space Division
P. O. Box 26018
Department 2761
New Orleans 26, Louisiana
Attn: Mr. J. Tucker
       Mr. B. Elam
       Mr. L. Hartley

Lockheed Research and Engineering Center
Huntsville, Alabama

North American Aviation
Space and Information Systems
12214 Lakewood Boulevard
Downey, California
Attn: A. Shimizu
      F. Laspesa

Scientific and Technical Information Facility   (25)
P. O. Box 5700
Bethesda, Maryland
Attn: NASA Representative
      S-AK/RKT

Mr. Robert Wasko
Lewis Research Laboratory
Mail Stop 86-1
Cleveland, Ohio

Douglas Aircraft Co.
5301 Bolsa Ave.
Huntington Beach, California 92646
Attn: Mr. D. Dearing